OPTIMIZATION, CONTROL, AND FLIES: QUANTITATIVE STUDIES OF INSECT FLIGHT

A Dissertation

Presented to the Faculty of the Graduate School

of Cornell University

in Partial Fulfillment of the Requirements for the Degree of

Doctor of Philosophy

by

Gordon Joseph Berman

August 2009

OPTIMIZATION, CONTROL, AND FLIES: QUANTITATIVE STUDIES OF INSECT FLIGHT

Gordon Joseph Berman, Ph.D.

Cornell University 2009

Insects are graceful and varied locomotors – flying, darting, and hovering with apparent ease and sophistication. Accordingly, their abilities have long engendered the curiosity of scientists and the envy of aerospace engineers. This thesis aims to shed light on some basic questions regarding the aerodynamics and control of insects, primarily through the guise of studying the fruit fly *Drosophila melanogaster*. Via these investigations, I attempt to elucidate some of the overarching problems in biolocomotion regarding optimization of movements, control of maneuvers, and the interaction between animals and their surrounding fluid.

Chapter 2 uses a quasi-steady model of intermediate Reynolds number aerodynamics to estimate the forces and torques experienced by an insect during hovering flight and asks whether the observed kinematics are energy-minimizing. Since insect flight is such a costly endeavor, it makes for an interesting test case of the hypothesis that animals move in a manner which minimizes metabolic cost.

The quantitative study of insect flight is currently a data-limited field, hence, it is imperative to realize new methods for obtaining and digitizing flight sequences. Chapter 3 describes the Hull Reconstruction Motion Tracking (HRMT) method, which takes three camera views of a freely flying fruit fly, and by using visual hull reconstruction and principal components analysis, automatically tracks the insect body and wings both quickly and accurately.

Using the data generated from applying HRMT to experimentally recorded movies, Chapter 4 analyzes the flight of ascending fruit flies. Having obtained several flight sequences of flight in which the filmed insect is moving almost straight upwards, we analyze the dynamics of how a steady-state ascending velocity is achieved, and what control knobs a fly can use to adjust this state. Additionally, we look at how fruit flies can quickly transition from one ascent speed to another.

The optimization line of thought highlighted in Chapter 2 is extended in Chapter 5, but is combined with some of the obtained experimental data from our collaboration with Leif Ristroph and Itai Cohen. Here, we relate the concept of optimization in locomotion to variations apparent within a population. Through utilizing some of the methods from sloppy modeling, we explore the idea of a fitness landscape for wing kinematics, and how that might effect the spread of data observed in experiments.

Finally, chapters 6 and 7 investigate aspects of a model of falling plates at intermediate Reynolds numbers which is used as an underpinning for much of the work done here. Chapter 6 studies how the model transitions to chaos through a period-doubling bifurcation, and Chapter 7 asks what type of flight trajectories are possible if the system is driven by a rotational actuator.

BIOGRAPHICAL SKETCH

The author was born to parents Jack and Catherine Berman on August 6th, 1980 in Traverse City, Michigan. He resided there for the first eighteen years of his life, living amongst the lakes, the trees, and the tourists. Being the progeny of a math professor and a librarian, Gordon was not imbued with a great deal of knowledge of the more practical nature, but did read many a book and completed more math workbooks than was probably healthy. He played (and plays) piano and percussion and ran cross country and track, as running was the only sport at which a lanky, uncoordinated youth had any hope of not embarrassing himself (there were also flirtations with baseball and football, but they ended badly for all involved). He dreamed of one day knowing how to answer the dreaded question "What do you want to be when you grow up?" He thinks that his lack of an answer to this query one day factored heavily in his decision to attend graduate school.

In the fall of 1999, he matriculated as an undergraduate to the University of Michigan at Ann Arbor. There, he majored in mathematics and physics, performing research in the field of high energy physics. Specifically, he worked on characterizing and constructing the muon spectrometer for the terribly-acronymed ATLAS (A Torroidal LHC ApparatuS) detector at the Large Hadron Collider under the direction of Dr. Daniel Levin and Prof. Bing Zhou, writing a senior thesis entitled "Measurement of the ATLAS Endcap Muon Spectrometer Sagitta Resolution at the 2002 H8 Test Beam."

After graduating from Michigan in April 2003, Gordon enrolled in the doctoral program in the physics department at Cornell University. His initial stated interests were the somewhat incongruous combination of high energy experiment and non-linear dynamics. By the end of his first year, however, he became

increasingly intrigued by problems in the latter of the two fields, a choice reinforced by his experiences in the IGERT program for nonlinear complex systems, headed by Prof. John Guckenheimer. As part of this fellowship, he spent a summer as a visiting researcher at the Santa Fe Institute, working with Prof. David Krakauer investigating problems related to biological computation using diffusive/faulty components.

In the summer of 2004, Gordon began working in Prof. Jane Wang's lab, studying the aerodynamics and biomechanics of insect flight. His initial research focused on understanding the nature of insect wing kinematics, specifically asking if the observed wing motions can be viewed as energy-minimizing. For the past few years, he has been working in collaboration with Leif Ristroph in Prof. Itai Cohen's lab and his lab-mate Attila Bergou to study the kinematics, dynamics, and control of freely-flying fruit flies.

After attaining his doctorate, Gordon will join the theoretical biology group in the Lewis-Sigler Institute at Princeton University as a postdoctoral researcher.

Dedicated to my parents,

Jack and Catherine Berman.

ACKNOWLEDGEMENTS

As is the case of most any document with a gestation time on the order of this thesis, there have been many people who have played a part in stewarding it towards completion, of which I shall try my hardest to acknowledge as many as possible here.

First, I would like to offer my thanks and gratitude to my advisor, Jane Wang, and the many students and postdocs who have populated her lab throughout my tenure at Cornell. Jane's knowledge and enthusiasm have been of great aid, providing me with assistance when needed, ideas when stuck, and sufficient rope when I wanted to stumble a little bit further into the academic wilderness than was most likely beneficial. Additionally, I would be remiss to omit my entomological-partner-in-crime Attila Bergou, who has sat beside me for the preponderance of my time in the group. Without the many, often quite lively, discussions we've had, the quality of the work presented here would have most definitely suffered. I would also like to thank Anders Andersen, Umberto Pesavento, and Sheng Xu for their help in orienting me to the world of fluid dynamics.

My research with experimental collaborators Itai Cohen and Leif Ristroph, has been remarkably rewarding and has greatly improved both my work and my time spent working. Itai's seemingly endless reserves of energy and creativity have been a boon to this thesis, and Leif's experimental prowess and ability to extract the essence of a problem has yet to cease to impressing me. Also deserving thanks are Witat Fakcharoenphol and Brad Lyon, undergraduates extraordinaire who helped collect data for the tracking and ascending sections of this thesis.

I would also like to express a great deal of gratitude towards John Guckenheimer, who has a tremendous source of both technical and creative advice, both as the primary figure in the NSF-IGERT program in nonlinear and complex systems here at Cornell (which is also deserving of much thanks) and as mentor and collaborator since. James Sethna has also provided a great deal of help over the years, giving me advice in matters of statistical physics and the sloppy modeling portion of this thesis in particular. Ryan Gutenkunst has been of great assistance in this area as well. Additionally, Andy Ruina has been a great source of information and inspiration regarding all matters mechanical and optimal.

There is no way I could have waded through all of the work placed into this document without the aid, encouragement, and harassment provided by my family and friends. In particular, I would not be in the position of defending my thesis without everything my parents, Jack and Cathy Berman, have done for me (and I mean this in far more than the entirely literal sense of my own ontology). My brothers, Gregory and Alexander, have been instrumental in the aforementioned harassment aspect, but despite this (and partially because of it), they deserve my thanks here. And I must admit that I owe the preponderance of my sanity to my fiancée, Jennifer, who is my daily reminder that man cannot live on computers and flies alone. Thank you.

TABLE OF CONTENTS

LIST OF TABLES

LIST OF FIGURES

CHAPTER 1

OVERVIEW

When animals move, we pay attention. Whether gazing at a hawk soaring through the air or a school of fish pulsing forward in a disorganized union or a gazelle racing with reckless ferocity across an undulating plane (or, for that matter, the lion pursuing it), animal locomotion garners not only our aesthetic appreciation, but also our scientific curiosity. And not without merit – all of the cases listed above are the result of complex interactions between the animals' mechanics, senses, environment, physiology, and evolutionary history.

The field of biolocomotion aims to probe the nature of these interplays, asking questions which can provide general insights into organisms' movement and behavior. For instance, what role does energetics play in locomotion? Do animals perform tasks in a manner which can be viewed as optimal in some sense, or has evolution arrived at a solution which is more complicated? What is the relationship between morphology and motion? What constraints do an organism's evolutionary ancestry place on its locomotion and what sorts of adaptations do we observe? Also, how do animals make decisions about their locomotion in often noisy, challenging environments? How do they use the complicated, conflicting reports of sensory organs, prior experience, and inter-individual interactions to induce a desired body motion? What types of neural processing occur to allow for this all to happen?

Of course, these questions are plainly too broad to base a particular study or to generate a testable hypothesis. Most animals move in some manner, so our options limit us in a way. Often, the response of biological researchers to such a dilemma is to appeal to Krogh's principle [1], which states that "For a large

number of problems there will be some animal of choice on which it can be most conveniently studied." By looking into a particular, (relatively) convenient organism, it is possible to gain intuition and then abstract outward to understand more general ideas. For this thesis, our "animal of choice" will be flying insects, and most often, the fruit fly *Drosophila melanogaster*. Through the lens of these creatures' flight kinematics and dynamics, many of the aforementioned questions are investigated via a combination of computation, analysis of simplied models, and comparison to experimental data.

So why fruit flies? For starters, they are varied and effective locomotors, able to hover, dodge and maneuver with an apparent effortlessness and elegance. Accordingly, their flight has engendered much interest in the scientific and engineering communities, attempting to both understand their aerial mechanisms [2–5] and to replicate their aerodynamic performance via engineering of micro-air vehicles (MAVs) [6–9]. Additionally, a practical reason for studying fruit flies in particular has been that they are obtained with relative ease, as they are found and bred in many a genetics lab, and are manageable to maintain. Also, since they are perhaps the most studied animal in scientific history [10,11], intriguing possibilities exist for relating concepts and discoveries in genetics to questions in biolocomotion.

Even given this insect as the primary subject of study, however, there of course remain many different means through which one can investigate the problems in which we are interested. On a most basic level, the studies in which one can partake range from the realistic veracity of "in the wild" biological surveys [12–15] to the more controlled environment of observing animals in the lab [16–25] to the the intuitive abstraction of physical modeling [26–33]. In phi-

losophy, this thesis tends to lean more on the latter of these approaches (the author, after all, is attempting to obtain a doctorate in physics), but aims not to venture too far away from naturalistic verisimilitude by continuously comparing its modeling results to experimental data obtained from fruit flies in free flight.

More specifically, the research content of this thesis opens in Chapter 2, which asks if observed insect kinematics are energy-minimizing. This work uses a quasi-steady model of intermediate Reynolds number aerodynamics to estimate the forces and torques experienced by an insect during hovering flight. Since insect flight is such a costly endeavor, it makes for an interesting test case of the hypothesis that animals move in a manner which minimizes metabolic cost.

Chapter 3 entails a description of the Hull Reconstruction Motion Tracking (HRMT) method which I co-developed with Leif Ristroph and Attila Bergou. This technique takes three camera views of a freely flying fruit fly, and by using visual hull reconstruction [34] and principal components analysis [35], automatically tracks the insect body and wings both quickly and accurately.

Using the data generated from applying HRMT to experimentally recorded movies, Chapter 4 analyzes the flight of ascending fruit flies. Having obtained several flight sequences of flight in which the filmed insect is moving almost straight upwards, we analyze the dynamics of how a steady-state ascending velocity is achieved, and what control knobs a fly can use to adjust this state. Additionally, we look at how fruit flies can quickly transition from one ascent speed to another.

The optimization principle highlighted in Chapter 2 is extended in Chapter 5, but is combined with some of the obtained experimental data from our collaboration with Leif Ristroph and Itai Cohen. Here, we relate the concept of optimization in locomotion to variations apparent within a population. Through utilizing some of the methods described in [36–39], we explore the idea of a fitness landscape for wing kinematics, and how that might effect the spread of data observed in experiments.

Chapters 6 and 7 investigate aspects of a model of falling plates at intermediate Reynolds numbers [40–42] which is used as an underpinning for much of the work done here. Chapter 6 studies how the model transitions to chaos through a period-doubling bifurcation, and Chapter 7 asks what type of flight trajectories are possible if the system is driven by a rotational actuator.

CHAPTER 2

ENERGY-MINIMIZING KINEMATICS IN HOVERING INSECT FLIGHT

2.1 Introduction[1]

Insect flight is a metabolically costly endeavor, requiring mass-specific oxygen consumption rates which are about an order of magnitude higher than than those measured in their terrestrially locomoting counterparts [43, 44]. Additionally, flying represents a 50-200 fold elevation from the basal metabolic rate [45, 46]. Hovering flight is particularly costly, as there is no ambient wind to aid in lift generation. Accordingly, a reasonable hypothesis is that insects move their wings in a manner which minimizes the metabolic cost associated with their motion. In this study, we test this hypothesis for the case of hovering flight and examine its implications through modeling the fluid forces on an insect wing and finding and analyzing the optimal kinematics of motion for a given morphology. Specifically, we investigate the optimal kinematics for fruit fly (*Drosophila melanogaster*), bumblebee (*Bombus terrestris*), and hawkmoth (*Manduca sexta*) morphologies. These insects range in mass by approximately three orders of magnitude.

This idea of optimizing traits with respect to some cost function as means of explaining animal behavior has generated much interest and controversy amongst evolutionary biologists and biomechanists [47–60]. Much of the criticism aimed at studying biomechanics problems in this manner states that given the many functions of a living organism, it is unclear that a specific behavior can

[1]The work presented in this chapter originally appeared in Berman & Wang, *J. Fluid Mech.*, **582**, 153-168 (2007).

be predicted by optimizing a single function. Moreover, even if such a function can be defined, it is not clear that any new insight must necessarily emerge from the study, as even a correctly predicted feature from optimization can be the result of an ignis fatuus emitted above the bog of evolution. However, for the case of a hovering insect, the energetic demands associated with maintaining flight make the power associated with generating a particular wing motion a natural candidate for a cost function. This distinct relationship between form and function (wing kinematics and hovering ability) allows us to investigate whether quantitative study can help to explain some common features in the observed wing motions of a diverse set of insects.

In this study, we find and analyze the energy-minimizing kinematics for the three insects mentioned above via a quasi-steady model of fluid forces. This model is similar to the one used by [40–42] to study the dynamics of a free-falling rigid plate. From this model, we calculate the average lift production and power consumption over the course of a flapping cycle. Using a hybrid optimization algorithm that combines a genetic algorithm with a gradient-based optimizer, we find the kinematics that minimize the power usage while still producing enough lift to maintain hovering flight. Aspects of these kinematics are then compared to previously measured wing strokes. We also study the sensitivity of the found optimal solutions to perturbations in various kinematic parameters to gain insight into why the optimal kinematics are at their found values. Finally, we investigate why most insects use a single leading edge throughout a flapping cycle, as opposed to alternating the leading edge near the onset of each half-stroke.

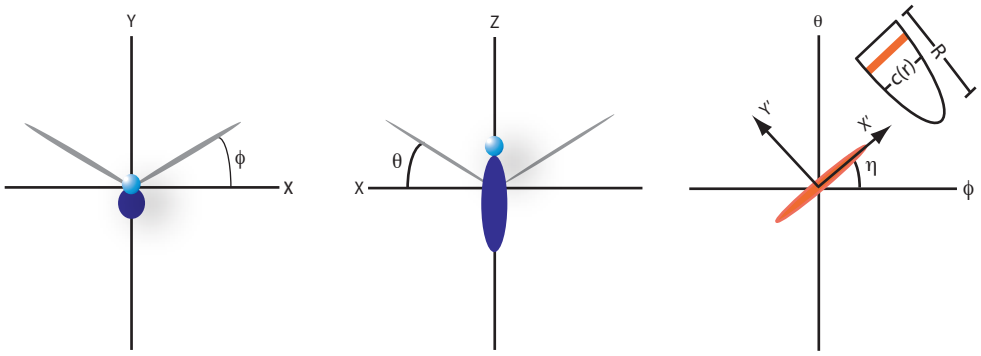

Figure 2.1: Angle definitions

2.2 Model of Insect Hovering

Here we describe our mathematical model for calculating the forces, torques, and power consumption associated with insect flight, as well as the computational methods used to analyze it and determine the optimal kinematics.

2.2.1 Coordinate Definitions and Transformations

We assume that an insect's wing is a rigid plate and is allowed to rotate along each of its three Euler angles. That is, it can rotate azimuthally (ϕ), vertically (θ), and can pitch about its radial axis (η). If z is the vertical direction, y is the forward direction of the insect, and x is perpendicular to the forward direction in the horizontal plane, then we have that

$$\begin{pmatrix} x \\ y \\ z \end{pmatrix} = \begin{pmatrix} r\cos\theta\cos\phi \\ r\cos\theta\sin\phi \\ r\sin\theta \end{pmatrix} \tag{2.1}$$

This is visualized in Figure 2.1.

As will be seen in Section 2.2.4, the equations for the aerodynamic forces on a section of the wing become simplified if we view the system's velocities in terms of coordinates co-moving with the wing, x' and y' (Figure 2.1). This transformation is achieved by writing the position of the wing slice in spherical coordinates, and then rotating through the pitching angle, η . In matrix form, this can be written as

$$\begin{pmatrix} \hat{x}' \\ \hat{y}' \end{pmatrix} = R_1 R_2 \begin{pmatrix} \hat{x} \\ \hat{y} \\ \hat{z} \end{pmatrix}, \tag{2.2}$$

where

$$R_1 = \begin{pmatrix} \cos\eta & \sin\eta \\ -\sin\eta & \cos\eta \end{pmatrix} \tag{2.3}$$

and

$$R_2 = \begin{pmatrix} -\sin\phi & \cos\phi & 0 \\ \sin\theta\cos\phi & \sin\theta\sin\phi & -\cos\theta \end{pmatrix}. \tag{2.4}$$

Using this transformation and differentiating with respect to time, we have

$$v_{x'} = r(\dot{\phi}\cos\theta\cos\eta - \dot{\theta}\sin\eta) \tag{2.5}$$

$$v_{y'} = r(-\dot{\theta}\cos\eta - \dot{\phi}\cos\theta\sin\eta) \tag{2.6}$$

$$a_{x'} = r([\ddot{\phi}\cos\theta - \dot{\theta}(\dot{\eta} + \dot{\phi}\sin\theta)]\cos\eta - (\ddot{\theta} + \dot{\eta}\dot{\phi}\cos\theta)\sin\eta) \tag{2.7}$$

$$a_{y'} = r([\dot{\theta}(\dot{\eta} + \dot{\phi}\sin\theta) - \ddot{\phi}\cos\theta]\sin\eta - (\ddot{\theta} + \dot{\eta}\dot{\phi}\cos\theta)\cos\eta), \tag{2.8}$$

where v_i and a_i are the velocity and the acceleration of the wing in direction i, and r is the distance along the radius from the wing's base.

2.2.2 Wing Geometry

For simplicity, the wing cross-section along the chord is assumed to be elliptical, with semi-minor axis, b, which represents the wing thickness. The chord length, $c(r)$, of the wing is assumed to vary like a half-ellipse along the wing radius. This is similar to the assumption made in [61]. Hence, the chord length as a function of radius is given by

$$c(r) = \frac{4\bar{c}}{\pi}\sqrt{1 - \frac{r^2}{R^2}}, \tag{2.9}$$

where $\bar{c}$ is the mean chord length of a wing and R is the wing's base-to-tip radius. We assume that $b \ll \bar{c}$. Morphological values used in this study were taken from [62] for the fruit fly, [63] for the bumblebee, and [64] for the hawkmoth.

2.2.3 Wing Kinematics

Drawing upon available kinematic data from prior empirical studies [3, 25, 62–65], the flapping motion of hovering flight is parameterized specifically in order to observe the effects of the rotation speed and relative phases of the wing's pitch and reversal, as well as the frequency and amplitude of the motion in the three angular degrees of freedom described in Section 2.2.1.

The azimuthal coordinate, $\phi(t)$, is given by a smoothed triangular waveform,

$$\phi(t) = \frac{\phi_m}{\sin^{-1} K}\sin^{-1}[K\sin(2\pi f t)], \tag{2.10}$$

where $0 < K < 1$. In the limit where $K \to 0$, $\phi(t)$ becomes sinusoidal, and in the limit of K approaching 1, $\phi(t)$ is a triangular waveform (Figure 2.2). In effect, K can be viewed as a measure of how rapidly the wing reverses direction. This functional form was inspired by comparing the azimuthal kinematics between

the experiments listed above, which often found a near-sinusoidal form, and robotic wing experiments, which used a rounded triangular form [66].

The angle related to vertical displacement, $\theta(t)$, is described by a sinusoidal oscillation,

$$\theta(t) = \theta_m \cos(2\pi N f t + \Phi_\theta) + \theta_0, \tag{2.11}$$

where N is either 1 or 2. $N = 1$ corresponds to one vertical oscillation per flapping period, and $N = 2$ corresponds to a figure-8 motion.

Finally, the pitching coordinate, $\eta(t)$, is described by a periodic hyperbolic function,

$$\eta(t) = \frac{\eta_m}{\tanh C_\eta} \tanh[C_\eta \sin(2\pi f t + \Phi_\eta)] + \eta_0. \tag{2.12}$$

As C_η approaches 0, $\eta(t)$ becomes sinusoidal, and as $C_\eta \to \infty$, $\eta(t)$ tends towards a step function (Figure 2.2). Hence, the value of C_η is inversely related to the duration of wing pitch reversal.

Between Equations 2.10-2.12, there are a total of 11 parameters which need to be fixed to describe a wing stroke (Table 2.1). Additionally, we assume that the motions of wings are symmetrical about the body. Despite the fact that this parameterization only looks at a subspace of all possible periodic functions, a wide range of kinematics are still available to the insect, as seen in Figure 2.3.

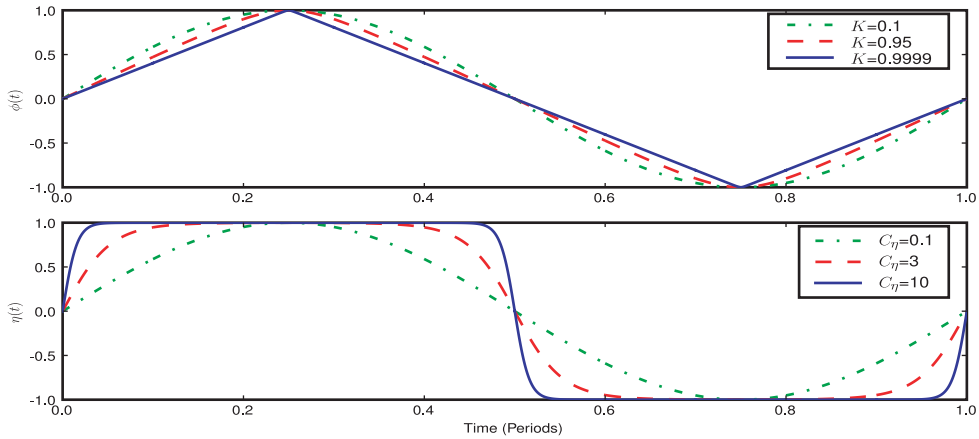

Figure 2.2: Dependence of $\phi(t)$ and $\eta(t)$ on K and C_η

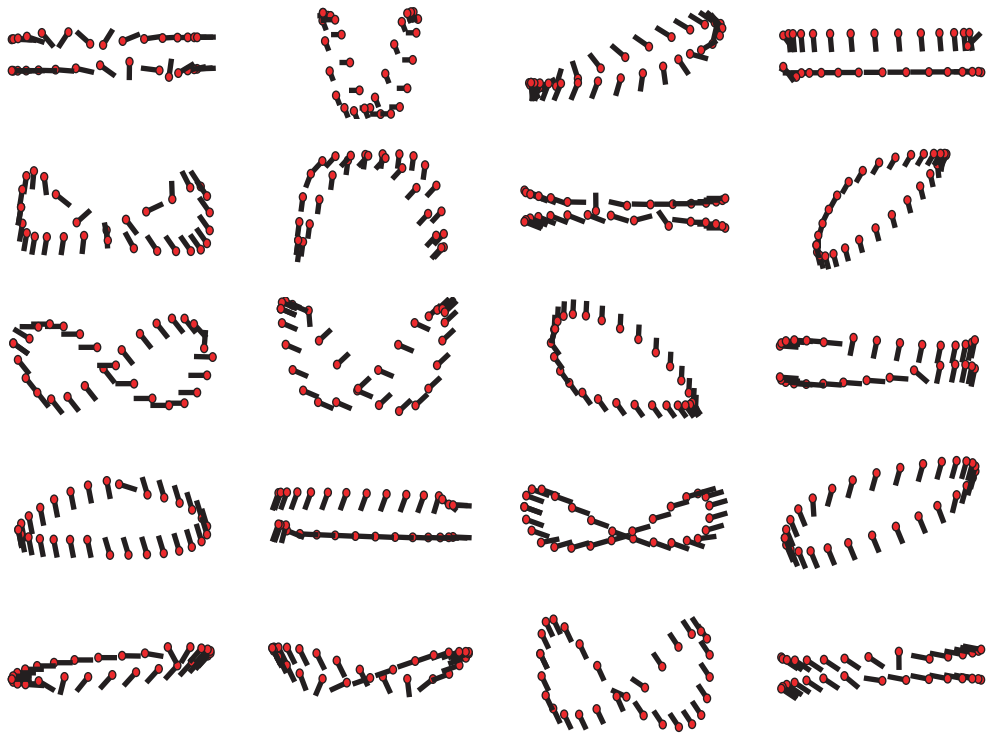

Figure 2.3: A selection of possible wing kinematics. The lines represent a wing chord cross-section, and the dots are placed on the same edge of the wing throughout the stroke.

Table 2.1: Table of independent model parameters and their constraints

	Description	Min	Max
f	Frequency	0	∞
ϕ_m	Azimuthal Amplitude	0	$\pi/2$
θ_m	Vertical Amplitude	0	$\pi/2$
η_m	Pitching Amplitude	0	π
θ_0	Vertical Offset	$\theta_m - \pi/2$	$\pi/2 - \theta_m$
η_0	Pitching Offset	$\eta_m - \pi$	$\pi - \eta_m$
K	Affects the Shape of $\phi(t)$	0	1
C_η	Affects the Duration of Wing Rotation	0	∞
N	Multiplier of $\theta(t)$ Period	1	2
Φ_θ	Vertical Phase Offset	$-\pi$	π
Φ_η	Pitching Phase Offset	$-\pi$	π

2.2.4 Aerodynamic Force Model

The forces acting upon a wing are found via the model formulated to study the motion of a free-falling plate [40–42] combined with a blade-element assumption that the total force on the wing is the sum of forces on many infinitesimal segments was used. This is a quasi-2D force model, as the instantaneous aerodynamic forces for each blade-element are in the plane perpendicular to the wing radius. The use of this model, as opposed to the vastly more computationally costly method of direct numerical simulation via computational fluid dynamics, is that it allows us to perform optimization procedures and detailed sensitivity analyses which require many evaluations of the cost function in question.

Specifically, the forces and torque on an infinitesimal slice of the wing are given by

$$dF_{x'} = [(\frac{c(r)}{\bar{c}R} M_{wing} + m_{22}) v_{y'} \dot{\eta} - \rho_f \Gamma v_{y'} - m_{11} a_{x'}] dr - dF^{\nu}_{x'} \tag{2.13}$$

$$dF_{y'} = [-(\frac{c(r)}{\bar{c}R} M_{wing} + m_{11}) v_{x'} \dot{\eta} + \rho_f \Gamma v_{x'} - m_{22} a_{y'}] dr - dF^{\nu}_{y'} \tag{2.14}$$

$$d\tau^{aero}_{\eta} = [(m_{11} - m_{22}) v_{x'} v_{y'} - I_a \ddot{\eta}] dr - d\tau^{\nu}, \tag{2.15}$$

where a_i is the acceleration component of the wing in coordinate i, M_{wing} is the mass of a wing, $c(r)$ and $\bar{c}$ are the chord length and average chord length as defined in Equation 2.9, R is the wing radius, Γ is the circulation around the wing, $dF^{\nu}_{x'}$, $dF^{\nu}_{y'}$, and $d\tau^{\nu}$ represent the viscous forces and torque on the wing segment, m_{11}, m_{22}, and I_a are added mass terms, and ρ_f is the density of the surrounding fluid (taken to be $1.29\frac{kg}{m^3}$). In the two force equations, the first term is due to the fact that the forces are being measured in a rotating coordinate frame, the second term is the force produced via circulation, the third term is an added mass force, and the final term is the viscous dissipation.

More specifically, the circulation, viscosity, and added mass term are given by

$$\Gamma = -\frac{1}{2}C_T c(r)|\vec{v}|\sin 2\alpha + \frac{1}{2}C_R c^2(r)\dot{\eta} \tag{2.16}$$

$$\vec{F^{\nu}} = \frac{1}{2}\rho_f c(r)[C_D(0)\cos^2\alpha + C_D(\frac{\pi}{2})\sin^2\alpha]|\vec{v}|\langle v_{x'}, v_{y'}\rangle dr \tag{2.17}$$

$$d\tau^{\nu} = \frac{1}{16}\pi\rho_f c^4(r)[\mu_1 f + \mu_2|\dot{\eta}|]\dot{\eta}dr \tag{2.18}$$

$$m_{11} = \frac{1}{4}\pi\rho_f b^2 \qquad m_{22} = \frac{1}{4}\pi\rho_f c^2(r) \qquad I_a = \frac{1}{128}\pi\rho_f[c^2(r) + b^2]^2. \tag{2.19}$$

Here, α is the angle of attack, C_T and C_R are, respectively, the translational and rotational lift coefficients of the wing, $C_D(\alpha)$ is the wing's drag coefficient as a function of the angle of attack, μ_1 and μ_2 are dimensionless coefficients related to the viscosity of the fluid, and f is the flapping frequency. Values for C_T, $C_D(0)$, and $C_D(\frac{\pi}{2})$ for fruit fly and hawkmoth wings were taken from model flapping experiments [67, 68]. Bumblebee measurements were taken from wind tunnel measurements in [69]. Finally, it is also possible to obtain analytic expressions for the components of the aerodynamic torques in the $\hat{\phi}$ and $\hat{\theta}$ directions through

$$\tau_i^{aero} = \int_{r=0}^{r=R}(\vec{r}\times\vec{dF})_i. \tag{2.20}$$

For the calculations presented here, the torques and forces are analytically calculated at 1000 evenly spaced time steps over a single period and average forces and torques are arrived at via numerical integration.

The total lift on the wing is calculated by transforming the force vectors back into the lab frame, in which $\hat{z}$ is the unit vector in the vertical direction. F_z is defined as the magnitude of the $\hat{z}$ component of the total force. In order to make a convenient, non-dimensional measure of the vertical force on an insect, we will subsequently quantify an insect's lift by L, which is defined as

$$L \equiv \frac{2\langle F_z \text{ From One Wing}\rangle}{mg}, \tag{2.21}$$

where m is the total weight of the insect and $g = 9.81\frac{m}{s^2}$. Hence, if $L \geq 1$, the insect is able to produce enough lift to fly.

2.2.5 Modeling Power Consumption

Given a particular morphology and set of kinematics, we also wish to determine the amount of power necessary to produce the desired wing motion. We assume that the energetic cost to the insect is given by the time-averaged positive mechanical power output. This includes both the power necessary to overcome aerodynamic drag and the inertial power required to accelerate the wing's inertia. Additionally, we assume that the cost for negative power is negligible and that the effect of elastic storage, which has been measured to be on the order of 10%, is minimal [43].

We model the power consumption by assuming that motions are powered by rotational actuators located at the base of the wing. Using the Eulerian equa-

tions for the rotational motion of a rigid body and given the assumptions made above, we have that the power output from rotating in angle i (p_i) is given by

$$p_i(t) = \Omega_i[I_i\dot{\Omega}_i - \Omega_j\Omega_k(I_j - I_k) - \tau_i^{aero}], \tag{2.22}$$

where $[i, j, k]$ is a cyclic permutation of $[\phi, \theta, \eta]$, I_i is the moment of inertia when rotating in i, and Ω_i is the angular velocity in the respective angular coordinate. The first two terms of (2.22) represent the power output the wing must overcome in order to move in a vacuum, whereas the final term (using the definition of τ^{aero} from Equations 2.15 and 2.20) is the additional power that must be added in order to overcome aerodynamic forces. This equation implies perfect elastic storage because any time $p_i < 0$, it counts as negative power, meaning that when the wing decelerates, energy is put into the system to be used later when it accelerates. In order to only take positive power into account, we define $P_i(t)$, the positive power consumption necessary to move the wing in angle i, by

$$P_i(t) = \Xi[p_i(t)] \tag{2.23}$$

where $\Xi(x)$ is defined by

$$\Xi(x) = x\Theta(x), \tag{2.24}$$

where $\Theta(x)$ is the Heaviside step function. The total mass-normalized power to perform the wing motion, P^*, is then given by

$$P^* = \frac{P_\phi + P_\theta + P_\eta}{\text{insect mass}} \tag{2.25}$$

2.2.6 Model Validation

To test the compatibility of our model with results obtained from 3-D Navier-Stokes simulations, we look at the cases of a fruit fly, a bumblebee, and a hawkmoth flying with a horizontal stroke plane ($\theta_m = \theta_0 = 0$) and a sinusoidally

Table 2.2: Morphological and kinematic parameters used for optimization and validation

Insect	$M(mg)$	$M_{wing}(mg)$	$R(mm)$	$\bar{c}(mm)$	$I_{wing}(g \cdot cm^2)$
Fruitfly	.72	8.6×10^{-4}	2.02	.67	$.80 \times 10^{-8}$
Bumblebee	175	.46	13.2	4.02	$.17 \times 10^{-3}$
Hawkmoth	1648	47	51.9	18.26	.184
Insect	$f(Hz)$	ϕ_m	C_T	$C_D(0)$	$C_D(\pi/2)$
Fruitfly	254	75^o	1.833	.21	3.35
Bumblebee	116	58^o	1.341	0	2.93
Hawkmoth	26.3	60.5^o	1.678	.07	3.06

varying azimuthal angle (corresponding to $K \to 0$ in (2.10)). Here, we utilize the same morphological and kinematic data used in Sun & Du (2003) in order to compare results (Table 2.2). As mentioned in Section 2.2.4, C_T, $C_D(0)$, and $C_D(\pi/2)$ are obtained by fitting lift and drag coefficient data observed in previous empirical studies [63, 67, 68] to the forms $C_L(\alpha) = C_T \sin(2\alpha)$ and $C_D(\alpha) = C_D(0)\cos^2\alpha + C_D(\pi/2)\sin^2\alpha$ from Equations 2.16-2.17. It should be noted that these measurements are based off of experiments involving dynamically scaled models of the wings. As in [41], C_R is set to be equal to π for all three insects. α_m, the mid-stroke angle of attack, is chosen to be identical to the values of 44^o, 28^o, and 32^o for the fruit fly, bumblebee, and hawkmoth, respectively, used in [70] for the sake of comparison. Finally, the non-dimensional viscous torque parameters, μ_1 and μ_2, are both set to be equal to .2, which was taken from [42] for cases at similar Reynolds numbers. The values of μ_1 and μ_2 have small effects on the total power, largely resulting from the fact that the power required to overcome translational drag dominates the power required to overcome viscous torque. They were both tested in the range $[0, 20]$, resulting in less than 1% change in both lift production and power consumption. Additionally, since [70] assumes that the contribution of rotational power is negligible, P_η is taken to be 0 for this section of the paper only.

Table 2.3: Comparison between quasi-steady and CFD (P^* in units of $\frac{W}{kg}$)

Insect	**Quantity**	**Quasi-Steady**	**CFD (Sun & Du)**
	L	1.003	1.0
Fruitfly	P^*	24	30
	L	.95	1.0
Bumblebee	P^*	53	56
	L	1.15	1.0
Hawkmoth	P^*	44	46

As seen in Table 2.3, the quasi-steady model agrees with the CFD calculations within approximately 15%. For the fruit fly, L is predicted almost exactly, but the specific power, P^*, is slightly underestimated. In the case of the hawkmoth, though, the specific power agrees well with the CFD calculation and the amount of lift predicted is off by about 15%. For the bumblebee, both the lift and power agree well with the CFD results.

2.2.7 Optimization

Given the model of forces and biomechanics described in the previous sections, we optimize the kinematic parameters listed in Table 2.1 in order to minimize the mass-specific power output of an insect (P^*) with a fixed morphology. This is a nonlinear optimization process with the constraint that $L \geq 1$. The problem also is constrained by the physical limitations on the parameters listed in Table 2.1 (i.e. $0 \leq \phi_m \leq \pi/2$). This constrained optimization was converted into a more tractable problem by defining the fitness, F, corresponding to parameter set Υ by

$$F = P^* + r\Theta(1 - L) + s \sum_{j \in \Upsilon} \frac{|\zeta_j|}{\text{Max}_j - \text{Min}_j} \tag{2.26}$$

where $\Theta(x)$ is the Heaviside step function, ζ_j is the distance that parameter j is outside the range specified by Max_j and Min_j given in Table 2.1, and r, s are positive, real parameters which specify the strength of the penalty for violating the lift and physical constraints, respectively. For the optimizations to follow, we use $r = s = 2000$.

The procedure used here is a hybrid of the clustering genetic algorithm (GA) used in [71] for other fluid dynamics applications and a Powell algorithm [72] for local optimization at the end. The GA is started with a population of 200 parameter sets which are then evolved to be grouped in a globally minimal basin. The initial sets are randomly chosen from all possible sets within the range allowed by the values in Table 2.1 in order to avoid biasing. After narrowing the population sufficiently, the simplex algorithm was used to relax each of the parameter sets found via the GA to the local optimum of the basin. All of the results to follow are validated by multiple runs of the algorithm, each of which matched to within the tolerance set for the simplex algorithm (relative tolerances of 10^{-10} for the fitness function and all parameters).

2.3 Optimization Results

2.3.1 Optimized Kinematics

Wing kinematics, force production, and power consumption resulting from the three optimizations are shown in Figure 2.4. Data from the optimizations are listed in Tables 2.4 and 2.5. For the fruit fly, the optimal wing motion is largely flat but slightly U-shaped, qualitatively similar to the observed kinemat-

ics [25, 62]. Additionally, the force production and power consumption are relatively constant along the mid-stroke, dropping off precipitously during wing rotation. For both the bumblebee and hawkmoth motions, however, we see a figure-8 motion with a larger stroke deviation ($\sim 10^o$) and less constant forces and powers during the mid-stroke. The latter effect is especially pronounced for the power consumption.

Additionally, the frequencies of the optimized kinematics are similar to the observed values. For the fruit fly, the optimized frequency of 234 Hz is within the measured range of 210-260 Hz seen in empirical studies [25, 62]. For the two larger insects, although the optimized frequencies are slower than the observed values, there still exists a reasonable agreement between the optimization and empirical data. Speifically, the optimized hawkmoth motion has a frequency of 19 Hz (observed range: 24-26 Hz [64]), and the optimized bumblebee frequency is 122 Hz (observed range: 145-155 Hz [63]).

Finally, for all three insects, the optimal motions are such that they produce nearly exactly enough lift to hover, and not more (to within $mg \times 10^{-15}$). Since additional lift production requires an increase in power consumption, the inequality constraint placed upon the optimization acts more like an equality constraint ($L \equiv 1$ as opposed to $L \geq 1$). More will be said about this later.

Table 2.4: Optimal parameters

	Fruitfly	**Bumblebee**	**Hawkmoth**
$f(Hz)$	234	122	19
ϕ_m	90.0^o	90.0^o	90.0^o
θ_m	3.1^o	12.3^o	8.1^o
η_m	72.7^o	87.0^o	85.3^o
θ_0	$-.65^o$	1.83^o	2.67^o
η_0	90.0^o	-90.0^o	-90.0^o
K	.704	.925	.796
C_η	2.375	1.223	.711
N	2	2	2
Φ_θ	-70.6^o	-102.2^o	-109.2^o
Φ_η	-72.4^o	-91.8^o	-97.9^o

Table 2.5: Optimization results

	Fruitfly	**Bumblebee**	**Hawkmoth**
$L-1$	2.9×10^{-15}	2.5×10^{-16}	6.4×10^{-16}
$\langle F_z \rangle / \langle Drag \rangle_{rms}$	1.80	1.94	1.58
$\langle P^{Aero} \rangle / \langle P^{Inertial} \rangle$	3.74	.53	1.25
$P^*(\frac{W}{kg})$	14.6	39.2	26.6

2.3.2 Kinematics with Constrained Stroke Amplitudes

A possible explanation for the optimized frequencies being consistently lower than the observed values lies within the fact that for all three optimizations, the stroke amplitude, ϕ_m is at the maximum allowed value of 90^o. Intuitively, this makes sense, as a larger stroke amplitude allows for a larger percentage of the period to be spent in the mid-stroke, where most of the lift is generated. Hence, this additional generation of lift per period allows for a slower flapping frequency. Insects, however, are limited by additional constraints which do not exist in our model. In particular, the cost for moving the wing is most likely a non-constant function of the stroke position (i.e. the cost required to move a wing from $\phi = -15^o$ to $\phi = 15^o$ is different than the cost to move from $\phi = 60^o$

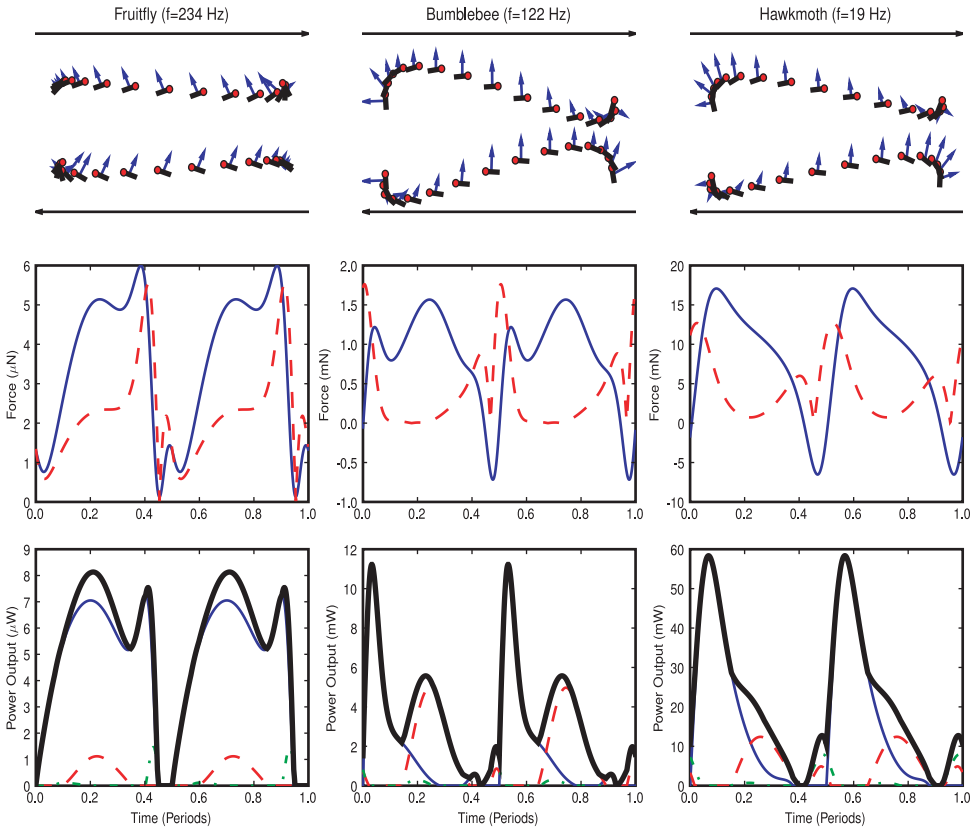

Figure 2.4: Kinematics, forces, and powers for optimized wing motions. Top – The motion of the wing chord with dots representing the wing's leading edge. The arrows are the instantaneous forces on the wing. Middle – The vertical forces (solid line) and the magnitude of horizontal (dashed line) forces on the wing over one flapping period. Bottom – The total power output (thick solid line) and its three components: P_ϕ (thin solid line), P_θ (dashed red), and P_η (alternating).

to $\phi = 90^o$). Hence, it is of interest to observe the wing motions that result from optimizing the kinematics while keeping ϕ_m fixed to the empirically observed value (75^o for the fruit fly, 58^o for the bumblebee, and 60.5^o for the hawkmoth).

Results from this optimization are shown in Figure 2.5. For all three insects, the decrease in ϕ_m results in a higher flapping frequency, as expected. Specifically, the frequencies resulting from this optimization with a constrained stroke amplitude were 268 Hz for the fruit fly, 164 Hz for the bumblebee, and 24 Hz

for the hawkmoth. Each of these values are within or only slightly above the empirically observed range of frequencies. Also, it should be noted that although small changes exist between the other stroke parameters, the wing motions, forces, and powers resulting from optimizing with a constrained stroke amplitude do not differ qualitatively from the non-constrained case. In particular, for the case of the hawkmoth (Figure 2.6), we see good agreement between the optimized solution and the wing stroke empirically observed by [64]. The primary disagreements between the optimized and the observed strokes occur due to the lack of asymmetry in our kinematic equations. However, for all three angles, there is quantitative agreement for the amplitudes, phases, as well as the frequency, of the motion.

2.4 Sensitivity of Optimal Solutions

Given the optimized kinematics presented in Figure 2.4 and Table 2.4, we now investigate the effects of perturbing various parameters on their lift and power production. This is done to gain insight into why these particular parameters are optimal, as well as to understand more fully the structure of the optimal basin. Figure 2.7 shows the dependence of L and P^* for each of 9 parameters for the hawkmoth, assuming all the other parameters remain constant at their optimized values. Only the hawkmoth analyses are shown here due to the qualitative similarity exhibited between the sensitivity analyses of all three of the insects studied here.

What we see from these single-variable sensitivity analyses is that although interplay exists between the parameters, the location of the optimal value can be explained by only three categories of behavior. The first category contains

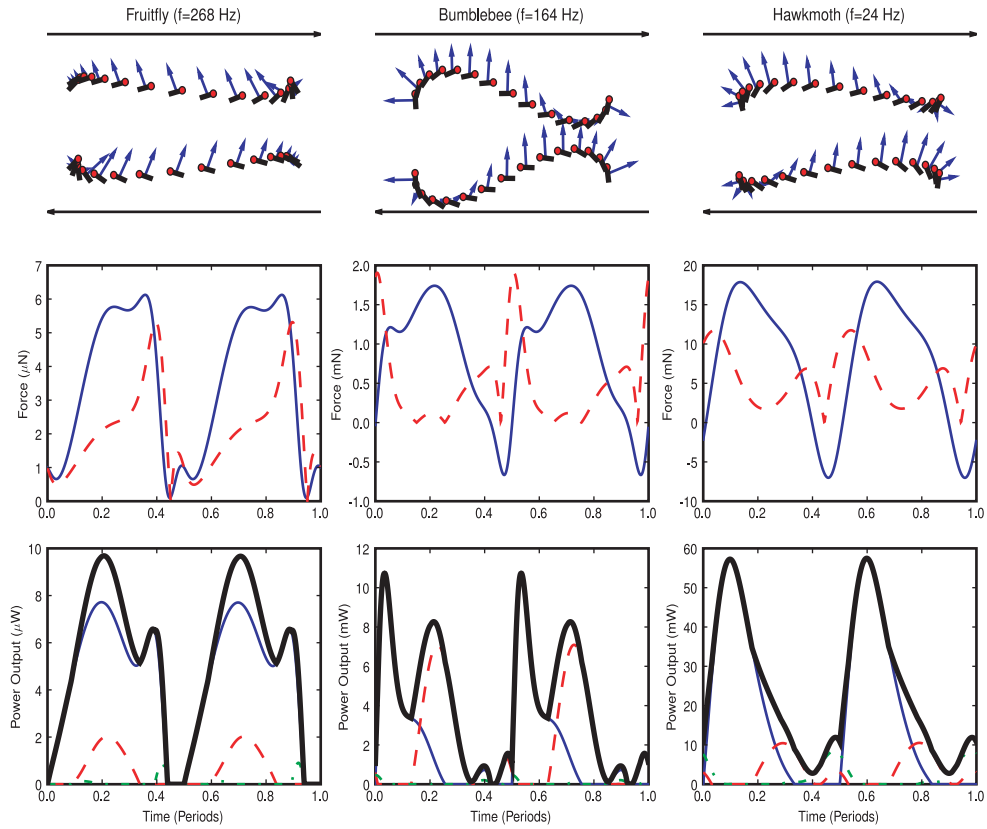

Figure 2.5: Kinematics, forces, and powers for optimized wing motions with constrained ϕ_m (layout is the same as in Figure 2.4).

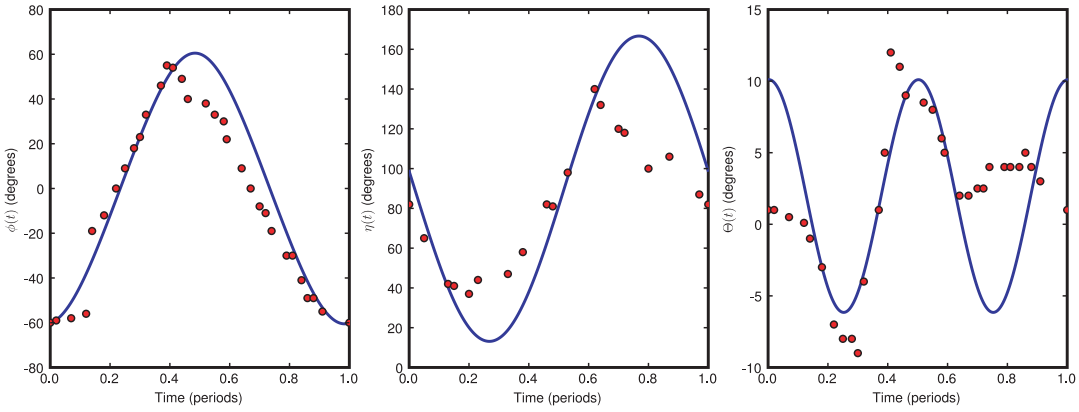

Figure 2.6: Comparison between optimized (solid line) hawkmoth hovering kinematics and observed data (dots) from Willmott & Ellington, *J. Exp. Bio.*, 1997.

parameters where a conflict between lift production and power consumption affects the optimal value. These three parameters (ϕ_m, θ_m, and η_m, Figure 2.7A-C) are the amplitudes in the three angular degrees of freedom. For the first two cases of ϕ_m and θ_m, an increased amplitude corresponds with more lift production, but also results in strokes which require more power. Hence, given our optimization's constraint that $L \geq 1$, the optimal values for these parameters will be set by finding the minimal value where $L = 1$. This helps to explain the result in Section 2.3.1 where the inequality constraint of our optimization becomes an equality constraint. Any deviation from the manifold where $L = 1$ would result in either a violation of the lift constraint or an increase in power consumption. Similarly, for η_m, we see that for large values of the amplitude (corresponding to small mid-stroke angles of attack), both the lift and power decrease monotonically. Hence, the optimal value of η_m is the largest value such that the lift constraint is met.

The second category contains parameters where the optimized value is at or near the global minimum with respect to P^* (namely, η_0, C_η, Φ_η, and K, Figure 2.7D-G). Variations away from the optimum in these parameters tend to cause significant increases in power consumption. The exception to this is K, but the optimal value is the global minimum in P^* due to the relative flatness of the dependence of L on the parameter. It also should be noted that all four of these parameters are directly related to the speed and phase of wing rotation.

The final category of parameters are those where L is maximized irrespective of power consumption (θ_0 and Φ_θ, Figure 2.7H-I). For these parameters, both related to $\theta(t)$, the relatively small effect these parameters have on P^* gives more importance to providing a maximal amount of lift.

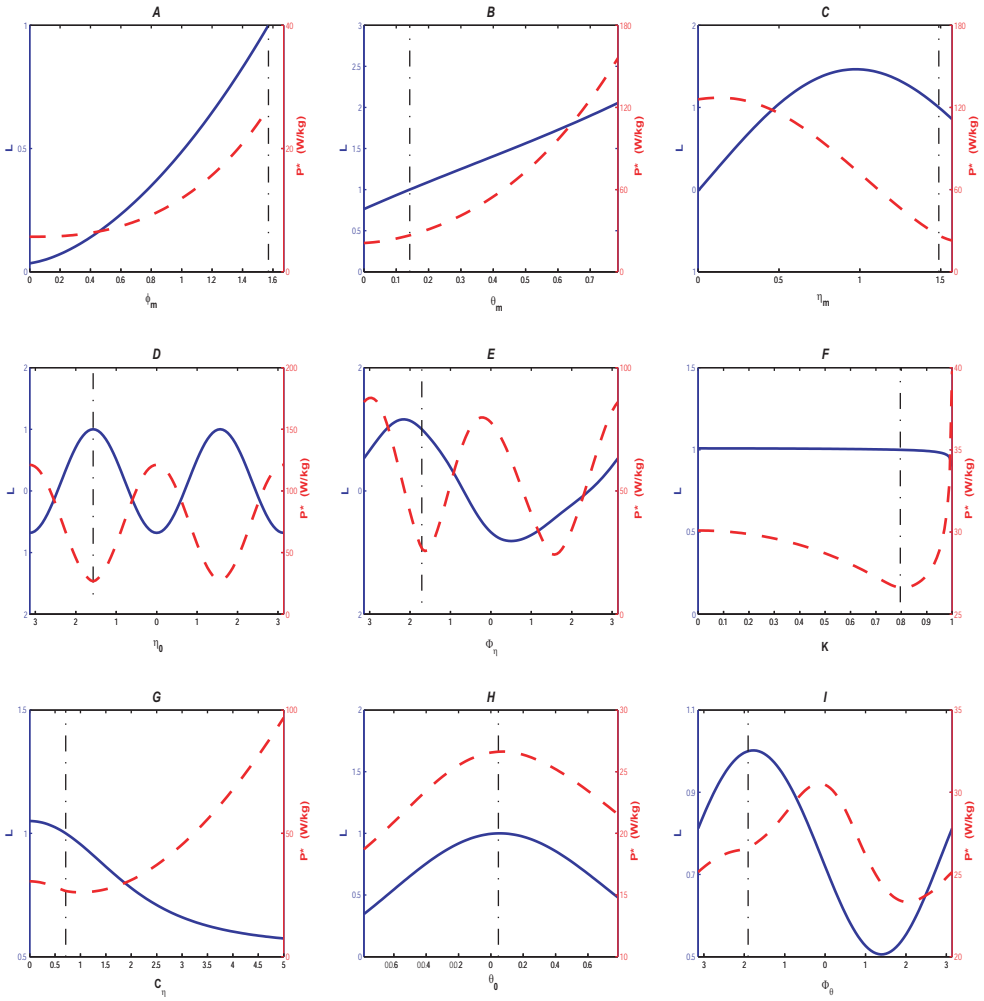

Figure 2.7: Single parameter sensitivity analyses for hawkmoth. The solid lines represent show L as a function of the given parameter, and the dashed lines represent the variation of P^*. The alternating vertical lines indicate the position of the optimal solution for the parameter in question.

2.5 Rotational Power and Passive Wing Rotation

An interesting feature of the optimized kinematics is that the cost to pitch the wing corresponds to only a small fraction of the total power consumption (1.4% for the fruit fly, 4.5% for the bumblebee, and 5.6% for the hawkmoth). In particular, the optimal kinematics are such that the stroke maintains a constant leading edge throughout a flapping period, as opposed to switching the leading edge

during wing rotation (Figure 2.8). This observation matches empirically observed results for nearly all insects. Previously, the use of a single leading edge was assumed to occur for structural (as opposed to aerodynamic) reasons, as the leading edge of the wing must be relatively thick compared to the trailing edge, since the additional fluid forces which occur at the trailing edge lead to greater stress on that portion of the wing [73]. Hence, a wing can be lighter if only one of its edges needs to be made of the thicker material that a leading-edge side requires. Our model, however, assumes a symmetry between the two edges of the wing. Hence, the fact that the wing keeps the same leading edge through the optimization implies that there is another reason for this rotation. What appears to occur is a passive-dynamic relationship between the inertial forces required to flip the wing over and the fluid forces acting on the wing during rotation. This effect is seen in Figure 2.7D, where both maximum lift production and the minimum power consumption occur at values where the stroke maintains a constant leading edge ($\eta_0 = \pm\pi/2$). Conversely, the lift is minimized and the power maximized at $\eta_0 = 0$, corresponding to an alternating leading edge.

The sensitivity analysis, however, is not a full explanation for the optimal solution using a single leading edge, as the interplay between different parameters may allow for more efficient strokes with alternating leading edges. To gain a better understanding, we run the same optimization described in Section 2.2.7 but with the additional constraint that the leading edge must switch at some point during the stroke. In other words, for every flapping period, there exist times t_1 and t_2 such that $\vec{v}(t_1) \cdot \vec{c}(t_1) < 0 < \vec{v}(t_2) \cdot \vec{c}(t_2)$ where $\vec{v}(t)$ is the velocity vector at time t and $\vec{c}(t)$ points in the direction of the chord.

Performing this optimization (Figure 2.9), we observe that maintaining a constant leading edge results from the interplay between inertial and aerody-

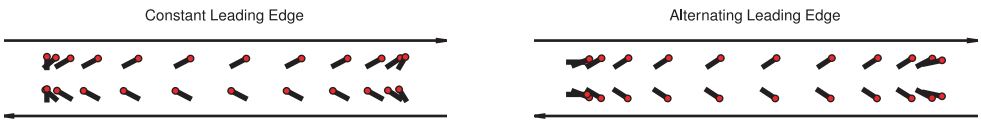

Figure 2.8: Examples of wing kinematics with differing wing rotation strategies

namic powers. Specifically, the two powers largely cancel each other for the case of a single leading edge, whereas they are additive in the case of the optimal kinematics for alternating edges. The amount of power necessary for rotation increases by factors of 190%, 88%, and 76% for fruit fly, bumblebee, and hawkmoth, respectively, when an alternating leading edge is mandated. These differences in efficiency can be explained by the timing of the aerodynamic forces acting on the wing. For the case of using a single leading edge, the aerodynamic torque facilitates the turning at the onset of rotation – the fluid is doing work on the wing. Then, during the second half of the wing rotation, the aerodynamic and inertial forces are again antithetical to each other, the relatively weak aerodynamic force slightly aiding the wing rotation's deceleration into the midstroke. For the case of alternating leading edges, however, the wing must do work on the fluid while the wing attempts to accelerate and does work on the fluid while it decelerates. An energetic benefit exists on neither the onset nor the resolution of rotation, resulting in the increased power consumption observed in Figure 2.9.

2.6 Summary

In this chapter, we have found and analyzed the optimal wing kinematics for the hovering flight of three insects of widely varying masses through the use of a quasi-steady model of fluid forces on a thin plate and a hybrid optimizing

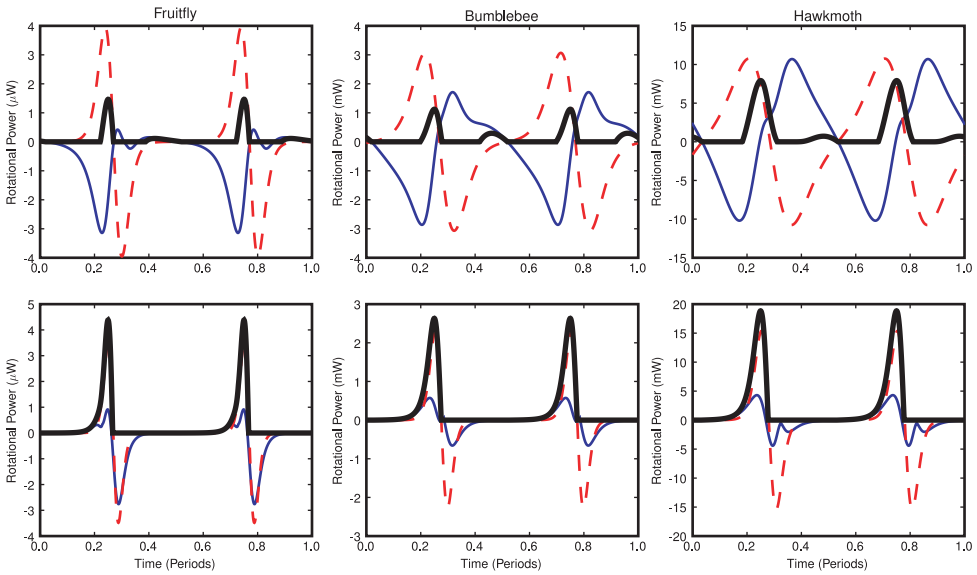

Figure 2.9: Rotational power output for optimized wing motions. Displays the rotational power necessary to pitch the wing for an optimized stroke with either a single (top) or alternating (bottom) leading edge for the three insects (from left to right: fruit fly, bumblebee, and hawkmoth). The thick solid line is the total rotational power consumption (P_η), the thin solid line represents the aerodynamic power, and the dashed line is the inertial power. The kinematics from the top three plots are identical to those in Figure 2.4, whereas the kinematics in the bottom plots were generated by running the optimization procedure with the added caveat that the leading edge forced to switch at some point during the stroke.

algorithm. These solutions minimize power consumption while still producing enough lift to sustain hovering flight. We found that these kinematics capture several qualitative aspects of observed flight and predict the observed flapping frequencies well. These agreements become more striking if we fix a parameter by constraining the stroke amplitude, ϕ_m, to its empirically observed value. We also have performed sensitivity analyses of the optimal solutions. From these analyses, we determined the import and effects of varying the kinematic parameters in our model. Finally, we observed that the optimal motions used a single leading edge throughout the stroke, as opposed to alternating edges during wing rotation. Previously thought to occur for purely structural reasons,

we found that maintaining a constant leading edge is advantageous due to an interplay between inertial and aerodynamic power.

There, of course, are further extensions of the investigations described in this chapter that are intriguing. One of these potential lines of inquiry is to explore the effect of the fitness landscape surrounding the optimal solution. More specifically, one can ask whether the types of observed variations of wing kinematics in a population can be predicted by finding the compliant directions in the parameter space. We shall say more about this later in Chapter 5.

Underlying any analysis of the landscape however, is the parameterization used to probe the system. In this chapter, we have utilized a parameterization of our Euler angles that allows for a wide range of possible wing strokes, but eliminates the problem of singular kinematics (i.e. the wing flipping infinitely quickly) that results from calculus of variation methods, as well as the existence of copious local optima that arises from parameterizing the wing strokes via a Fourier series. Additionally, the parameters used here are all directly relatable to meaningful physical quantities. Despite these benefits, however, there is something slightly unsatisfying about eliminating wide swaths of wing stroke space with a quiet flick of the wrist. Hence, it would be interesting to perform a more thorough analysis as to how the results of the analysis depends on the parameterization used.

Also possible is to utilize statistical methods, such as those performed in [74] on *C. elegans*, to derive a more natural parameterization of the space of available wing motions. In the cited study, long time series of observed worm motions were found to be accurately represented as a linear combination of a small number of "eigenworms," hence providing an experimentally-derived description of the organism's motion. While the direct application of this type of approach

to flying insects is currently data-limited, it provides an intriguing option for future endeavors.

Lastly, recent work [27, 75] has suggested that the wing pitch for hovering flight is only passively controlled. In other words, given a particular translational wing motion ($\phi(t)$ and $\theta(t)$) and some set of morphological parameters, the wing rotation angle ($\eta(t)$) is given by some differential equation. Accordingly, a possible study would be to perform a similar optimization as done in this chapter, but to prescribe only the stroke plane and stroke plane deviation angles, allowing the wing rotation to occur according to the aforementioned model. In this way, a more natural restriction of the parameterization might be achieved, as the passive nature of the wing flipping could cause the optimization algorithm to avoid the singularities of infinite rotation.

CHAPTER 3

HRMT: AUTOMATICALLY TRACKING INSECT KINEMATICS THROUGH VISUAL HULL RECONSTRUCTION

3.1 Introduction[1]

Insects are capable of performing amazing maneuvers in flight, from a graceful ascent to a dramatic escape to making a 180^o turn in a manner of a few wing beats. Despite this ability, though, the differences observed between wing strokes are remarkably subtle – a change of only a view degrees in the angle of attack can be the difference between hovering and the aforementioned violent turn [75,76]. As a result, in order to study these creatures' flights experimentally, one needs a method of recording the insects wing kinematics with impressive accuracy and high enough throughput to allow for statistical analysis. In addition, many behavioral studies of animals which co-opt methods from statistical physics are data-hungry, again requiring large amounts of kinematics to be provided [74].

Therein lies the rub, however, as accurate insect flight data is quite difficult to obtain. Until quite recently, almost all methods of tracking insects (or any other animal, for that matter) in free-flight involved a large amount of manual input [25, 77–79]. This basic idea of this is seen in Figure 3.1, which displays a schematic of the manual tracking process. Essentially, what occurs is that a model fly (in this case, consisting of three ellipsoids for the head, thorax, and abdomen and two, thin elliptical plates for wings) is superimposed upon a set of silhouettes generated from camera views. This model is then tweaked, usually

[1]Much of the work discussed in this chapter was originally presented in Ristroph, Berman, Bergou, Wang, & Cohen, Automated hull reconstruction motion tracking (HRMT) applied to sideways maneuvers of free-flying insects, *J. Exp. Bio.*, **212**, 1324-1335 (2009).

by a bleary-eyed (under)graduate student, through manipulating its degrees of freedom until it is within the observed shadows. After significant training, an expert user can track a frame in about 2-3 minutes. Given a camera frame rate of 8,000 Hz and a flapping frequency of about 250 Hz (typical for a fruit fly), it takes about two days (no sleeping, bathroom breaks, etc.) of human tracking time to finish one 30 stroke flight sequence.

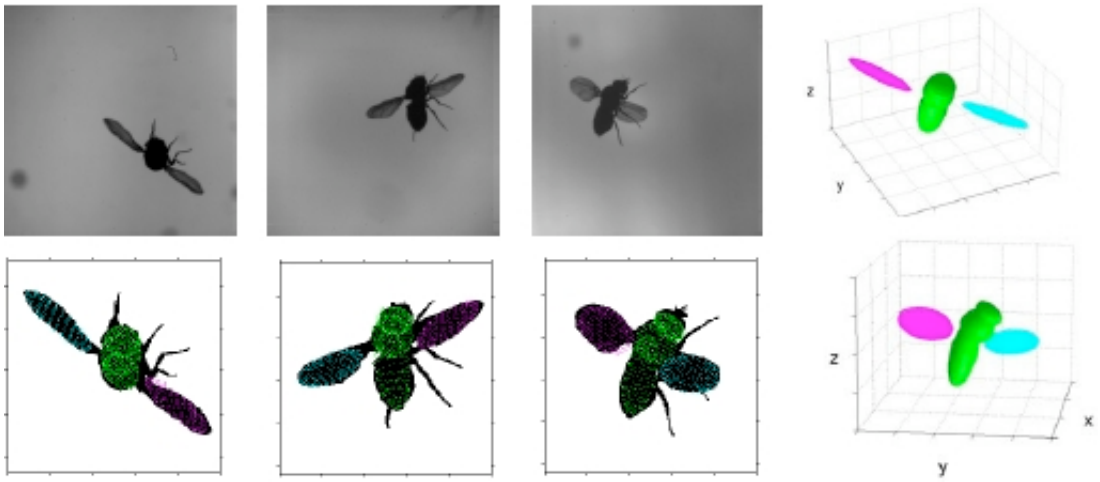

Figure 3.1: Typical example of a manual-based tracker. Raw Images (top left) are thresholded and a model fly is placed on top (the superposition is on the bottom left and a rendering of the model insect is on the right). A human user then adjusts the model until it coincides with the shadows.

Accordingly, better solutions need to be found. Ideally, a fully automated method is desired so that data can be obtained without intense human labor. This, as one might imagine, is far easier said than done. Perhaps the most well-developed solution to this problem is to place markers at various positions on the insect and then use methods from photogrammetry to track the fly [80]. Unfortunately, placing markers on the insect is problematic, as it is difficult to perform consistently. More fundamentally, though, the lighting conditions for most experiments are such that silhouettes are obtained (and not reflected flight)

– meaning that we might not be able to distinguish the marker anyway. For larger insects, such as hawkmoths, this method holds promise, though.

Another technique which has been used to track blowflies has been to place search coils on the insect and find the position and orientation of the fly body through induced currents on external coils [81]. Alas, this is not satisfactory for our requirements either, as it only tracks the body (and not the wings). Also, the method appears to be somewhat intrusive, perhaps affecting flight behavior.

Applied recently for tracking zebrafish and fruit flies [82,83], is to use a state-space Bayesian statistics method which takes as an input a detailed model of the insect morphology and a training set of data which is tracked a priori. While this method is relatively automated, additional difficulties are posed, however. First, the aforementioned detailed model needs to be readjusted for each different insect tracked, introducing a somewhat hefty overhead for each flight sequence. Secondly, the observed errors for insect wing kinematics in this method are quite large ($\approx 17^o$ for the angle of attack). Since flight maneuvers can be caused by variations of only a few degrees, this level of error is unacceptable.

So why is designing an automated tracking algorithm so difficult? One way to see this is shown in Figure 3.2. Take, for example, a sphere being viewed by three orthogonally placed cameras. The silhouettes this object generates are three circles of equal radius. Applying the inverse operation, however, we get that there are an infinite number of possible solids which are consistent with the shadows. This non-uniqueness proves to be a fundamental difficulty with developing any automated tracker. In order to track an object from its shadows, external geometric information is required.

The method we describe in the following sections alleviates some of the inherent difficulties in tracking from image shadows by taking the maximal vol-

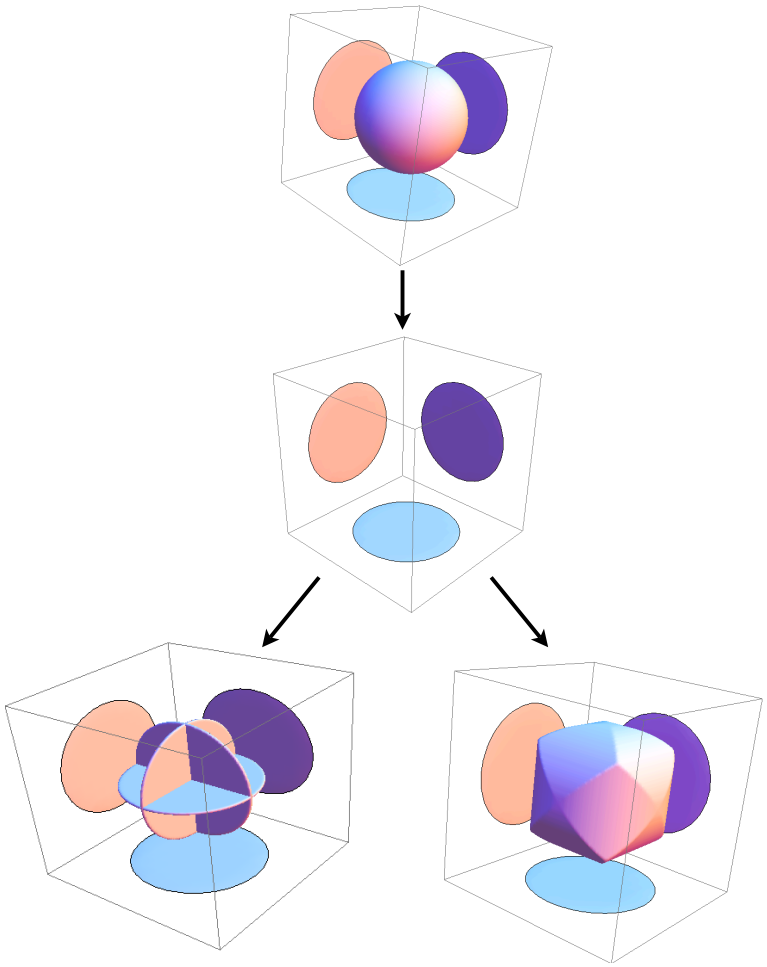

Figure 3.2: Demonstration of the non-uniqueness of volume given silhouettes. In this simple example, we can see that the shadows produced by a sphere (three circles) could produce infinitely many possible solids, including a solid of volume zero (three intersecting disks) and the maximal volume solid, the intersection of three perpendicular cylinders (a Steinmetz Solid, to be precise). The latter of these is referred to as the visual hull of the shadows.

ume which is consistent with the silhouettes (deemed the object's visual hull) and using the geometric knowledge we possess about a fruit fly. As a result, we have deemed this algorithm HRMT (Hull Reconstruction Motion Tracking). We will first describe the experimental apparatus which obtains these images, followed by a run-through of the tracking algorithm, and will finish with some sample results.

3.2 Experimental Apparatus

The apparatus used to perform our investigations is seen (in schematic form) in Figure 3.3. Here, three high-speed cameras (Vision Research Phantom v7.1 CMOS digital cameras), filming at 8,000 frames/s with 512×512 resolution are placed along orthogonal axes, resulting in a cubical intersection which serves as the filming volume. This volume is aligned via the use of precision rails mounted on an optical table. The size of the filming volume varies between about 2-20 cm^3, depending on the experiment in question.

Located about the filming volume is a plexiglass flight arena in which insects can be placed. This portion of the apparatus is designed to be modular so that differing experiments can be done. For example, in Chapter 4, two amendments are added to the flight chamber to engender forms of ascending behavior. Additionally, since fruit flies (our target of choice) are only about 3mm in length, we magnify by placing an optical bellows (Nikon PB-5) and a zoom lens (Nikon Macro-Nikkor 28-105mm) on each of the three cameras.

As the short exposure times, high magnification, and large depth of field all limit the amount of light in our filming volume, we need to have accordingly bright light sources to satiate the harsh desires of photon counting statistics. Our particular strategy for ameliorating this is to backlight the region with red LEDs, focused via a lens. The LEDs are a viable solution as they provide a great deal of light without creating vast amounts of heat, which could affect the observed flight sequences. Red is the color of choice here, as fruit flies cannot see at such wavelengths [84]. As a result of this method of lighting, however, the images we capture are silhouettes, since the cameras only see blockages in the light, as

opposed to reflected light. As previously alluded to, this fact somewhat limits one's options when attempting to track these creatures. Our solution to this dilemma will be described in the sections to follow, however.

Finally, we describe the triggering mechanism used to initiate recording in the cameras. In order to reduce effects from near-wall flight, such as raised legs or interface-affected aerodynamics, the filming region comprises only a small portion of the flight enclosure (less than 1%). Hence, to improve our data throughput, a laser-triggering mechanism is used. To be more concrete, this apparatus (shown in Figure 3.3b) consists of two red HeNe laser beams impinging on photodiodes. The radii of these beams are expanded (via a Galilean expander) such that they cover the entire filming region. The diodes are connected to a coincidence circuit which triggers the cameras when an insect blocks both laser signals.

All told, this apparatus provides the raw material for our tracking algorithm, which shall be described in the remainder of this chapter.

3.3 Registration

The initial step for our tracker is to take the three orthogonal camera views and to find the minimal bounding box which encloses the fly in each of them. This data will be used to both align the cameras and to reduce the computer time required to reconstruct the hull. In order to find the bounding box, we first need to threshold the fly silhouette from the gray background. This is done by manually setting a threshold value; however, we find that the same threshold value applies for all of the sequences we have tracked (i.e. it is a tweaked parameter, but only needs tweaking once). As seen in Figure 3.1, this results in a crisp im-

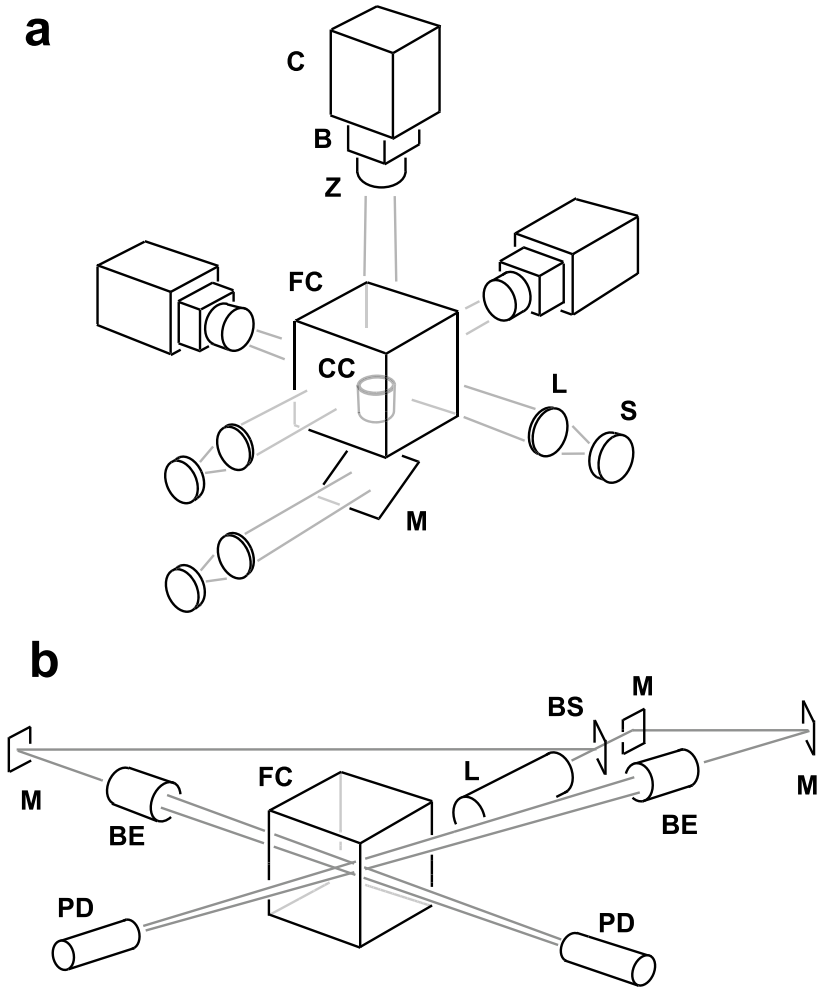

Figure 3.3: Experimental set-up. Part **a** shows the camera (C) arrangement focusing on a flight chamber (FC) via optical bellows (B) and zoom lenses (Z). The filming region is lighted via red LEDs (S) focused through lenses (L). Part **b** of the figure displays the triggering mechanism, in which the laser light (L) comes upon a beam splitter (BS), a series of mirrors (M) and beam expanders (BE) before crossing in the filming region and impinging on two photodiodes (PD). When the intensity measured at the diodes varies beyonf a threshold, the cameras initiate filming (*figure by Leif Ristroph*).

Figure 3.4: Typical images from the experimental apparatus. The three stills shown are simultaneous frames from the (left to right) XY, XZ, and YZ camera views.

age with little noise on the edges. Given the thresholded image, calculating the bounding box is simply a matter of finding the maximum and minimum pixel values in each direction. Hence, performing this analysis for all three camera views, we have two measurements for every one of the extremal values (x_{min}, x_{max}, y_{min}, etc.).

We then can use the bounding boxes to fix the small errors remaining that might have occurred since the cameras and the laser triggers were more recently aligned. In essence, we scale and translate the bounding boxes in order to correct for misalignments in camera shift or zoom. For example, to register the pixels along the vertical direction, we shift and scale the images from one of the horizontally pointed cameras such that its vertical coordinate is consistent with the image from the second horizontally pointed camera. The image from the first image is vertically shifted such that the top of its bounding box is aligned with the top of the bounding box from the reference view. We then stretch or contract the first image to match the zoom of the second. This procedure is further iterated to make corrections in the x and y directions. Typically, we find that the images need to be scaled by less than 1% and scaled by less than 5 pixels to achieve registration. Finally, in order to achieve consistent registration for each

movie, we find the average shift and scaling values for the whole sequence, and apply the resulting values to all of the images. This provides the raw material on which our hull reconstruction works.

3.4 Construction of the Visual Hull

From the three aligned silhouettes, we now construct a visual hull [85] via a method similar to that used in [34]. The visual hull of a set of silhouettes is formally defined as the maximal volume which is exactly consistent with all of the silhouettes. Moreover, it can be shown [34] that the object which formed the observed silhouettes must be completely inside the hull. This implies that given our three orthogonal camera views, the visual hull must give us a volume which entirely encloses the fly.

There still remains, however, the task of constructing the hull from the data. We achieve this via the Sparse Pixel Occupancy Test (SPOT) algorithm [34]. Essentially, the concept behind this technique is to group the voxels of the space we are interested, $\{v_{ijk}\}$, into $N \times N \times N$ cubes of voxels, each of which will be deemed w_{ijk}. This coarse-graining is done for two reasons. First, it reduces the effects of getting false positives around the border of the hull – namely, the inclusion of voxels which are likely the result of thresholding noise. Secondly, it increases the speed of the reconstruction, as the number of voxels that need to be evaluated is cut by a factor of 2^N (since processing time turn out to not limit us here, however, this is truly a secondary concern). Given $\{w_{ijk}\}$, the set of coarse-grained voxels within the bounding box found in Section 3.3, and two parameters, Q and Q_ϵ, we find the visual hull, H, as described in the pseudocode below:

$H = \emptyset$

for all $w \in \{w_{ijk}\}$ **do**

  $c = 0$

  for $i = 1, .., Q$ **do**

    Select $v_{ijk} \in w$ at random

    if v_{ijk} is consistent with all silhouettes **then**

      $c \rightarrow c + 1$

    end if

  end for

  if $c \geq Q_\epsilon$ **then**

    $H \rightarrow H \cup w$

  end if

end for

For our tracker, we use $N = 2$, $Q = 8$, and $Q_\epsilon = 5$. Or, in other words, we break the space into $2 \times 2 \times 2$ cubes, sample all of the eight voxels from each one, and if the majority of the non-coarse-grained voxels are consistent with the silhouettes, we add the cube to the hull. When this algorithm finishes, our hull reconstruction returns the cartesian coordinates of the centers of each of the coarse-grained voxels which are later used to find the body position and orientation vectors, as described in the remaining sections in this chapter. A visualization of the hull reconstruction process can be seen in Figure 3.5.

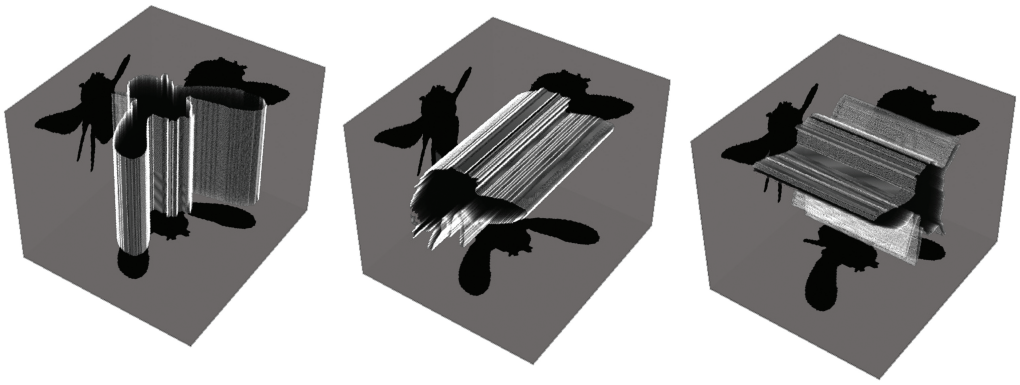

(a)

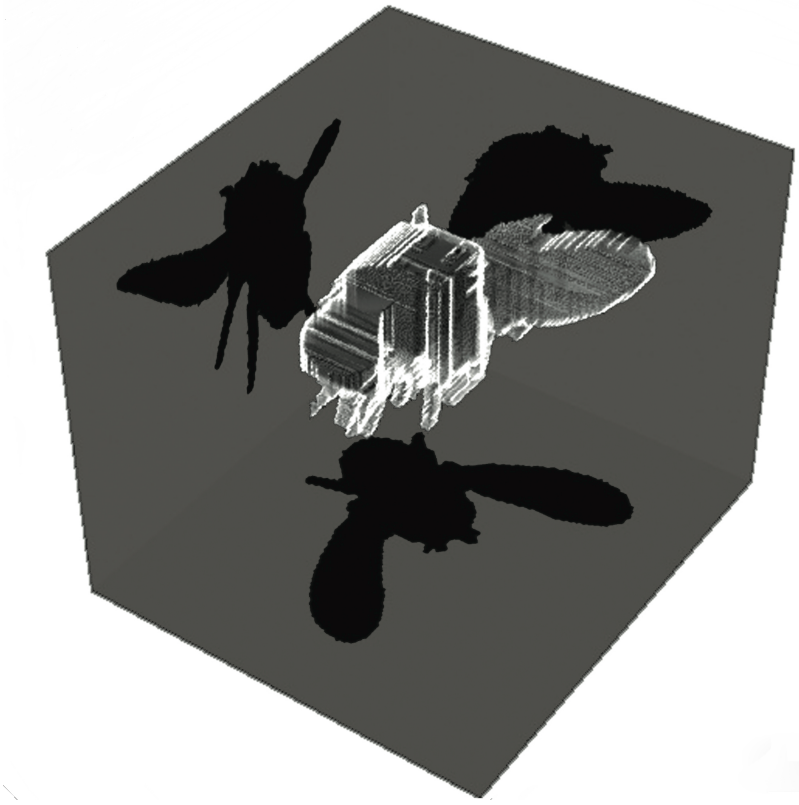

(b)

Figure 3.5: Visualization of the hull reconstruction process. Three cookie-cutter-like slices are taken through the filming volume, resulting in the 3D volume displayed in the lower plot (*visualizations by Attila Bergou*).

3.5 Clustering of the Body and Wings

GIven the collection of voxels attained through the method described in Section 3.4, we now wish to determine which voxels belong to the body, and which voxels belong to each of the two wings. The is achieved by grouping the voxels into minimal Euclidian clusters via the k-means algorithm [86]. Basically, given a set of N points, $\vec{x}_i$, and a fixed number, k, of centroids, $\vec{\mu}_j$, k-means finds the locations of each $\vec{\mu}_j$ and assigns each $\vec{x}_i$ to a centroid such that

$$C = \sum_{j=1}^{k} \sum_{\vec{x}_i \in S_j} \|\vec{x}_i - \vec{\mu}_j\|^2 \tag{3.1}$$

is minimized. Here, S_j is the set of all points assigned to the centroid μ_j. The most primitive version of this algorithm starts with some initial partition of the data, $S^0_{1,\ldots,k}$, then calculates an initial set of centroids, $\vec{\mu}^0_{1,\ldots,k}$, for each partition. The set is then repartitioned such that each data point is assigned to the nearest centroid, and then the process continues iteratively until a convergence criterion is met. Improvements have been made on this relatively simple algorithm since it was proposed, as the version described above has a tendency of getting trapped in local minima. In particular, we use the MATLAB built-in `kmeans` function to perform clustering on our data.

To separate the wings from the body, we perform the k-means algorithm with $k = 4$ on our data[2]. The resulting clusters correspond to the anterior and posterior region of the body, as well as the left and right wings. The two largest clusters, which inevitably correspond to the anterior and posterior regions, are then merged to form the body (see Figure 3.6). The centroids of the body and the two wings are given by the centroids of their corresponding clusters of voxels.

[2]We use $k = 4$ instead of the more obvious choice of $k = 3$, as the latter configuration will often group large portions of the body with the wings.

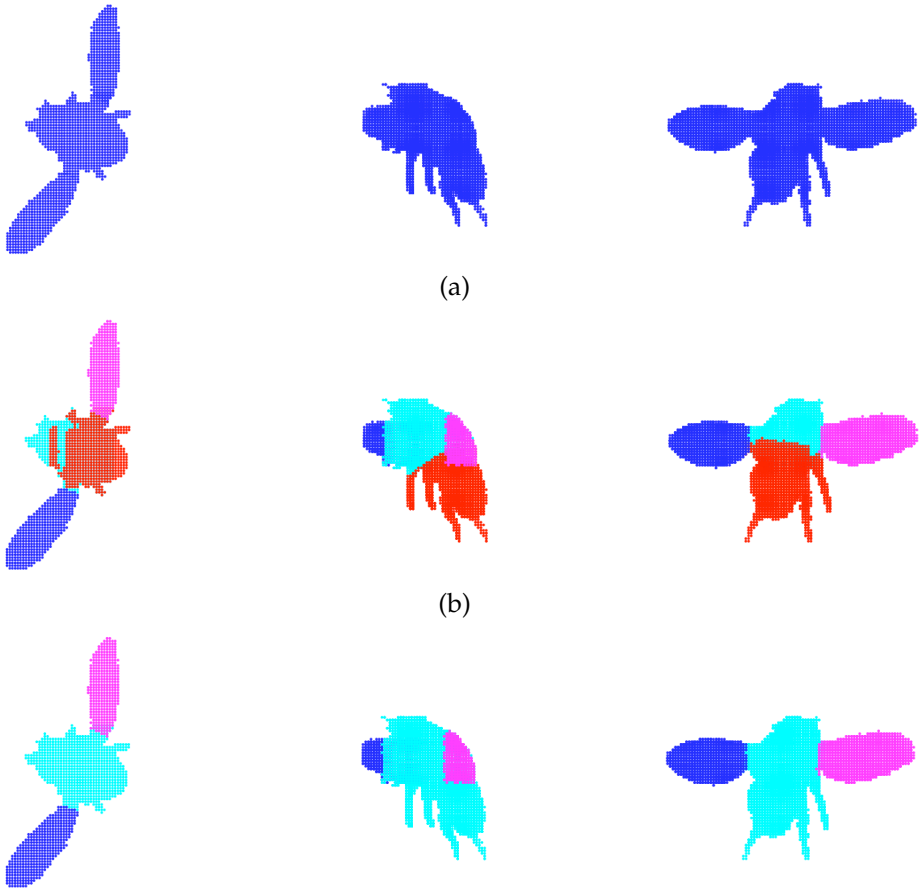

(a)

(b)

(c)

Figure 3.6: Example of the clustering process. The initial hull (part a) is clustered into 4 parts using the k-means algorithm (part b). The two largest clusters are then combined to form the body (part c), leaving two wings and a body.

3.6 Determining Body Orientations

The final portion of the algorithm involves finding the nine angular degrees of freedom for the body (the other three are given by the object centroids found during clustering). Much of this process relies on Principal Component Analysis [35] (PCA), which finds the principle basis vectors of a given data set by finding the eigenvectors of the data covariance matrix. For our tracker, we use

MATLAB's built-in `princomp` function. Since both the body and the wings have one principle axis which is significantly longer than the others (the roll axis in the case of the body, and the span axis for the wings), finding the principle component with the most variation along it provides a robust method for calculating two of the three rotation angles for each object (to be described momentarily). For the roll angle of the body and wings, however, the particular geometry of our visual hull confounds PCA, so more creative measures must be taken. For an overview of the angle and orientation definitions used in this section, see Figure 3.7.

For the initial step, we apply PCA to the cloud of body voxels. Since the body is much longer than it is thick, the first principle component eigenvector gives us the body's roll unit vector, $\hat{A}$. From this vector, we find the body's yaw and pitch angles (ψ and β, respectively) can be found via

$$\psi = \tan^{-1}\left(\frac{\hat{A}_y}{\hat{A}_x}\right) sign(\hat{A}_x \hat{A}_y) \tag{3.2}$$

and

$$\beta = \sin^{-1}(\hat{A}_z), \tag{3.3}$$

where $\hat{A}_x$, $\hat{A}_y$, and $\hat{A}_z$ are the x, y, and z (lab frame) components of the roll axis.

From here, all that remains to characterize the body orientation is to find the roll angle, ρ. The most obvious method for achieving this would be to look at the rotation of the second and third principle component eigenvectors about $\hat{A}$. This, however, proves problematic, as the body is essentially cylindrical. Moreover, the effect of occlusions being added to the visual hull outweighs any small rotational anisotropy which exists. Instead, we use k-means clustering (see Section 3.5) with $k = 3$, which separates the body into, roughly, a head, thorax, and abdomen. We will denote the centroids of these three regions as $\vec{x}_h$, $\vec{x}_t$, and $\vec{x}_a$, respectively. These three points define the plane of bilateral symmetry

for the body whose normal vector, $\vec{n}$, is given by

$$\vec{n} = (\vec{x}_h - \vec{x}_t) \times (\vec{x}_a - \vec{x}_t). \tag{3.4}$$

Since we need a unit vector which is orthogonal to $\hat{A}$ to compute the roll angle, we define $\hat{L}$ via

$$\hat{L} = \frac{\vec{n} - (\vec{n} \cdot \hat{A})\hat{A}}{\|\vec{n} - (\vec{n} \cdot \hat{A})\hat{A}\|}. \tag{3.5}$$

Given all of this, we now can calculate the roll angle, ρ from

$$\rho = \tan^{-1}\left(\frac{\|\hat{L} \times \hat{\psi}\|}{\hat{L} \cdot \hat{\psi}}\right) \tag{3.6}$$

where

$$\hat{\psi} = < -\sin\psi, \cos\psi, 0 > . \tag{3.7}$$

One obvious limitation of (3.6) is that it only allows for roll angles between ±90 degrees. However, we have yet to observe an insect in any of our videos which rolls by more than this amount.

3.7 Determining Wing Orientations

For the first two Euler angles describing the wing orientations, the process is similar to that seen in Section 3.6. Initially, we apply PCA to each set of wing voxels. Since the wing span is significantly longer than the other two principle axes, we can use the first principle component to define the span vector, $\hat{S}$. From there, we can find the yaw and pitch (ϕ and θ) values for the wings via

$$\phi = \tan^{-1}\left(\frac{\hat{S}_y}{\hat{S}_x}\right) sign(\hat{S}_x \hat{S}_y) \tag{3.8}$$

and

$$\theta = \sin^{-1}(\hat{S}_z), \tag{3.9}$$

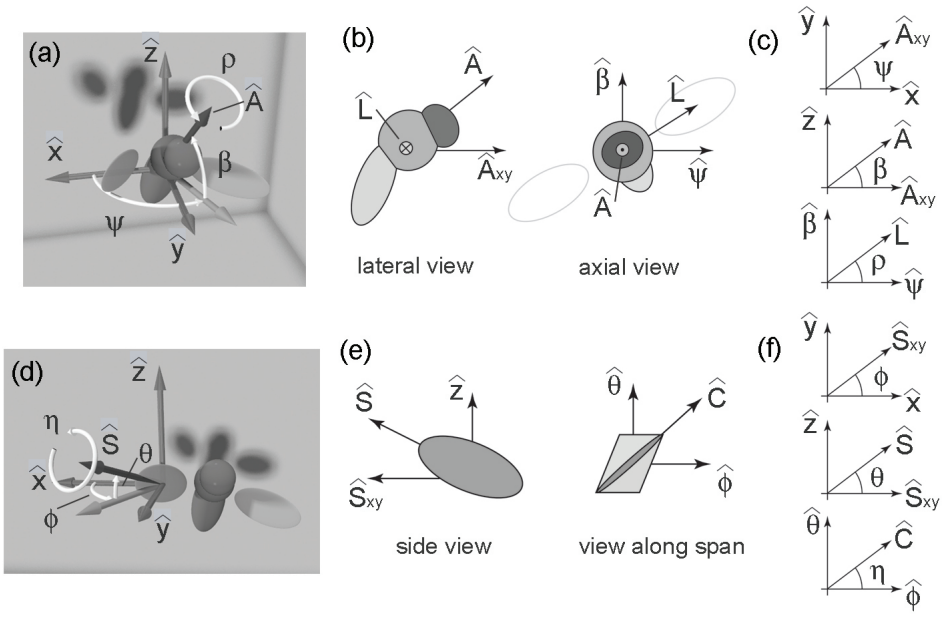

Figure 3.7: Angle orientation definitions (*figure by Leif Ristroph*).

where $\hat{S}_x$, $\hat{S}_y$, and $\hat{S}_z$ are the x, y, and z components of the span axis.

Again, though, the problem remains that we cannot use the results of PCA to obtain the final rotational angles for the two wings. Initially, this is somewhat surprising, as the wings, being almost like thin plates, do not have the same problem of cylindrical symmetry exhibited by the body. The difficulty arises due to the fact that the visual hull of the wing is often augmented due to the body occluding the areas directly above and below the wing. Hence, the wing obtains a finite thickness which is often on a similar length scale to the chord length – thus muddying the results for the second and third components of the PCA. What we do, instead, is to take advantage of the particular geometry of the wings' visual hulls. Namely that near the mid-chord, the hull for a given wing will look like a parallelogram. We assume the chord vector, $\hat{C}$ to be the upwards-pointing unit vector in the direction of the longest diagonal of the parallelogram. More formally, if V_w is the set of all wing voxels for one of the insect wings, we

look at only V_{mid}, defined as

$$V_{mid} \equiv \{\vec{x}_i | \vec{x}_i \in V_w \ \& \ |(\vec{x}_i - \vec{x}_c) \cdot \hat{S}| < \epsilon\}, \tag{3.10}$$

where $\vec{x}_c$ is the wing centroid (found via Section 3.5), and ϵ is a tolerance length, set to be 2 pixels for our tracking algorithm. Having found this set, we find the voxels, $\vec{x}_i$, $\vec{x}_j$, which satisfy

$$\sup_{\vec{x}_i, \vec{x}_j \in V_{mid}} \|(\vec{x}_i - (\vec{x}_i \cdot \hat{S})\hat{S}) - (\vec{x}_j - (\vec{x}_j \cdot \hat{S})\hat{S})\| \tag{3.11}$$

as well as

$$\vec{x}_i \cdot \hat{z} \geq \vec{x}_j \cdot \hat{z}, \tag{3.12}$$

where $\hat{z}$ is the vertically-pointing unit vector. Defining $\vec{q} \equiv \vec{x}_i - \vec{x}_j$, the chord unit vector, $\hat{C}$, is then given by

$$\hat{C} = \frac{\vec{q} - (\vec{q} \cdot \hat{S})\hat{S}}{\|\vec{q} - (\vec{q} \cdot \hat{S})\hat{S}\|}. \tag{3.13}$$

Finally, we can calculate the wing roll angle (η) from

$$\eta = \tan^{-1}\Big(\frac{\hat{C} \cdot \hat{\theta}}{\hat{C} \cdot \hat{\phi}}\Big) sign((\hat{C} \cdot \hat{\phi})(\hat{C} \cdot \hat{\theta})), \tag{3.14}$$

where

$$\hat{\phi} = < -\sin\phi, \cos\phi, 0 > \tag{3.15}$$

and

$$\hat{\theta} = < -\cos\phi \sin\theta, -\sin\phi \sin\theta, \cos\theta > . \tag{3.16}$$

Effectively, this defines η as the angle $\hat{C}$ makes between the $\hat{\phi}$ and the $\hat{\theta}$ axes.

3.8 Results

Figures 3.8 - 3.10 show the results of applying HRMT to a typical flight sequence obtained from our apparatus. This film, where the fruit fly in question ascends

at a relatively slow rate of 3 cm/s, contains a little more than 34 wing beats of data. At a rate of about one frame per 2 seconds, it takes HRMT about 40 minutes to complete the entire sequence (on a 2.4 GHz Intel Core 2 Duo processor running Mac OS 10.5). At this point, it is worth noting that although the results section here will focus on this representative sequence alone for the sake of expositional clarity, HRMT is capable of providing accurate tracking of insect kinematics for a wide array of fruit fly movements, as will be shown in Chapter 4.

The left and right wing angular kinematics for the aforementioned flight sequence are shown in Figure 3.9. Part (a) displays values of ϕ, θ, and η for the whole sequence, whereas part (b) zooms-in on one wing stroke. Error bars are obtained via a model-shadow reconstruction method. Using this technique (fully described in [23]), we find that the error bars are approximately 2^o for ϕ and 3^o for θ and η. As seen in previous studies [25, 62], we find the fruit fly is employing a roughly sinusoidal oscillation in the azimuthal plane (ϕ). Since the curve for $\theta(t)$ is at twice the frequency as the azimuthal oscillations, we find that the fruit fly is using a figure-8 wing stroke. Finally, we observe that the wing rotation angle something akin to a smoothed square wave (i.e. Equation 2.12) with mid-strokes of roughly constant angle followed by a relatively rapid rotation about the wing's leading edge during stroke reversal.

Lastly, Figure 3.10 exhibits the translational (part (a)) and rotational (part (b)) dynamics of the insect body. In this particular movie, the insect is ascending and traversing in the $-x$ direction (relatively slowly) while making a slight dodge in the y direction. In all of the plots (although more apparent in the angular position curves), there exist oscillations that are superimposed upon the actual trajectory. These are artifacts of the tracking process, resulting from the

cyclical nature of occlusions caused by the wings on the body. For example, when the wings are in front of the body, a beer-gut-like growth is added to the front of the body, as the forward pitch of the body conspires with the wings to cause a protrusion on the visual hull. A similar result occurs at the rear of the insect when the wings are near their maximal posterior position. Since the clustering algorithm clusters these points onto the body, this occlusional cycle causes the observed oscillations in the body orientations. Fortunately, though, these artificial oscillations do not pose a great difficulty, as they are relatively small and the body velocity scale is about an order of magnitude beneath the wing velocity scale. Hence, we can obtain sufficiently accurate body kinematics by low-pass filtering the body measurements from HRMT.

That being said, however, we still can apply the model-shadow reconstruction previously to which we previously alluded to find error bars on the data arising from each individual frame. The body translational coordinates (x, y, and z) are known within 2 pixels (.05 to .1 mm, depending on the cameras' zoom). The yaw (ψ) and pitch (β) are known within 5^o. The roll (ρ), however, is only known within about 10^o. This is due to the cigar-like shape of the fruit fly body mentioned in Section 3.6.

3.9 Conclusions

In this chapter, we have shown Hull Reconstruction Motion Tracking (HRMT) to be a fast, robust, and accurate method for tracking fruit flies in free flight. This is accomplished by taking images from three orthogonally placed cameras, aligning and registering them, finding the resulting visual hull, and using k-means clustering and principal components analysis to extract the positions

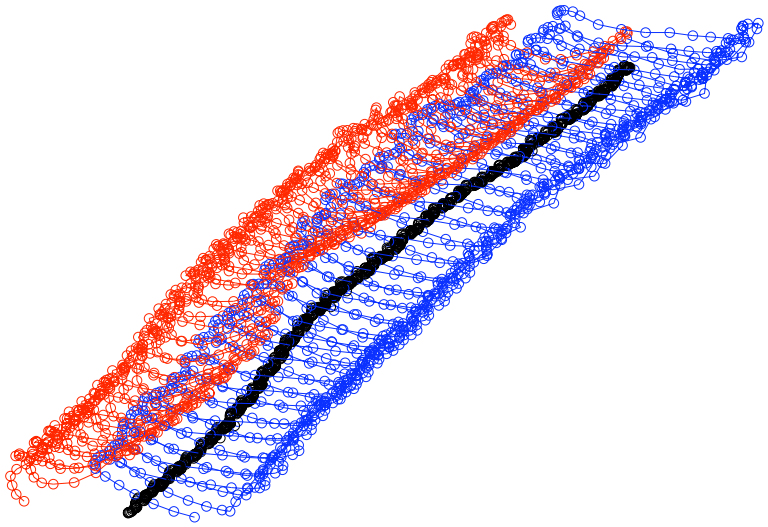

Figure 3.8: Example trajectory obtained from our experimental set-up and data tracker. Here, the black dots are the body positions, red dots are the positions of the right wing centroid, and blue dots are the positions of the left wing centroid. Each dot represents data from one frame, taken at 8,000 Hz. Error bars are approximately the size of the dots.

and orientations of the body and each of the two wings. The capacity to do this will be taken advantage in Chapter 4, as well as in [23], [75], and [76], to tackle problems like the control of sideways flight, ascending flight and turning maneuvers, the nature of wing rotation, and how insects respond to external perturbations.

This, of course, does not mean to imply that future improvements to HRMT are not possible or desirable. The most obvious area in which progress is possible in the tracking of the body's roll angle. One quick-fix which results in a less noisy estimation for this angle is to average the left and right wing values of the vertical deviation, θ. This, however, is somewhat unsatisfactory, as one is implicitly assuming that the two wings have identical mean θ values with respect to the frame co-rotating with the body. One way of ameliorating this concern is to find a way to use a marker-based technique to track the roll. Since (as seen in Figure 3.4) we do have some weak intensity information, such as the

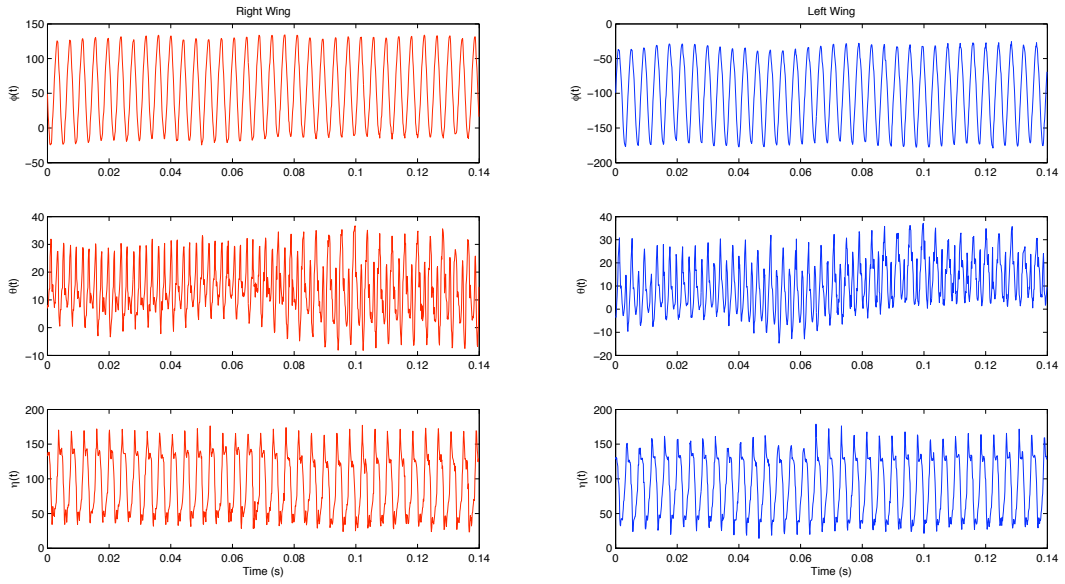

(a)

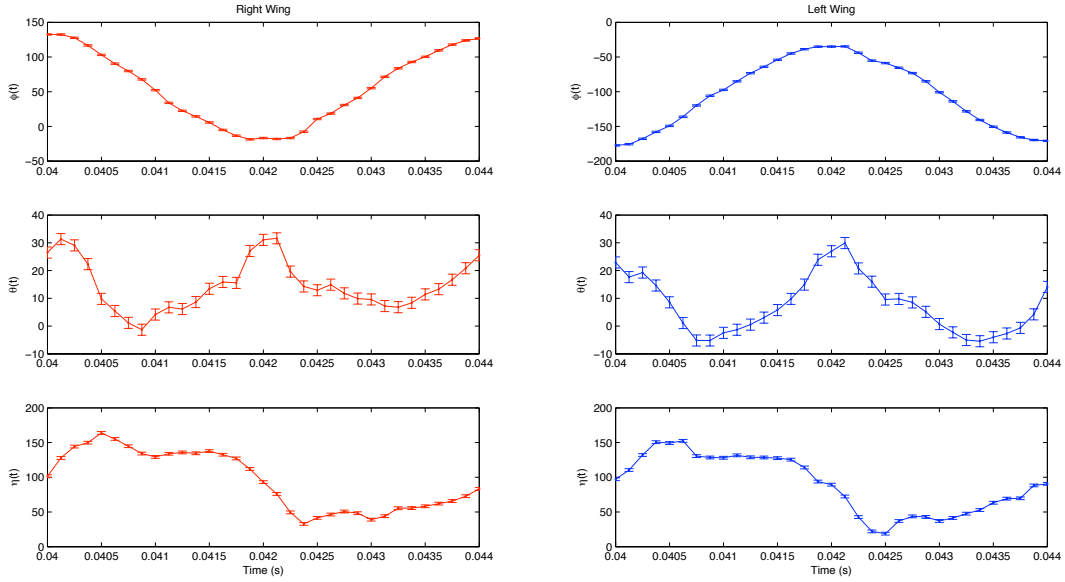

(b)

Figure 3.9: Sample data sequence from HRMT. The data shown are three Euler angles from each wing from a slowly-ascending ($\approx$ 3 cm/s) fruit fly which is captured for 34 wing beats. Part (a) shows data for the entire sequence and part (b) is a zoom-in on a single wing beat.

relative transparency of the wings, this could be possible. Also, since the observed values for the wing orientation angles depend on the body roll, a hybrid Bayesian approach taking advantage of these conditional probabilities might be

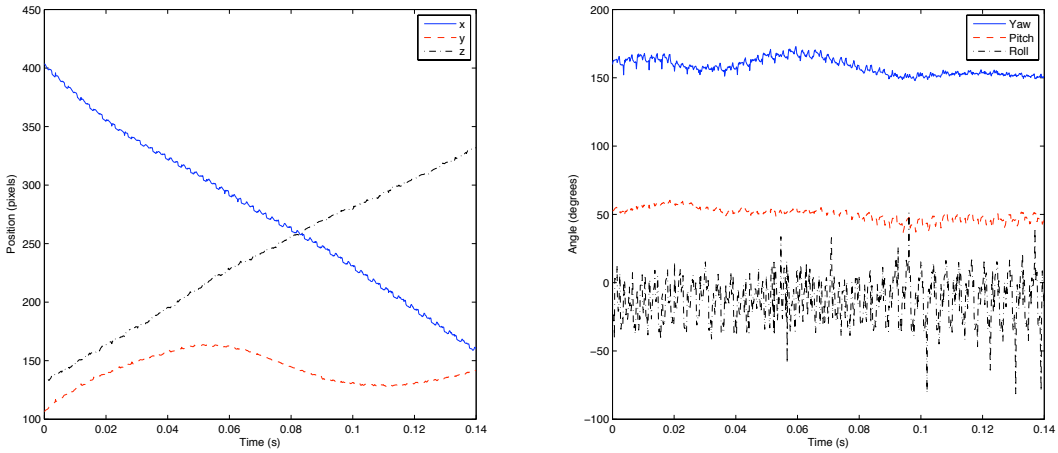

Figure 3.10: Sample body data sequence from HRMT.

of utility [82, 83].

Another aspect of HRMT which could be extended is the ability to track wing deformations. Since our test species for the method is the fruit fly, which has relatively stiff wings, our assumption of the wings as rigid bodies is fairly good (camber deformations are usually no greater than 15%, which occurs during wing rotation). For larger insect such as hawkmoths, though, this assumption breaks down, hence neglecting important aspects of the insects' flight dynamics [87, 88]. By utilizing a photogrammetric method similar to that used in [80], however, these deformations might be understood.

These possible augmentations aside, HRMT provides an improved method for tracking insects in free flight with high throughput and temporal-spatial resolution which can be applied to aid the understanding of many unresolved questions in insect flight.

CHAPTER 4

THE DYNAMICS AND CONTROL OF FRUIT FLY ASCENDING FLIGHT

4.1 Introduction

Having described a method for capturing and tracking fruit flies in the previous chapter, we now aim to utilize this data to explore a particular type of behavior often observed – ascending flight. The climbing flight of a fruit fly is an interesting case because it is not only commonly seen experimentally, but because it is also in some senses a limiting case in which flight performance is pushed to the limit as the animal must support more than its own body weight.

Several previous studies have looked at the problem of ascending flight without actual ascent to investigate the maximal force production of flying animals. Specifically, [89–91] observe the kinematics and force production of four species of tethered fruit flies (*Drosophila*). Here, the fly was tethered amidst an LED arena displaying visual stimuli. A pattern was played on the LED array, invoking increases and decreases in force production. A principle finding in these studies found was that a combination of somewhat unbendable morphological and metabolic constraints put a limit on the maximum force produced.

The morphological side of this barrier is that flapping stroke amplitudes can be no larger than 90^o before the animal's wings run into each other. Since the stroke amplitude is positively correlated with force production in fruit flies [89], this limitation provides the aforementioned morphological threshold. This same feature was also found as a limiting factor in orchid bee and hummingbird force production in variable density gasses [92, 93].

In addition to this morphological constraint, however, [89] and [90] also found that there is a metabolic limit to force production. The fruit flies in their

study would alter both flapping frequency and stroke amplitude to increase force production, but even at sub-maximal observation of stroke amplitude, the insect never went above a threshold of power usage. This finding was later confirmed by [22], which found that even flies selectively bred for maximal flight performance maxed-out at about 28 W (kg muscle)$^{-1}$ of power output. Additionally, by measuring the flies' CO_2 output during the experiment, an estimate of muscle efficiency was obtained. It was found that, oddly enough, as flight forces increased, muscle efficiency (estimated mechanical power from wing strokes divided by estimated power from CO_2 output) increased as well.

What these studies do not address, however, is the coupling between an insect's body dynamics and its force production (tethering, after all, has a tendency to have an adverse effect on movement). The motion of the body upwards affects not only the local wind velocity near the wing, but also causes a change in the wing angle of attack and creates an effect where aerodynamic drag on each wing acts in the vertical direction. The effect of this coupling has yet to be investigated explicitly. Additionally, as the tethered insects are induced to increase/decrease force production by maintaining a constant position with respect to their visual field, it is unclear whether observed kinematic changes would occur if the fly's imperative is to actually move upwards, rather than to remain constant with respect to its surroundings.

Also intriguing is how the ascent velocity is attained and controlled. [22] noticed that the ascending fruit flies in their apparatus achieved a steady-state velocity relatively rapidly (on the order of 20-30 wing beats). Is this a purely dynamical phenomenon, or does the insect directly control this ascent? Also, if an insect alters its ascent velocity from a previous steady-state, what kind of control does it exhibit? In [94], a computational model of a fruit fly was imbued

with a PID altitude controller which could modulate only its flapping frequency to alter its state (increase f to increase vertical acceleration). This cannot be the whole picture for an insect, however, as [89] found that the flapping frequency actually decreases at near-maximal force production and the force production appears to be determined via an increased stroke amplitude.

In this chapter, we present our initial investigations as to how fruit flies (*Drosophila melanogaster*) attain and control their ascent speed. In particular, we ask which degrees of freedom are actuated as the flies achieve varying steady-state ascent speeds and model this process through a simplified model of intermediate Reynolds number flapping flight. We find that ascent velocity is controlled primarily by increasing the wing velocity scale while keeping a roughly constant angle of attack. This is consistent with our model, as it predicts both the form of this dependence and that velocity modulation is more energy efficient than angle of attack modulation. In addition, we observe how fruit flies transition from one ascent speed to another.

4.2 Description of the Model

We will first describe the set-up and the assumptions of the simple model of ascending flight we use to analyze and gain intuition about the system at hand. The basic idea behind our formalism is that we assume a fruit fly's flight forces are the same as those experienced by a translating airfoil at intermediate Reynolds number ($Re \approx 100$). This assumption ignores the effects of wing rotation, stroke plane deviation, and changing velocities during the stroke, but aims to serve as a first (or zeroth) order approximation for the dynamics with which an insect must contend. These assumptions are plausible for the case of fruit flies, as their body dynamics are much slower than their wing dynamics, so this

model can be viewed akin to finding the average vertical force production over the course of a wing beat. This coarse-graining allows for a more analytically tractable model that can still provide quantitative predictions. In addition, we do not need to fret about left-right wing asymmetries, as any difference in lift production would cause the insect to roll.

To be more precise, we assume that an insect is free to move its body only in the vertical direction (horizontal wing velocity modulation can only be achieved through modulating the wing stroke itself) and has two control degrees of freedom to modulate. First, the insect, of mass m, can alter the velocity scale, U, of its wings. In reality, this can be done by changing either the flapping frequency or amplitude of the strokes. Also, we assume that the insect can control the angle of the airfoil with respect to the horizontal, α. As a result of these control parameters and the according fluid forces acting on the wing (to be described momentarily), a vertical velocity, v, can be induced (although not directly actuated). This changes the resulting velocity and angle of attack of the wing to be U' and α', respectively. Hence, $U' = \sqrt{U^2 + v^2}$, and $\alpha' = \alpha - tan^{-1}(\frac{v}{U}) \equiv \beta$. A schematic of this can be seen in Figure 4.1. The fluid force model on the wing is assumed to be quasi-static, implying that there is no history-dependence when calculating forces. Forms for the magnitude of lift, L, (force perpendicular to U') and drag, D, (force antiparallel to U') are given by the standard forms:

$$L = \frac{1}{2}\rho_f C_L \bar{c} R U'^2 \sin 2\alpha' \tag{4.1}$$

and

$$D = \frac{1}{2}\rho_f C_D \bar{c} R U'^2 \sin^2 \alpha'. \tag{4.2}$$

Here, ρ_f is the density of air, $\bar{c}$ is the mean wing chord length, R is the wing radius, and C_L and C_D are lift and drag coefficients, respectively. Additionally, we assume there is a term due to aerodynamic drag on the body in the vertical

direction, D^{Body} (horizontal body drag is neglected, as the insect is assumed to be ascending straight up). This term is given by

$$D^{Body} = \frac{1}{2}\rho_f C_D^{Body} \bar{c} R v|v|, \tag{4.3}$$

where C_D^{Body} is the body drag coefficient[1]. Putting these terms together, the equation of motion in the vertical direction is given by

$$m\dot{v} = L\cos\beta - D\sin\beta - mg - D^{Body}. \tag{4.4}$$

This can be simplified via trigonometric identities, and then non-dimensionalized using length scale, $\bar{c}$, and velocity scale, $\sqrt{\bar{c}g}$. The resulting equation involving the non-dimensionalized velocities (in remarkably abusive notation, still referred to as U and v) is as follows:

$$\dot{v} = \frac{U\sin\alpha - v\cos\alpha}{2\lambda\sqrt{U^2+v^2}}\Big((2C_L U^2 + C_D v^2)\cos\alpha + (2C_L - C_D)Uv\sin\alpha\Big) - 1 - \frac{C_D^{Body} v|v|}{2\lambda}, \tag{4.5}$$

where $\lambda \equiv \frac{m}{\rho_f \bar{c}^2 R}$, is the non-dimensionalized mass. For typical fruit fly morphologies, λ is about 350.

Lastly for this section, some of our analyses will necessitate calculation of power output needed to drive the wing velocity. Since all of the applied force provided here is horizontal in the wing frame ($\hat{U}'$ direction in the lab frame). The power, P, can be calculated by

$$\begin{aligned} P &= -\vec{U}' \cdot \vec{F}^{aero} && (4.6)\\ &= \sqrt{U^2+v^2}(D + D^{Body}\sin\beta) && (4.7)\\ &= \frac{\bar{c}R\rho_f}{2}(C_D\sqrt{U^2+v^2}(v\cos\alpha - U\sin\alpha)^2 + C_D^{Body}|v^3|). && (4.8) \end{aligned}$$

[1]It should be noted that the effective surface area of the body is likely different from the effective surface area of the wings, $\bar{c}R$, this factor should be constant across insects, so we will simply wrap it into C_D^{Body}.

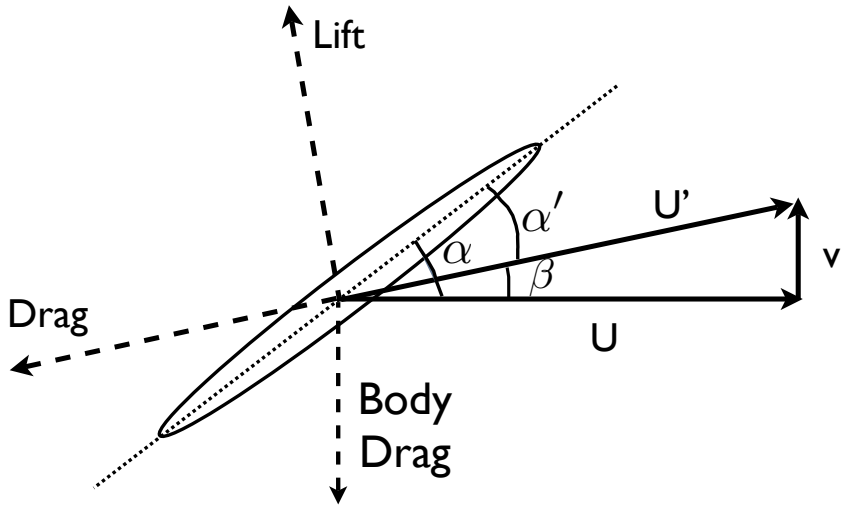

Figure 4.1: Schematic of the ascending model

Non-dimensionalizing the previous equation with power scale, $\bar{P}$, given by $\bar{P} \equiv \rho_f \bar{c}^{5/2} R g^{3/2}$, we have that

$$P = \frac{1}{2}(C_D \sqrt{U^2 + v^2}(v \cos\alpha - U \sin\alpha)^2 + C_D^{Body}|v^3|), \tag{4.9}$$

again, using the abusive notation where U, v, and P represent the non-dimensional values of their corresponding quantities. From this point on, however, we shall only deal with the non-dimensional equations, hopefully limiting confusion as much as possible.

4.3 Model Analysis

4.3.1 Location and Stability of Fixed Points

As is the first step of most dynamics studies, we shall begin our analysis by a) looking for the system's fixed points and their corresponding stabilities, and b) simply simulating it for typical parameters vales. Figure 4.2 shows some typ-

ical results from the latter of the two endeavors. Here, we observe that there appears to be one stable fixed point to which all solutions flow, thereby implying the lack of any unstable fixed points. Figures 4.3-4.4 show the dependence of the steady-state ascent velocity, v^*, on both U and α, implying that a stable steady-state velocity exists over a wide swath of kinematic parameter range. Additionally, the qualitative structure of the U and α dependence is quite structurally robust to changes in the morphological parameters (C_L, C_D, C_D^{Body}, and λ). There is, however, only one region of parameter space where this alters, which we will discuss shortly in Section 4.3.2, but it exists in the biologically unobserved region where α becomes very large.

Given the intuition we've gained from simulation, we shall attempt to analytically determine the fixed points for our system. Ignoring the absolute value sign in (4.5), thereby looking at only cases in which $v \geq 0$ or $v \leq 0$, depending on the sign in front of the body drag term, setting $\dot{v} = 0$ results in in a 6th order polynomial equation in v. This makes life a little difficult, seeing as how we cannot guarantee an analytic solution to the equation. To alleviate this, we Taylor expand (4.5) about $v = 0^+$, resulting in the third-order expression displayed below:

$$\begin{aligned}\dot{v} \approx \frac{1}{2\lambda}C_L U^2 \sin 2\alpha - 1 - \frac{1}{4\lambda}(C_D + (4C_L - C_D)\cos 2\alpha)Uv \\ -\frac{1}{2\lambda}(C_D^{Body} + (3C_L - 2C_D)\cos\alpha \sin\alpha)v^2 \\ -\frac{1}{8U\lambda}(C_D + (3C_D - 4C_L)\cos 2\alpha)v^3 + O(v^4). \end{aligned} \tag{4.10}$$

We shall only analyze the case where $v \geq 0$ here, as that is the regime which our experiment probes. We can then set this equation equal to zero and solve for v, yielding an analytic approximation. Granted, the form of this solution is still too unwieldy to display here, but with the aid of Mathematica [95], the solution can be obtained. Similarly, we can also find the predicted equilibrium values

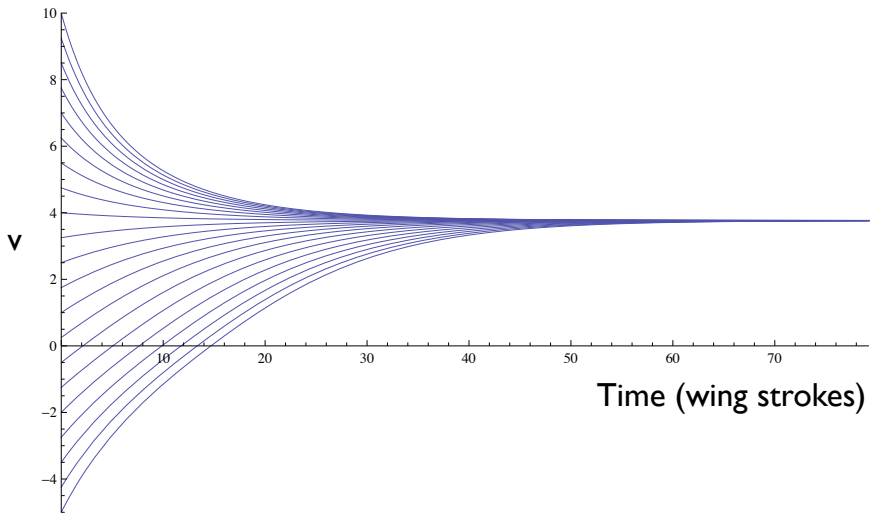

Figure 4.2: Simulation results for ascending velocity, v, vs. time in wing strokes (one wing stroke = 1/250 s) with $C_D = 3$, $C_L = 2$, $C_D^{Body} = 3$, $\alpha = 60^o$, $U = 21$, and $\lambda = 350$. Each line represents a simulation of (4.5) starting from a different initial condition.

using only the linear and/or quadratic terms as well.

Figure 4.5 displays simulation results for the v^* vs. U curves, and Figure 4.6 displays plots of these curves resulting from both the aforementioned approximations as well as direct numerical simulation of the (4.5). From these two figures, we see that although the linear approximation diverges quickly from the simulation results as U increases, the quadratic and cubic curves approximate the simulation curve quite well, especially in the range of steady-state velocities observed in real insects (roughly $U \in [15, 21]$). This analytic curve will prove useful later in fitting the model to experimental results.

4.3.2 Analysis of the Hovering Case

One situation in which the model can be solved exactly is for the hovering case, where the lift produced is equal to the body weight. First, we will solve for the

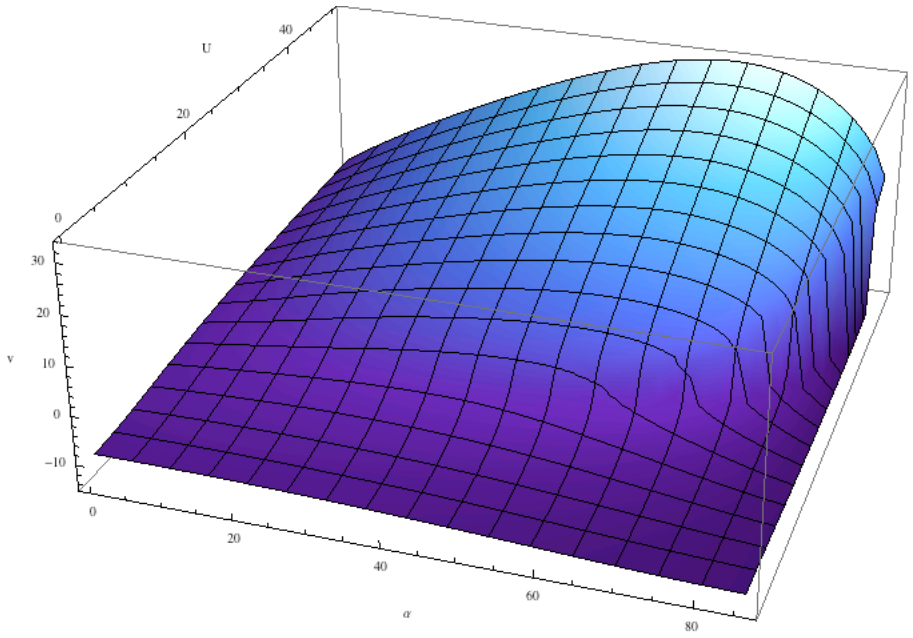

Figure 4.3: Plot of steady-state ascent velocity (v^*) vs. U and α from simulations with $C_D = 3$, $C_L = 2$, $C_D^{Body} = 3$, and $\lambda = 350$.

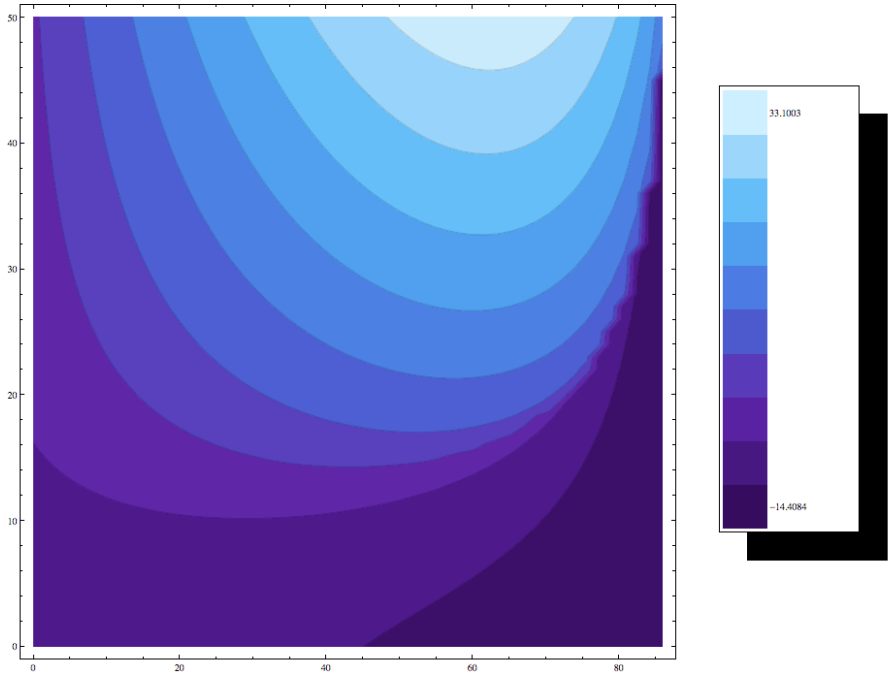

Figure 4.4: Contour plot of steady-state ascent velocity (v^*) vs. U and α from simulations with $C_D = 3$, $C_L = 2$, $C_D^{Body} = 3$, and $\lambda = 350$.

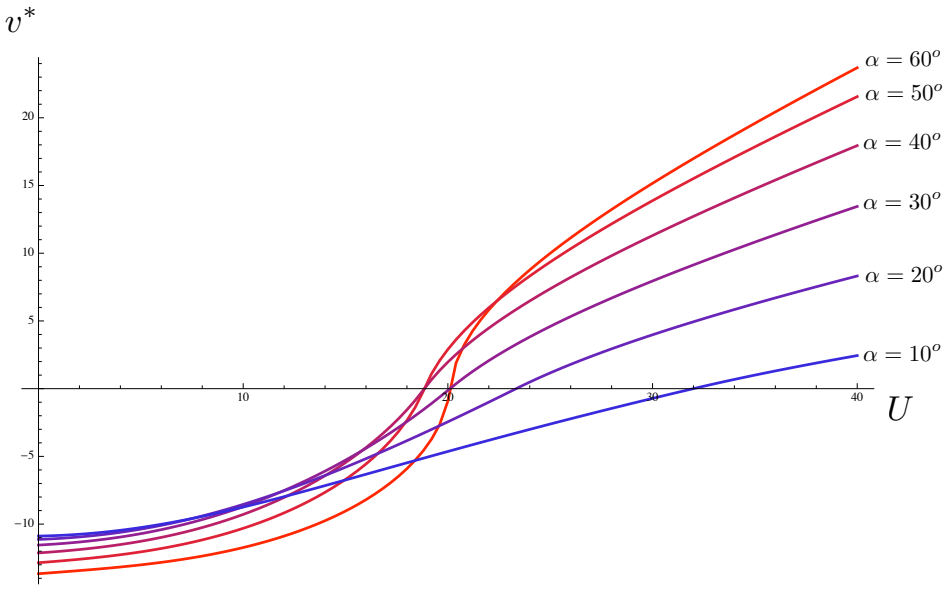

Figure 4.5: Plot of steady-state ascent velocity (v^*) vs. U from simulations with $C_D = 3$, $C_L = 2$, $C_D^{Body} = 3$, $\lambda = 350$, and varying values of α.

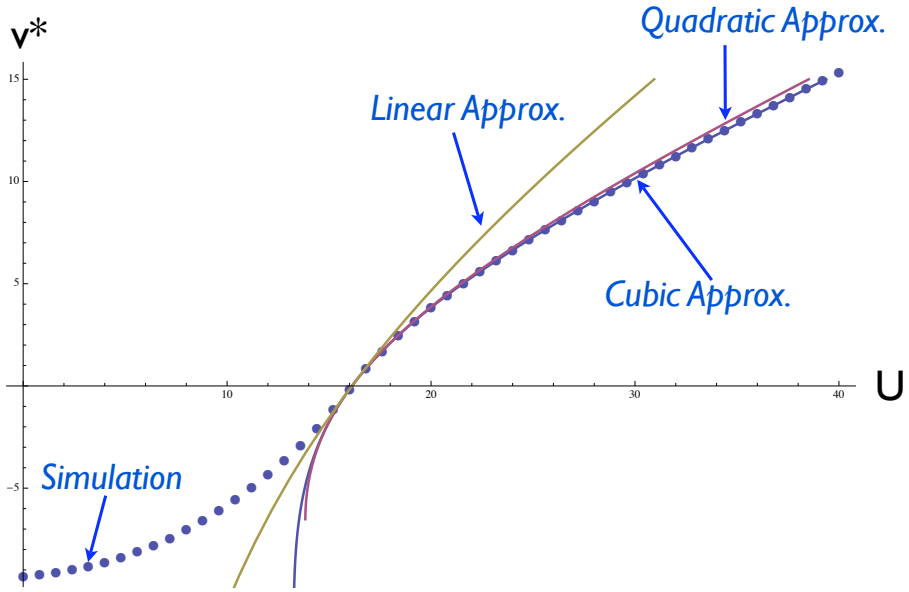

Figure 4.6: Simulation and approximation results for steady-state ascending velocity (v^*) vs. horizontal velocity (U). Here, $C_D = 3$, $C_L = 2$, $C_D^{Body} = 3$, $\alpha = 30^o$, and $\lambda = 350$

curve in the $U-\alpha$ plane which should result in $v = 0$. This manifold is interesting because it will serve as a line of hovering fixed points, about which we will later perturb. Setting $\dot{v} = 0$ in our equation for $\dot{v}$ and solving for U, we get that

$$U^*(\alpha) = \sqrt{\frac{2\lambda}{C_L \sin 2\alpha}}. \tag{4.11}$$

Hence, $U^*(\alpha)$ is the velocity at which the wing must be driven in order to maintain hovering flight assuming a fixed α and no instabilities in the v direction.

Expanding our original differential equation linearly about $v = 0$, and substituting $U^*(\alpha)$ for U, we get that

$$\dot{v} \approx -\frac{1}{2\lambda}(2C_L \cos 2\alpha + C_D \sin^2 \alpha)U^* v. \tag{4.12}$$

Since this differential equation is stable if the prefactor in front of the v term on the right hand side is negative (and assuming that $0 \leq \alpha \leq \pi/2$), this implies that the hovering solution is stable if

$$2C_L \cos 2\alpha + C_D \sin^2 \alpha > 0. \tag{4.13}$$

The first piece of information this equation gives us is that a stable hovering state must exist for all α between 0 and $\pi/4$. For $\alpha > \pi/4$, stability becomes a competition between a lift component that destabilizes and a drag component that stabilizes. Also, as the left hand side of the equation monotonically decreases on $\alpha \in [\pi/4, \pi/2]$, subbing $\alpha = \pi/2$ yields that no instability can exist if $C_D > 2C_L$. Furthermore, assuming that $4C_L - C_D > 0$ (a safe assumption for all realistic parameter values), as well as performing a few trig identities, (4.13) reduces to

$$\sin^2 \alpha < \frac{2C_L}{4C_L - C_D}, \tag{4.14}$$

or

$$\alpha < \sin^{-1}\Big(\sqrt{\frac{2C_L}{4C_L - C_D}}\Big) \equiv \alpha^*. \tag{4.15}$$

This implies that for any value of α larger than α^*, no stable hovering solutions are possible. As seen in Figure 4.7, for $\alpha > \alpha*$, the steady-state ascending velocity at $v = 0$ is unstable, resulting in either a stable ascending or descending state, depending whether the initial ascent velocity is greater or less than zero. It should be noted that this transition point is independent of the insect mass, depending only on the lift and drag coefficients. As shown in Figure 4.8, (4.15) predicts the simulation value of the transition point exactly. An example of trajectory dynamics in the unstable regime is displayed in Figure 4.9.

Lastly, although this bifurcation is perhaps interesting from a mathematical perspective, it doesn't appear to be a large factor in ascending insect flight, as observed angle of attack values are much lower than $\approx 60^o - 70^o$, which is where this transition occurs for typical insect parameter values. In addition, in order to achieve high ascent velocities through this effect alone, (4.11) shows that correspondingly large values of U must be used, resulting in a large increase in power input (Figure 4.10). α^* could serve as an upper bound for angle of attack, however, as values above this lead to an instability in the vertical velocity.

4.4 Experimental Methods

4.4.1 Experimental Apparatus

To compare the model described in the previous sections to observed wing and body motions, we utilize the experimental set-up initially described in Chapter 3 [23]. This apparatus consists of three orthogonally placed Phantom V7.1 cameras, each filming at 8,000 Hz with 512×512 pixels of resolution. This set-up captures three silhouettes of a freely-flying fruit fly, which we then track using

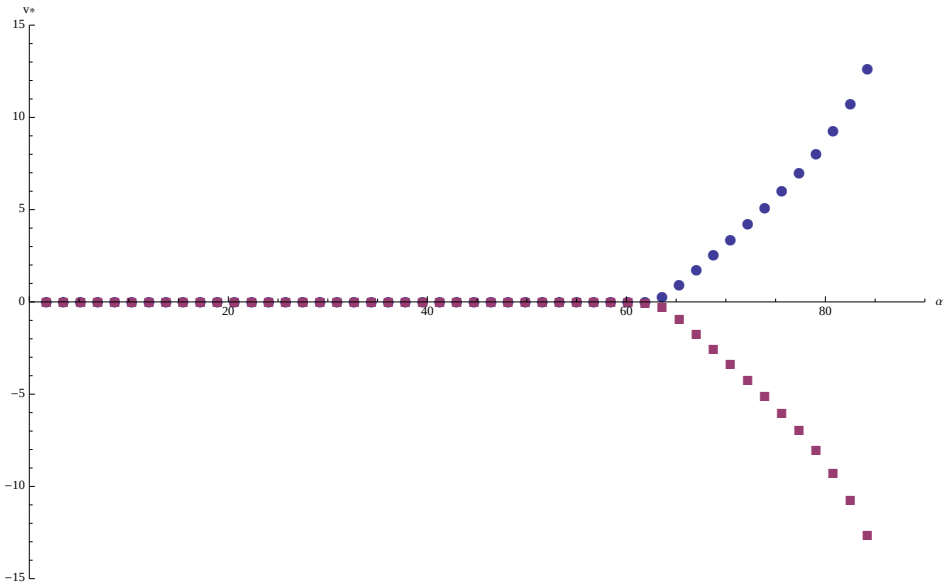

Figure 4.7: Bifurcation diagram of v^* vs. α with $U = \sqrt{\frac{2\lambda}{C_L \sin 2\alpha}}$ (the hovering velocity) for $C_L = 2$ and $C_D = C_D^{Body} = 3$. Circles represent solutions starting with $v > 0$ and the squares are solutions starting from $v < 0$. For this set of parameters, $\alpha^* \approx 63.4^o$.

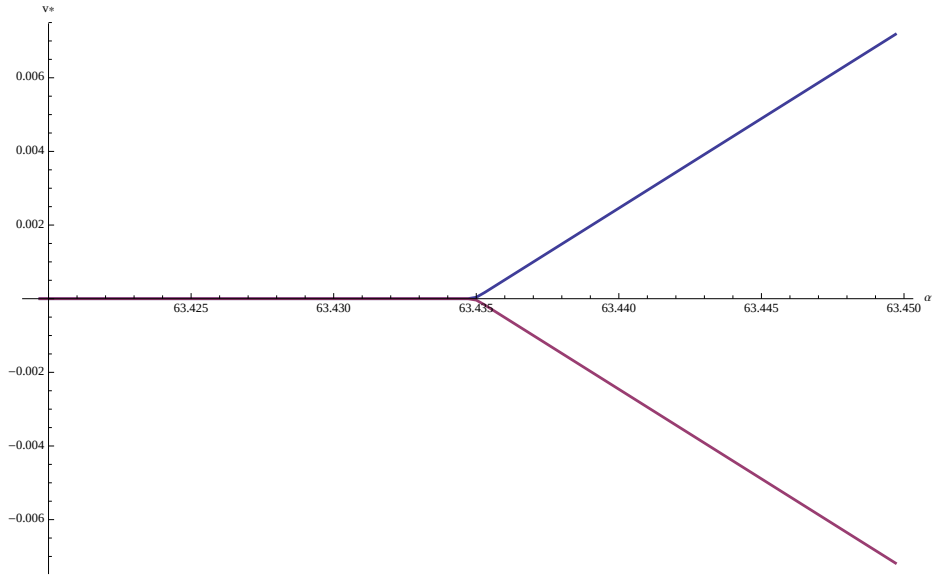

Figure 4.8: Zoom-in of Figure 4.7 near $\alpha \approx 63.435^o = \alpha^*$.

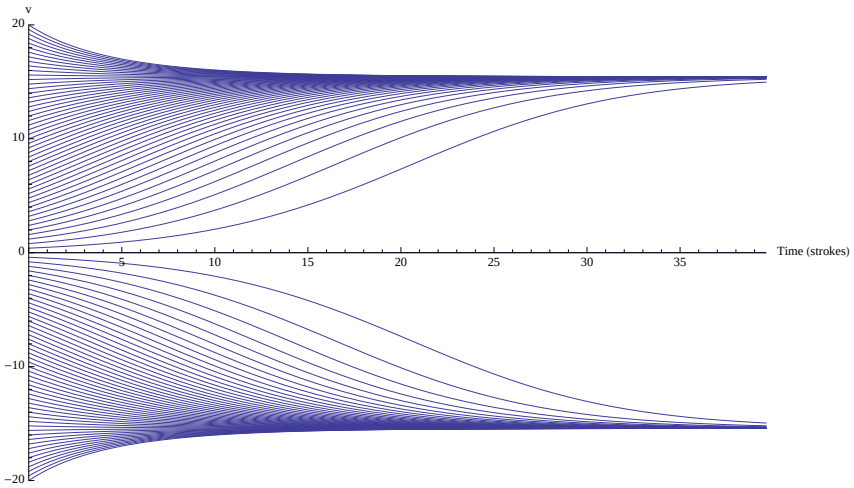

Figure 4.9: Sample trajectories of v vs. t for $\alpha > \alpha^*$.

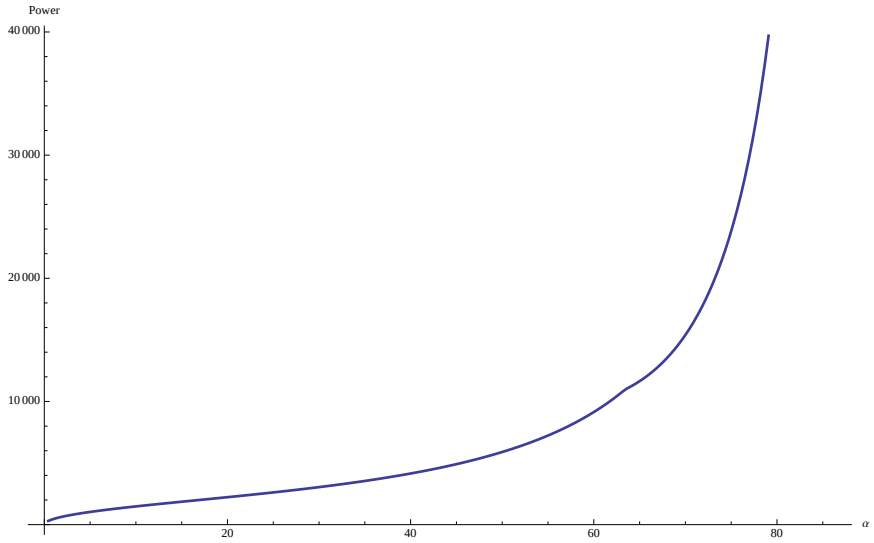

Figure 4.10: Plot of power (Equation 4.9) vs. α for the hovering case. Note the exponential rise in the the power required to maintain hovering flight with increasing α. The slight kink near 60^o is the location of the bifurcation

the Hull Reconstruction Motion Tracking (HRMT) method introduced in [23] and Chapter 3. The final output from this tracking algorithm are the 18 translational and rotational degrees of freedom of an insect (three translational and three rotational for each of the body, left wing, and right wing).

In addition to this facility, we utilize a custom-built apparatus which engenders ascending flight capture (Figure 4.11). In this, several fruit flies are placed at the bottom of a container which has a long, narrow opening, at the top of which is the camera filming volume. The sides of the opening are lined with chalk so that the flies are unable to simply walk up the edges. As the flies opt to leave the container, they must fly upwards, and we capture their flight just as they leave the opening. Empirically, we have found that the insects' usually fly straight upwards at a nearly-constant vertical velocity while within the filming region. From this apparatus, we have obtained several filming sequences in which the fly is moving vertically at speeds between 3 cm/s and 35 cm/s, an example of which can be seen in Figure 4.12. To ensure that the sequences used represent pure ascending movies, we make a cut that the left wing and right wing velocity scales (defined in a moment) must be with ±10% of each other. This eliminates movies in which the insect produces large amounts of torque or lateral forces.

Additionally, we are interested in not only the steady-state ascent dynamics of these insects, but also how this ascent is achieved and controlled. In hopes of understanding these questions more fully, we capture fruit flies with decelerating vertical velocities using another custom apparatus (again, Figure 4.11). Specifically, several flies are placed on the bottom of a cubic clear plastic enclosure made of microscope slides, again, with chalk lining on the outer walls to discourage the animals from simply walking up the sides. Instead of placing

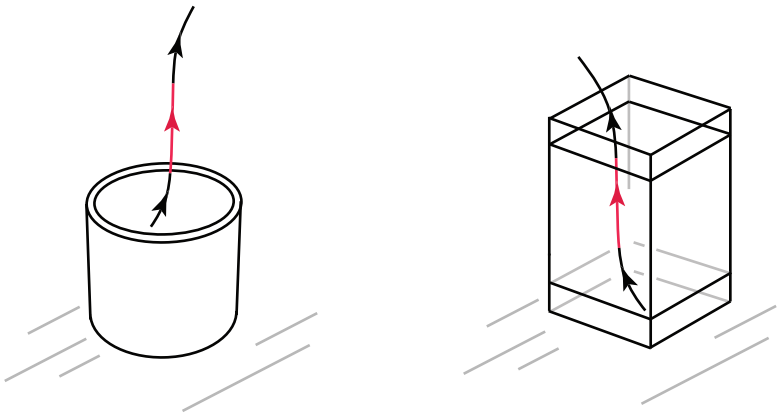

Figure 4.11: Schematics of the ascending flight apparatuses. For both figures, the black/red line represents the path of a fruit fly, with the filming region represented by the red segment. The left figure places the filming region atop a section of PVC tubing, through which the insects escape. This has a tendency of engendering steady-state ascending flight. The rightmost schematic shows a cube made out of microscope slides which is placed at the bottom of the filming enclosure seen in Figure 3.3. Most of the flight sequences obtained from this figure are of accelerating flight, as it captures fruit flies as they transit from take-off behavior to steady-state behavior.

the filming volume atop the enclosure here, though, the filming region is placed a few centimeters above the bottom, hence, filming the animals while they are changing velocities.

4.4.2 Deriving Comparison Metrics

Given the data collected above, we would like to be able to compare the observed velocities and angle of attack to the model parameters U and α. This is somewhat problematic, as in reality, U and α are (roughly) periodic functions of time. Hence, in order to make a comparison, we need to determine effective parameters U_{eff} and α_{eff}, which will be the coarse-grained wing velocity and angle of attack for a wing stroke.

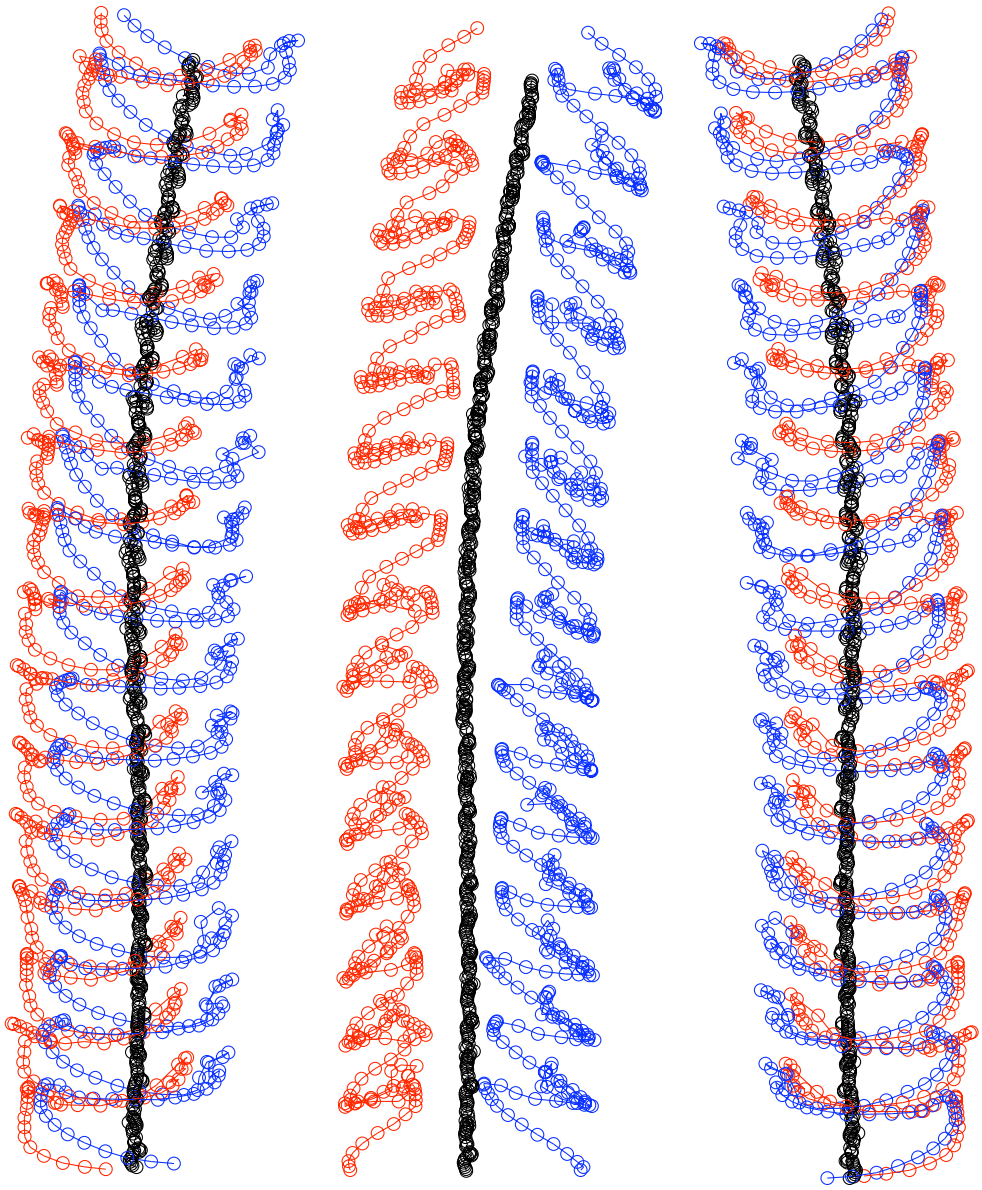

Figure 4.12: Three views of a typical steady-state ascending trajectory obtained from our experimental set-up and data tracker. Here, the black dots are the body positions, red dots are the positions of the right wing centroid, and blue dots are the positions of the left wing centroid. Each dot represents data from one frame, taken at 8,000 Hz. This particular insect is ascending with a velocity of about 24 cm/s.

The basic principle we use for this is that for a hovering insect, from quasi-steady theory, the average vertical force production, $\langle F_z \rangle$, is given by

$$\langle F_z \rangle = \langle \frac{1}{2} \rho_f \bar{c} R C_L U(t)^2 \sin 2\alpha(t) \rangle = \frac{1}{2} \rho_f \bar{c} R C_L \langle U(t)^2 \sin 2\alpha(t) \rangle = mg, \tag{4.16}$$

ignoring vertical force production from drag (i.e. an inclined stroke plane or wing stroke deviation from the stroke plane). Therefore, it makes sense to define our parameters such that

$$U_{eff}^2 \sin 2\alpha_{eff} = \langle U(t)^2 \sin 2\alpha(t) \rangle \tag{4.17}$$

in order for the relation

$$mg = \frac{1}{2} \rho_f \bar{c} R C_L \langle U(t)^2 \sin 2\alpha(t) \rangle \equiv \frac{1}{2} \rho_f \bar{c} R C_L U_{eff}^2 \sin 2\alpha_{eff} \tag{4.18}$$

to hold for the hovering case. Furthermore, as the lift is proportional to U^2, we will define $U_{eff} \equiv \sqrt{\langle U^2 \rangle} = U_{rms}$. Hence, in order to satisfy (4.17), we need

$$\alpha_{eff} \equiv \frac{1}{2} \sin^{-1} \frac{\langle U(t)^2 \sin 2\alpha(t) \rangle}{U_{rms}^2}. \tag{4.19}$$

Given these definitions, though, we still need to be able to calculate $U(t)$ and $\alpha(t)$ in order to make comparisons. We shall define $U(t)$ as the horizontal wing velocity at $\frac{2}{3}R$ (the approximate location of the wing's center of pressure), where R is the wing radius. More specifically, since our tracker gives the azimuthal angle, ϕ, as a function of time, and this angle is varies in a near-sinusoidal manner, we can define U_{rms} via

$$U_{rms} \equiv \frac{2}{3\sqrt{2}} R \phi_m 2\pi f, \tag{4.20}$$

where ϕ_m is the stroke amplitude and f is the stroke frequency (i.e. $\phi(t) = \phi_m \sin(2\pi f t)$). Finally, we non-dimensionalize all velocities using the velocity scale $\sqrt{\bar{c}g}$, as performed previously.

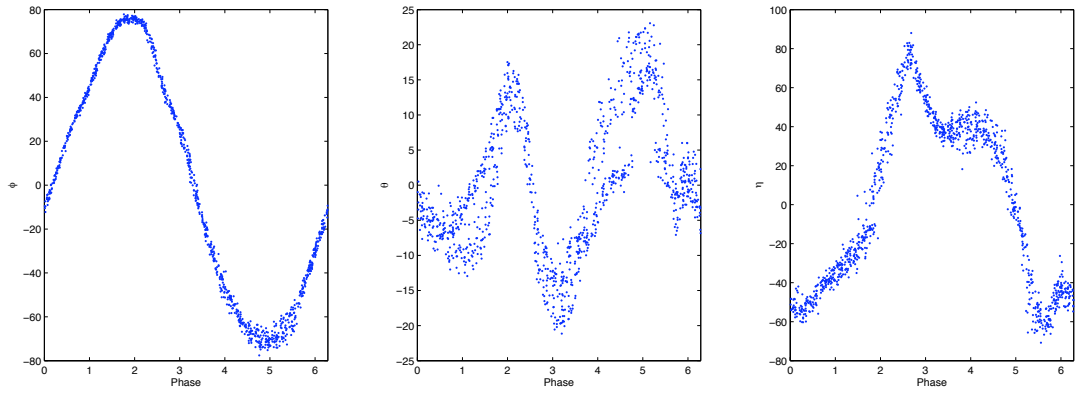

Figure 4.13: Sample output from the Phaser algorithm for three Euler angles vs. phase. Plots show right wing angular orientation data from a low-speed ascending sequence vs phase modulo 2π.

$\alpha(t)$, which is a geometric quantity, not to be confused with aerodynamic angle of attack, is defined as

$$\alpha(t) = \begin{cases} \eta(t) & \text{if } \dot{\phi}(t) \geq 0 \\ 90^o - \eta(t) & \text{if } \dot{\phi}(t) < 0 \end{cases}, \tag{4.21}$$

where η is the wing rotation angle as defined in Figure 3.7.

Finally, in order to split the data up into individual wing strokes, we use the Phaser phase reconstruction algorithm developed in [96]. This method takes a six-dimenensional data vector returned from the tracker (three Euler angles for each wing) and maps the observed time series onto a circle with phases, $\Phi \in [0, 2\pi)$. We define $\Phi = 0$ to be the maximum anterior position of the wings, and vivisect the data accordingly. From these values of $U(t)$ and $\alpha(t)$, we can then use (4.17) to find U_{eff} and α_{eff} for the strokes by averaging between the two wings. Additionally, as the body moves at a much slower speed than the wings, we simply assume that the vertical velocity, $\dot{z}$ is the total vertical distance traveled over one cycle, divided by period.

4.5 Steady-State Dynamics

Using the apparatus described in the previous section, we have six movies where flies ascend at a relatively constant speed with little to no wing asymmetries. These insects range in ascent speed between 3 and 35 cm/s. Applying the conversion metrics derived in Section 4.4.2, we obtain the plots seen in Figures 4.14 and 4.15. Figure 4.14 shows the relationship between ascent velocity and horizontal velocity scale, U. Here, we see the an almost linear relation, reminiscent of the small angle of attack curves of v vs U with constant α seen in Figure 4.5. Sure enough, Figure 4.15 shows that α varies little (effectively within error bars) between significantly different ascent sequences. In fact, if we fit the U vs v curve to the cubic model described in Section 4.3.1, we find that the fitted $\alpha = 31.4^o \pm 2.2^o$, well within the range of empirically observed angles (Figure 4.16).

These figures imply that in effect, insects control predominately their velocity scale, and not their angle of attack, to obtain varying ascending velocities. This still leaves open the question of the mechanisms behind this control. Figure 4.17 shows time-series plots of $\phi(t)$ with time normalized by the flapping frequency for both a fast and a slow ascending sequence. Here, we see that the more quickly ascending insect is using a significantly larger amplitude ($\approx 15^o$). Figure 4.18 displays values of v as a function of amplitude, showing that this trend holds (albeit somewhat noisily) across all six analyzed sequences, agreeing with the findings of [89, 90].

The other part of how an insect could control its horizontal velocity, its flapping frequency, alas, is a slightly less clear endeavor. In general, the observed positive change in stroke amplitude with increasing v is somewhat countered by a decrease in f (Figure 4.19). The relative increase in stroke amplitude, how-

ever, is more than the relative decrease in frequency, resulting in a net increase in U. The trend of decreasing f is more difficult to discern than the amplitude increase, however, as f is a function of insect mass, which, due to our experimental set-up, we are not able to measure for each specimen. Accordingly, we have two outlier flight sequences which have a lower than expected flapping frequency. For a single, tethered fruit fly, however, [89] also observed a decrease in f as the produced vertical force increased in the regime near maximal force production. This could imply that the ascent sequences we observe are near this point at which flight power is limited.

The general story here, though, appears to be that to achieve different steady-state ascent velocities, fruit flies increase their stroke amplitudes while maintaining a roughly constant angle of attack. Qualitatively, this is in line with the findings from [75], which found that the mean angle of attack over a whole wing beat is not controlled by the insect. Additionally, the upper limit on ascent velocities we observe ($\approx 40 cm/s$) is near the point at which the stroke amplitude is 90^o, implying that this might be an actual upper limit for maximal ascent velocity. A similar result has been observed for tethered fruit flies [89] as well as in hummingbirds flying in variable density gases [92]. The observed decrease in flapping frequency could be the result of the indirect driving mechanism of the fruit fly thorax saturating at maximal output levels. Additional increases in amplitude might occur from utilizing steering muscles in addition to the thoracic driving inputs, but these would not significantly affect the stroke frequency.

Finally, if we plot the power (calculated from (4.9) along the fitted v vs U curve (and also using morphological parameters from this fit), another interesting effect presents itself (Figure 4.20). Looking at the P vs v plot (Figure 4.20(b)), we see the reappearance of the infamous J-curve [97,98] with a minimum power

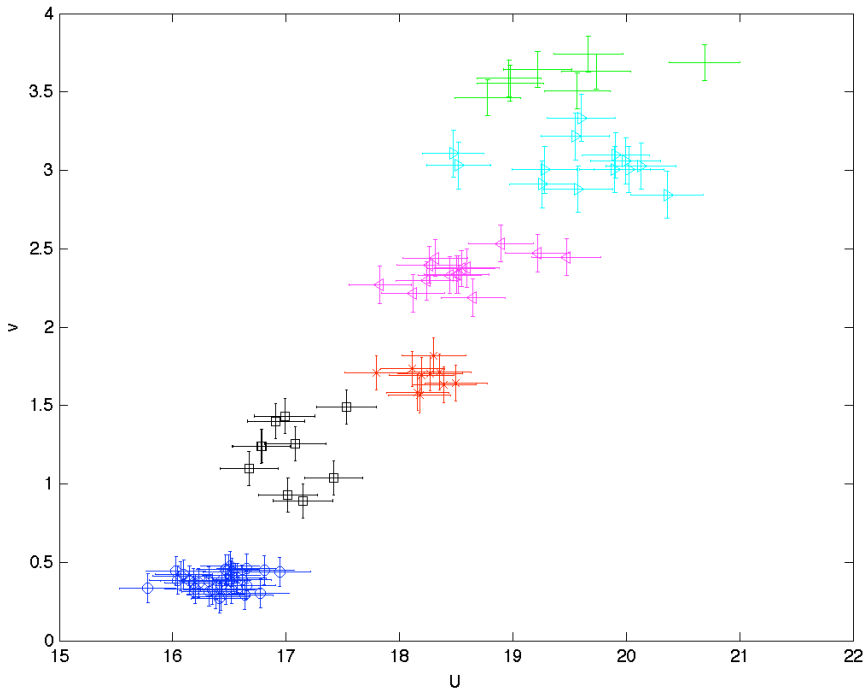

Figure 4.14: Plot of U vs v for several different ascending sequences. Each data point represents a single wingbeat, and different colors imply different sequences.

output at a non-zero flight speed, although this time it is referring to ascending, rather than forward flight. Here, P is minimized at a ascent speed of $v \approx 2$, which is well within our range of observed ascents ($v \approx 0 \rightarrow 4$).

The physical mechanism behind the appearance of this minimum in power arises from the fact that there is an interplay between the power required to overcome drag on the wings and the power required to overcome body drag. As seen in Figure 4.21, the wing power monotonically after decreases after a particular value of U. This is because the effective angle of attack, α', decreases as v increases, resulting in less drag. However, as the ascent velocity increases, the power required to overcome body drag increases like v^3. Summing these two components together results in a curve with a minimum ascent speed (Figure 4.21).

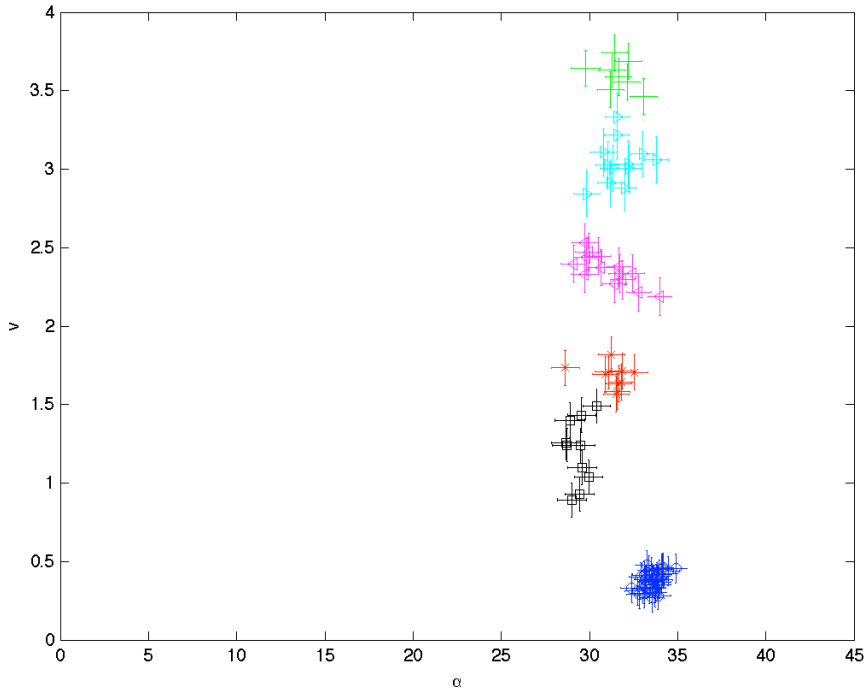

Figure 4.15: Plot of α vs v for several different ascending sequences (colors are the same as in Figure 4.14. Note that almost all variation observed is within measurement error bars.

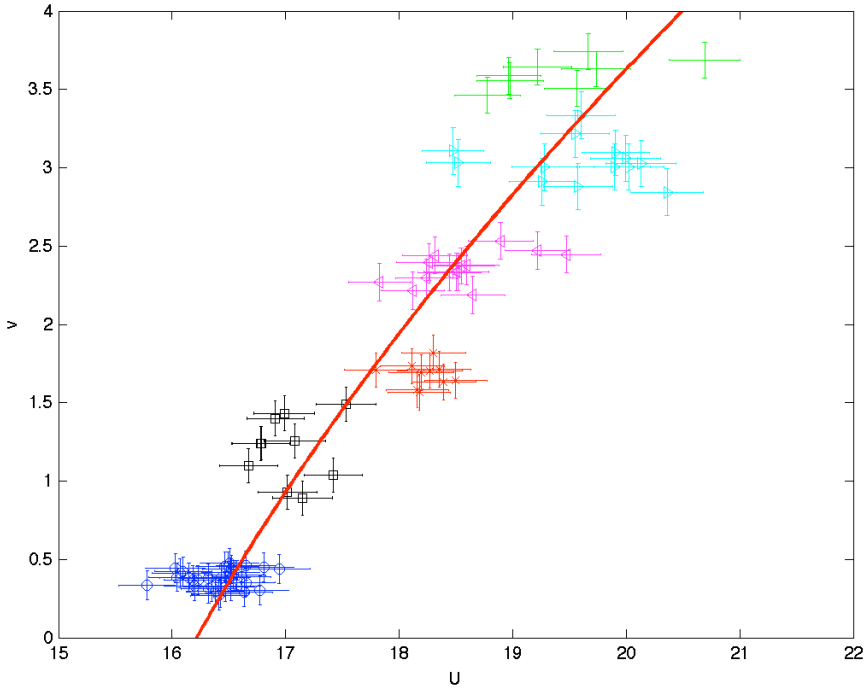

Figure 4.16: Ascent velocity vs U fit to cubic model (Equation 4.10). The fit parameters are $C_L = 3.0 \pm .25$, $C_D = 5.2 \pm 1.2$, $C_D^{Body} = 5.2 \pm 1.2$, and $\alpha = 31.4^o \pm 2.2^o$.

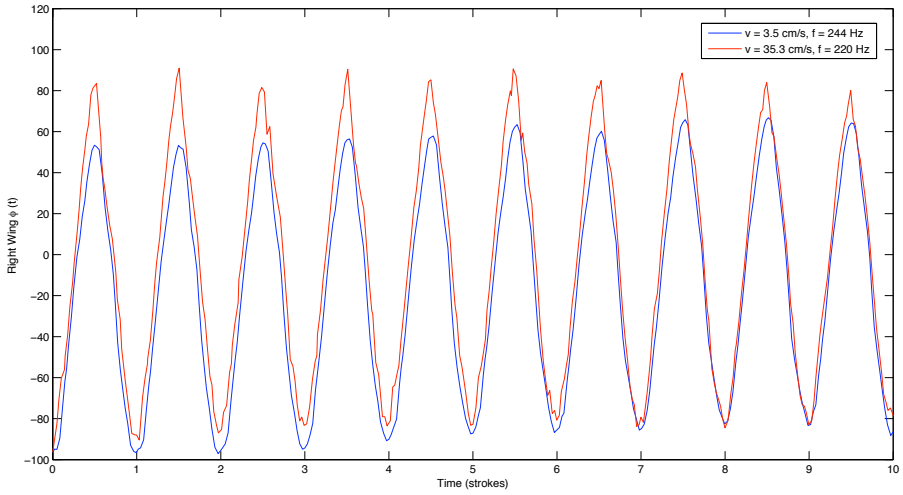

Figure 4.17: Right wing $\phi(t)$ vs t for two steady-state sequences of slow (blue) and fast (red) ascent velocities. The amplitude for the quickly ascending fly is noticeably larger.

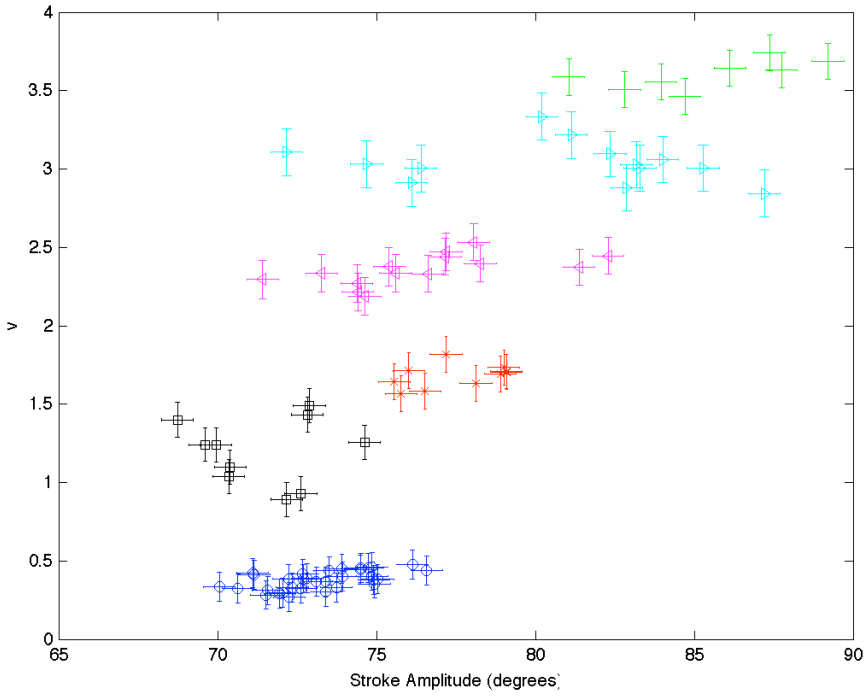

Figure 4.18: Ascent velocity vs stroke amplitude

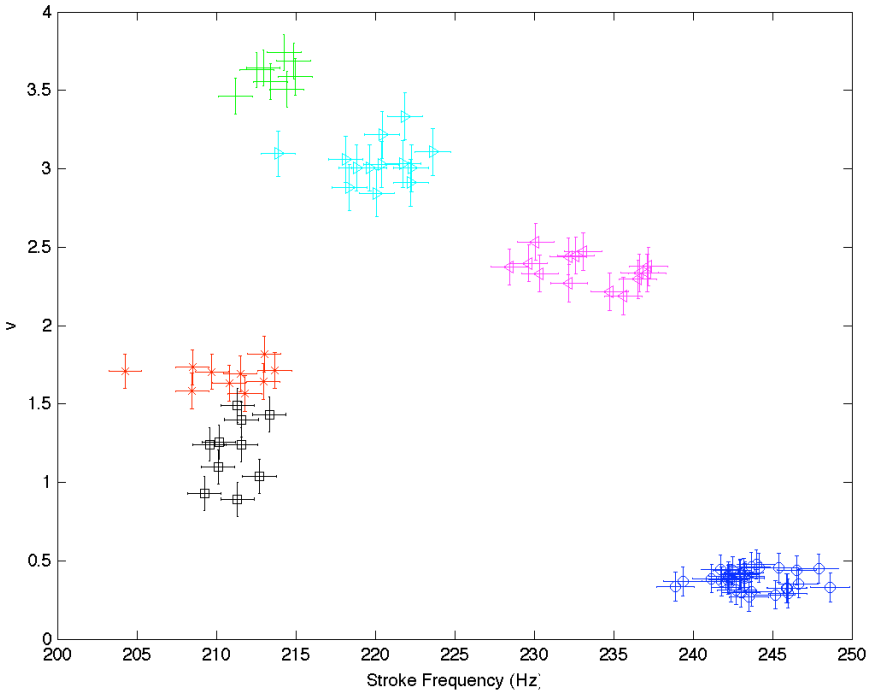

Figure 4.19: Ascent velocity vs flapping frequency.

4.6 Transition Dynamics

While the previous section discusses the differences in wing kinematics between individual fruit flies ascending at varying speeds, here we investigate the acceleration dynamics of ascending flight using data obtained from the apparatus previously described in Section 4.4.1. The most prevalent form of flight sequences resulting from this apparatus are akin to the voluntary-type take-off observed in [99]. In these sequences, we observe that the the fly takes off relatively quickly (but steadily), then eventually relaxes to a slower, steady-state ascent velocity[2].

[2]We also observe the escape-type response seen in [99] on occasion, but as the escape dynamics are more unsteady, they are not strictly ascending, but exhibiting more intricate motions.

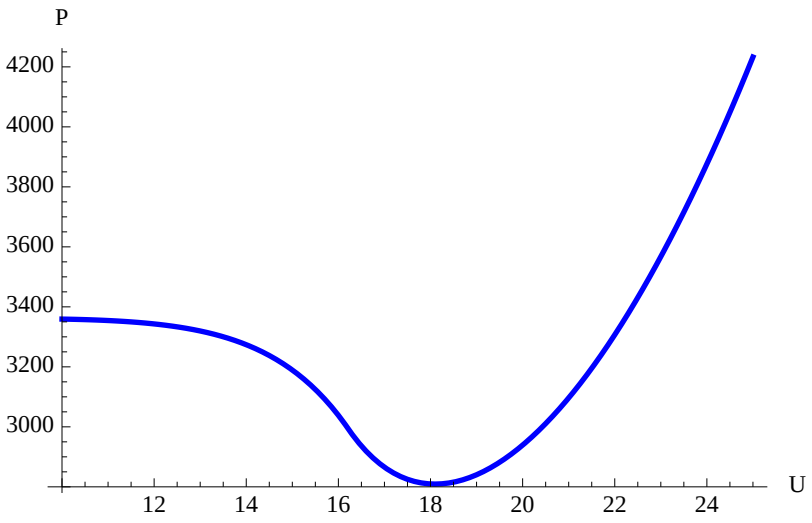

(a) Steady-state power vs horizontal velocity

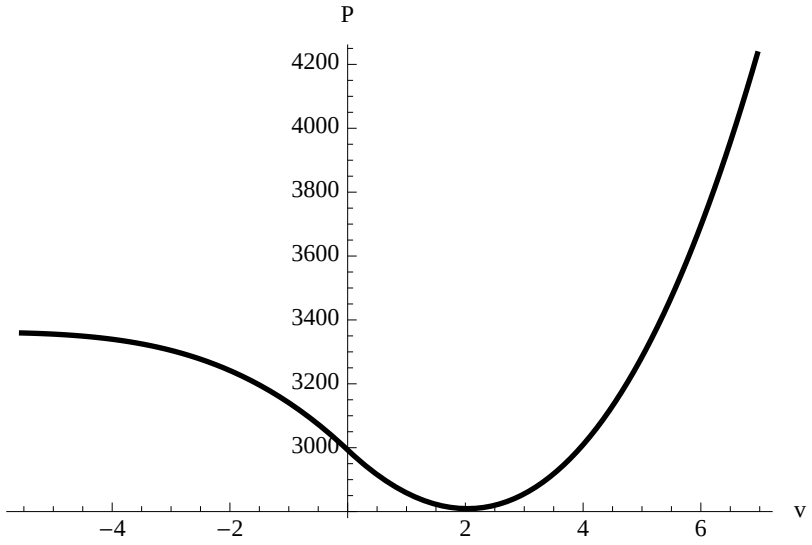

(b) Steady-state power vs vertical velocity

Figure 4.20: Plots of steady-state power vs U and v. Morphological parameters (i.e. C_L, C_D) are from the fit in Figure 4.16

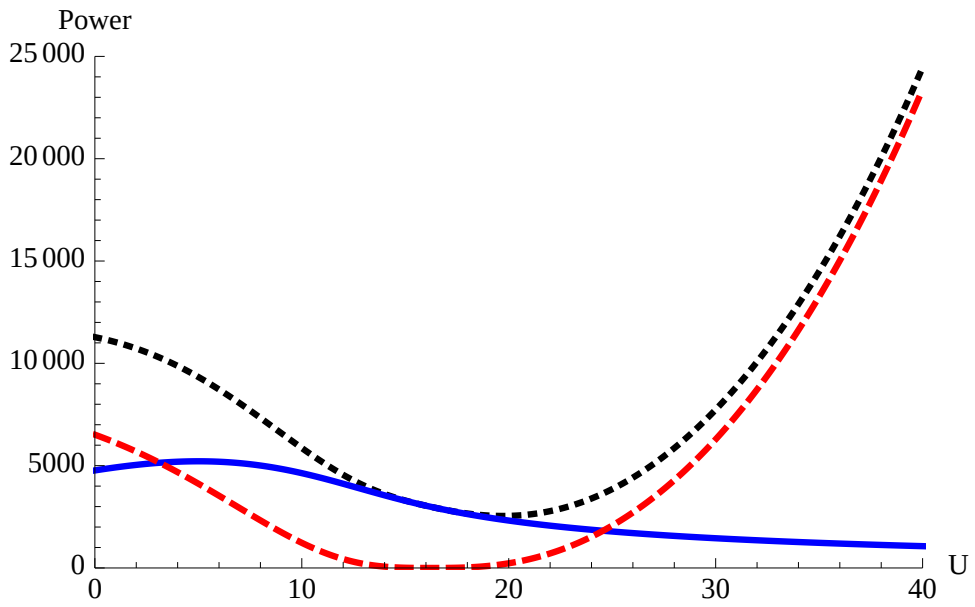

Figure 4.21: Contributions to the aerodynamic power of the ascending model. The solid line is the power required to overcome drag on the wings, the dashed line is the power required to overcome drag on the body, and the dotted line is the total power requirement.

An example sequence of this type of flight is seen in Figure 4.22, with plots of v, U, and α vs time displayed in Figure 4.23. Here, the insect enters the filming region with a vertical velocity of ≈ 34 cm/s then decelerates down to about 12 cm/s over the course of 24 wing beats. Over the course of the deceleration, we see a sharp decrease, followed by a smaller increase in U, with small variations on the order of 2^o in α. Perhaps more suggestively, we plot the same U vs v data and fit from Figure 4.16, but with the transition data superimposed. Here, it appears that the insect transits from one point along the steady-state curve ($v \approx 3$), decreases U so low that it overshoots the desired equilibrium value, and then gradually increases the horizontal velocity to the steady-state value of U corresponding to the desired final value for v (≈ 1).

This plot suggests the existence of some sort of control scheme which allows for quicker transitions between ascending states than simply changing U to its

final value and allowing the system to relax. This can be seen in Figure 4.25, which compares the observed transition data to the model dynamics under the simplest possible controller with

$$U(t) = \begin{cases} U_0 & \text{if } t \leq 0 \\ U_f & \text{if } t > 0 \end{cases} \tag{4.22}$$

and $v(t)$ found from simulating Equation 4.5 (all morphological parameters are those from the fit in Figure 4.16). The figure shows that the observed dynamics are much faster than the model's predicted relaxation, implying that the control the insect provides results in speeding-up its transition.

Additionally interesting is that not only does the chosen control scheme relax more quickly to the new steady-state ascent speed, but it also requires less power, as seen in Figure 4.26. Using (4.9), we can calculate the power consumed for both the observed stroke and the simple controller from (4.22). Performing this analysis, we see that the captured transition sequence requires less power than the quick-switching control mechanism. This difference is largely due to the fact that $U(t)$ is smaller for the data than for the model during the whole transition, resulting in the seen decrease.

4.7 Discussion

In the previous two sections, we have seen that ascending velocity in fruit flies is a steady-state endeavor which is controlled by tuning only one proverbial knob, the horizontal wing velocity, U. In addition, we have also seen that when transitioning from one ascent velocity to another, the insect uses a control scheme which allows for a more rapid relaxation to a new steady-state (and less power

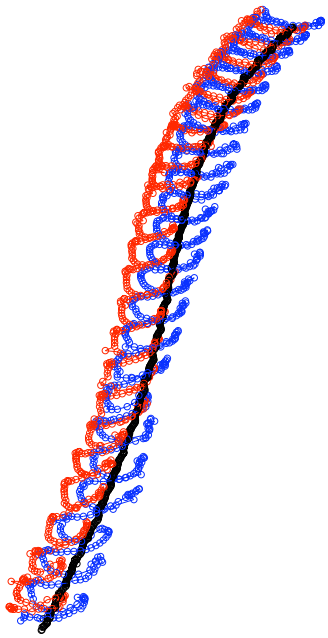

Figure 4.22: Sample transition sequence. As in Figure 4.12, the black dots are the body center of mass positions, the red dots are the right wing centroid positions, and the blue dots are the left wing center of mass positions. Each dot represents data from a single image frame. This particular example starts its ascent with a velocity of roughly 34 cm/s, eventually decelerating to about 12 cm/s

consumption) than simply instantaneously changing U (or, by extension, gradually changing it monotonically). Unfortunately, though, it is currently impossible to divine precisely the type of control used by the flies as we are working with low statistics and only viewing a portion of the transition which does not include the endpoints of the process.

Our results here, however, are potentially suggestive as to the types possible control schemes which the flies could invoke and their imperatives for using them, so we shall engage in a game of informed speculation which makes predictions for future studies. Specifically, the overshoot in controlling $U(t)$ is intriguing, as it causes the insect to decelerate towards its final ascent velocity more rapidly than the simple controller in the previous section. Also of interest is that the reversal in the slope of $U(t)$ happens fairly quickly, almost in a

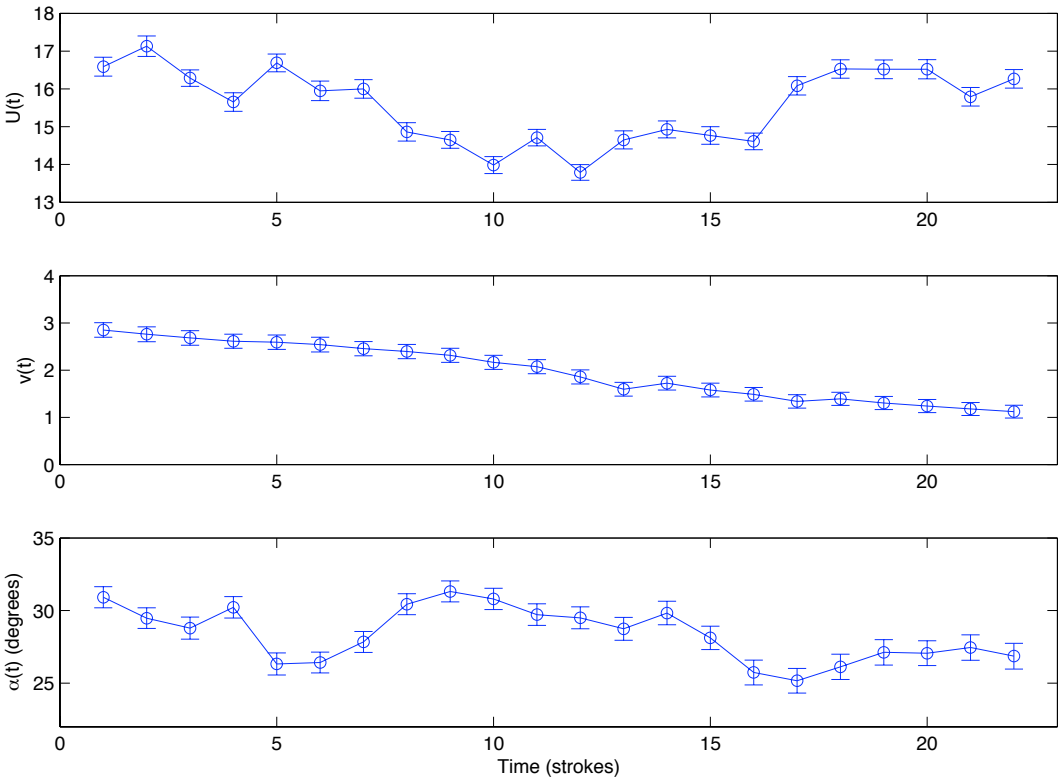

Figure 4.23: Plots of U, v, and α vs time for the sequence shown in Figure 4.22.

V-shaped pattern (Figure 4.27(a)).

One possibility for controlling U in this manner could be a to minimize (or at least deduct from) the transition time between differing ascent velocities. As it turns out, if we assume that motor inertia bounds the maximal rate of change of U [3] ($a \leq \frac{dU}{dt} \leq b$), it can be shown (and is in this chapter's appendix) through optimal control theory [100] that the controller which minimizes the relaxation

[3] We do not need to worry about bounding U itself, as it is clearly bounded from below by 0 and should never be increased past its initial value, as the insect is decelerating. The derivative bounds safely keep the solution away from $U = 0$, however.

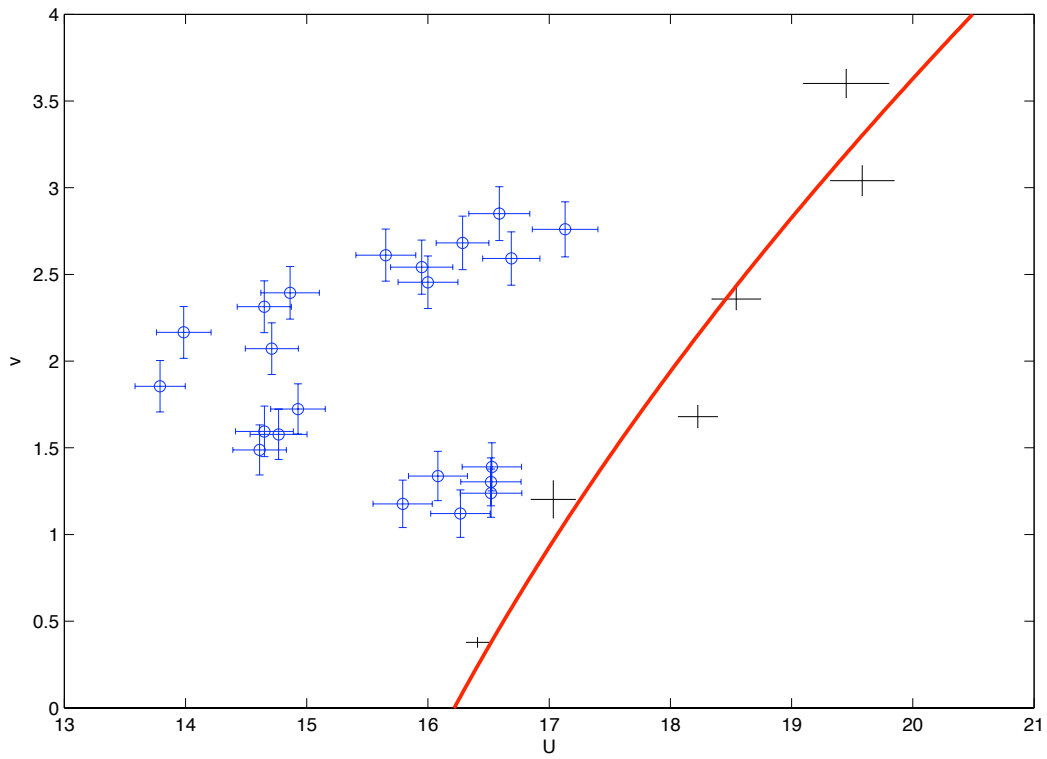

Figure 4.24: Deceleration sequence v vs U superimposed upon steady-state ascending data. The blue points on the left are the transition values, with v decreasing as a function of time. The red line is the model fit to the steady-state data, and the black points are the average values from the six steady-state sequences.

period is a bang-bang controller in the derivative of U which has the form of

$$\frac{dU}{dt}(t) = \begin{cases} 0 & \text{if } t < 0 \\ a & \text{if } 0 \leq t < \tau \\ b & \text{if } \tau \leq t < T \\ 0 & \text{if } t \geq T \end{cases}, \tag{4.23}$$

where T is the total time of the transition and τ is the cusp of the metaphorical V where $\frac{dU}{dt}$ abruptly changes. Integrating this equation with respect to t and

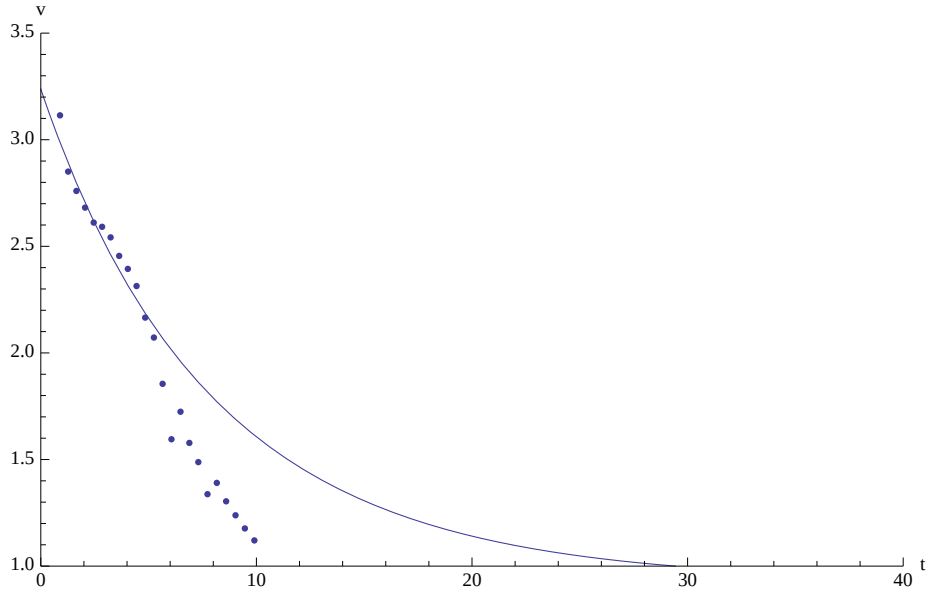

Figure 4.25: Comparison of v vs t between data (dots) and a simple control model (line).

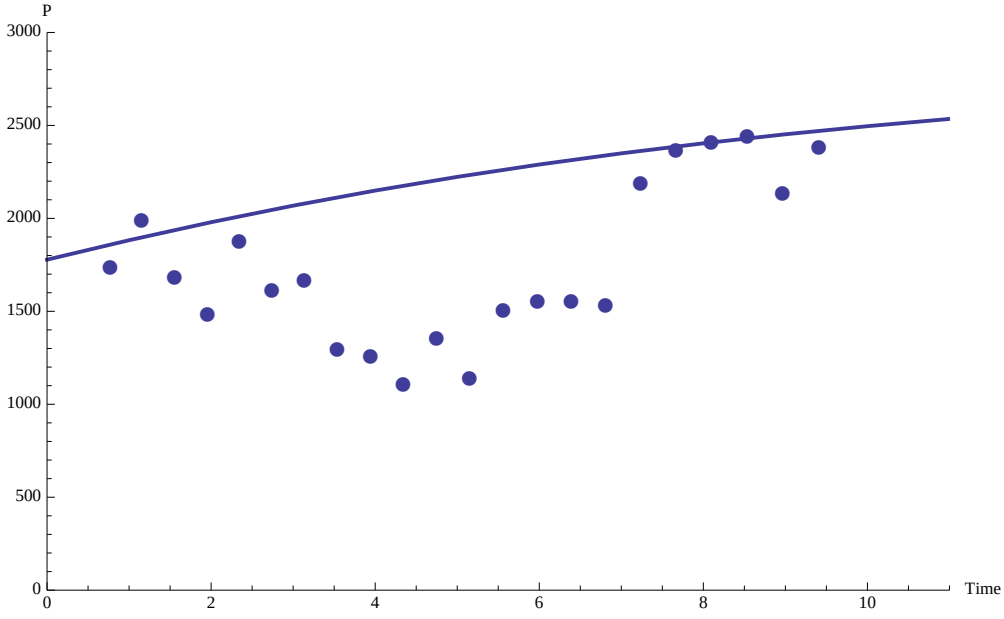

Figure 4.26: Calculated P vs t for data (dots) and the simple control model from Figure 4.25 (line).

enforcing continuity conditions, we find that

$$U(t) = \begin{cases} U_0 & \text{if } t < 0 \\ U_0 + at & \text{if } 0 \leq t < \tau \\ U_0 + a\tau + b(t-\tau) & \text{if } \tau \leq t < T \\ U_f & \text{if } t \geq T \end{cases}, \tag{4.24}$$

with

$$\tau = \frac{U_0 - U_f - bT}{b - a}. \tag{4.25}$$

Figure 4.27(a) displays a best fit of this model to the observed transition data ($U_0 = 19.5$, $U_f = 17.3$, $a = -.7$, $b = .6$, and $T = 13.0$), which, when simulating (4.5) with this form of $U(t)$, results in a much more (although not perfect) approximation to the experimental v dynamics (Figure 4.27(b)).

All this is only suggestive of a control scheme/imperitive, however, as it is based off of a single trajectory and makes an implicit assumption that an insect has a look-up table of sorts which gives v as a function of U. It could be, though, that instead of attempting to explicitly get from one ascent speed to another, there could be some internal or external trigger which discretely switches from one control type ($\frac{dU}{dt} = a$) to another ($\frac{dU}{dt} = b$) in a stereotyped manner. This potentially eliminates the need for a look-up table to exist.

This model also has no reliance on sensory input, which means that there are no corrections made for either motor errors or external perturbations. That being said, though, it is plausible that the controller used by a fruit fly is actually a PID-style controller ($\dot{U}(t) = K_P e(t-\tau_0) + K_D \dot{e}(t-\tau_0) + K_I \int_0^{t-\tau_0} e(t')dt'$, where $e(t)$ is an error function and τ_0 is a delay time) which mimics the observed bang-bang style method. There is a fair amount of evidence that insects are able to ascertain the magnitude and velocity of their relative flow field via their Johnston's

Organs, which are located in their antennae [101–103], and visual cues could be used, as dipteran species (although not explicitly *Drosophila melanogaster*) have been shown to exhibit flicker fusion rates at about twice their wing beat frequency [104, 105]. Hence, the use of sensory feedback is a distinct possibility during these sequences.

Despite these speculations, even if insects are indeed using a PID-type control that is consistent with a time-minimizing approach, this suggests that reducing the relaxation time might be an imperative in the flies' flight dynamics. Along with simply collecting additional statistics, this could be tested by perturbation experiments in which a fly ascending in steady-state experiences a force of some type that knocks it off this trajectory. Additionally, since the model here predicts maximal and minimal values for changing U, it might be possible to use this information to understand the maximal rate at which fruit flies can perform other maneuvers which rely on altering the magnitude of force production.

4.8 Summary

In this chapter, we have developed a simple model of fruit fly ascending flight and used it to gain further understanding of experimental data observing these maneuvers. We have found that given constant wing kinematics, there exists a steady-state ascent velocity, with the exception of the somewhat unphysical case of flight at very high angle of attack. Fitting an expansion of this model to the observed data, which was obtained via a custom-built filming arena, we find good agreement with the hypothesis that flies predominately control their wing velocity (and not their angle of attack) to alter their ascent speed. In the observed sequences, stroke amplitude is increased and flapping frequency is

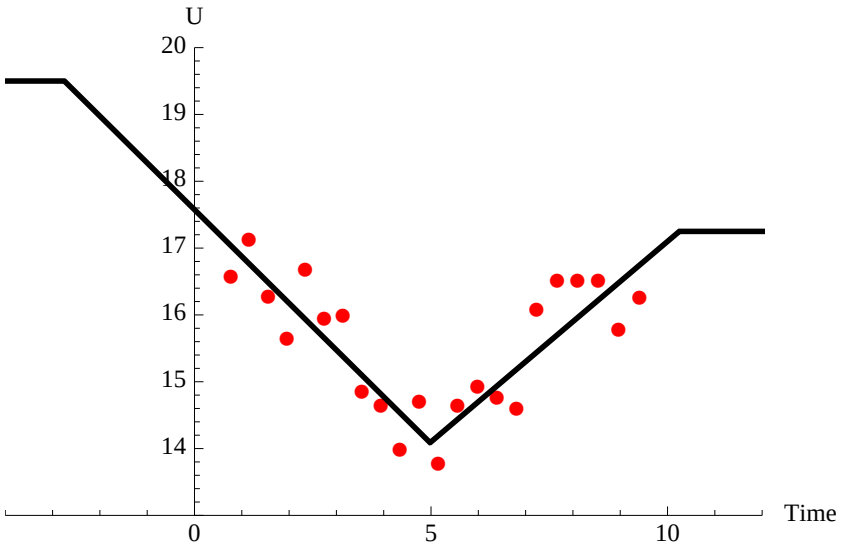

(a) U vs t

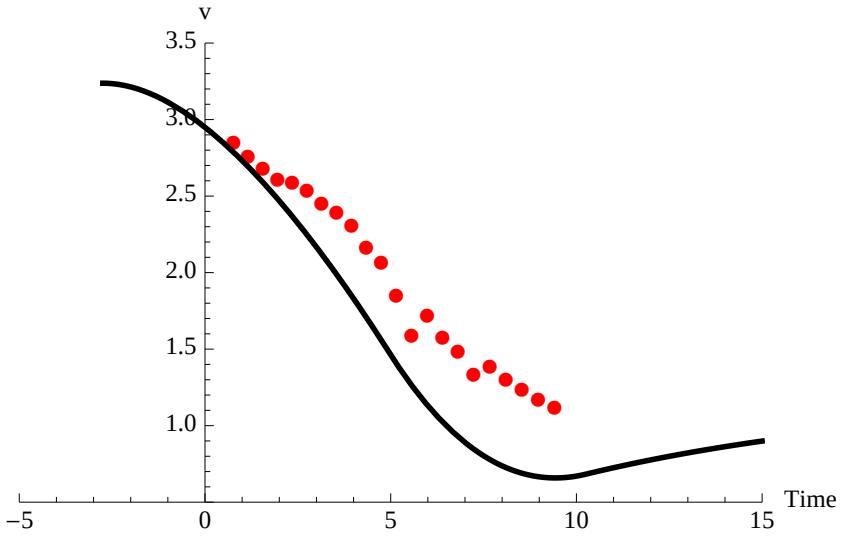

(b) v vs t

Figure 4.27: Plots of U and v vs time for transition sequence data (points) and the proposed controller (lines). The model for $U(t)$ is attained via a best fit of (4.24) to the data, and the model for $v(t)$ is found by plugging the predicted $U(t)$ into (4.5) and performing a forward simulation.

decreased in order to produce augmented vertical velocity.

We have also observed the transition of a fruit fly from a fast ascent to a slower vertical velocity. Through a V-shaped modulation of $U(t)$, the insect relaxes towards a steady-state far faster than possible with a simpler monotonic control. It is hypothesized that this type of velocity alteration helps to actuate a transition which is time-minimizing with respect to certain constraints. Further investigation is necessary, however, to understand this more fully.

APPENDIX:
Derivation of the Time-Minimizing Controller

As alluded to in Section 4.7, given the dynamics described in (4.5) and the constraint that $\frac{dU}{dt}$ must be bounded, we would like to show that (4.23) is indeed the time-minimizing form for the control of $U(t)$. Our approach will be to use methods from the calculus of variations to prove this.

Simplifying (4.5), we can write the dynamics for our system as

$$\frac{dv}{dt} = f_z(U, v) - 1, \tag{4.26}$$

with the control constraint that

$$a \leq \frac{dU}{dt}(t) \leq b. \tag{4.27}$$

The quantity we wish to minimize, the transition time, T, can be written such that

$$T = \int_0^T dt = \int_0^\gamma \frac{dz}{v}, \tag{4.28}$$

where z is the altitude of the insect and $\gamma = z(T)$. We can exchange z for t here because we assume that the insect's vertical velocity is always greater than zero. Hence, t is a single-valued function of z.

Furthermore, if we trickily define $g(z) \equiv \frac{1}{2}v^2$, we have that

$$\frac{dg}{dz} = \frac{d}{dz}\Big(\frac{1}{2}v^2\Big) = v\frac{dv}{dz} = v\frac{dv}{dt}\frac{dt}{dz} = \frac{dv}{dt} = f_z(U, g) - 1. \tag{4.29}$$

Using this, we will then rewrite our equation for T so that

$$T = \int_0^\gamma (2g)^{-1/2} dz. \tag{4.30}$$

Similarly, we can rewrite (4.27) so that

$$a \leq \frac{dU}{dz}\frac{dz}{dt} \leq b \iff \frac{a}{\sqrt{2g}} \leq \frac{dU}{dz} \leq \frac{b}{\sqrt{2g}}. \tag{4.31}$$

Lastly, we need to find a way of welding (4.29)-(4.31) into a cohesive functional. We shall perform this through the Lagrange multiplier method, but with one more trick required. Namely that in our equations' current state, the inequality constraint cannot be trivially written in a form which is equal to zero. We alleviate this, however, by introducing a new control variable, $r(z)$. If we insert

$$r^2 - \Big(\frac{1}{\sqrt{2g}}\frac{dU}{dz} - a\Big)\Big(b - \frac{1}{\sqrt{2g}}\frac{dU}{dz}\Big) \tag{4.32}$$

as an equality constraint into our variational functional, this neatly takes care of our dilemma, as $r \in \mathfrak{R}$ if and only if our derivative is in the appropriate range.

Putting all of this together, we define

$$J = \int_0^\gamma \Bigg\{(2g)^{-1/2} + \sigma_1\Big[\frac{dg}{dz} - f_z(U,g) + 1\Big] + \sigma_2\Big[r^2 - \Big(\frac{1}{\sqrt{2g}}\frac{dU}{dz} - a\Big)\Big(b - \frac{1}{\sqrt{2g}}\frac{dU}{dz}\Big)\Big]\Bigg\}dz, \tag{4.33}$$

where σ_1 and σ_2 are Lagrange multipliers. Now, we can apply the Euler-Lagrange equation,

$$\frac{\partial J}{\partial q_i} - \frac{d}{dt}\left(\frac{\partial J}{\partial \dot{q}_i}\right) = 0, \tag{4.34}$$

to all of the generalized coordinates, q_i, of the system.

As it turns out, for our purposes we only need to look at two generalized coordinates to find the desired functional form. With respect to r, we have that

$$\frac{\partial J}{\partial r} - \frac{d}{dt}\left(\frac{\partial J}{\partial \dot{r}_i}\right) = 2\sigma_2 r = 0. \tag{4.35}$$

Hence, either σ_2 or r must be equal to zero. Performing this with respect to $U(z)$ and solving for $\frac{d^2U}{dz^2}$, we find that

$$\frac{d^2U}{dz^2} = \frac{-1}{\sigma_2}\left(\text{Stuff not involving } \frac{d^2U}{dz^2}\right). \tag{4.36}$$

Hence, if $\sigma_2 = 0$, our acceleration in U is singular, which cannot happen for more than a finite number of points along our trajectory. Therefore, in order for

(4.35) to hold away from the singularities, $r = 0$. As a consequence then,

$$\Big(\frac{1}{\sqrt{2g}}\frac{dU}{dz} - a\Big)\Big(b - \frac{1}{\sqrt{2g}}\frac{dU}{dz}\Big) = 0, \tag{4.37}$$

which implies that either

$$\frac{1}{\sqrt{2g}}\frac{dU}{dz} = a \text{ or } \frac{1}{\sqrt{2g}}\frac{dU}{dz} = b. \tag{4.38}$$

Substituting our definition of g back in and reworking this a little bit, we find that

$$\frac{dU}{dt} = a \text{ or } \frac{dU}{dt} = b. \tag{4.39}$$

Since our flight sequences are decelerating while ascending upwards, this implies that the lower bound must occur first, followed by the upper bound. Accordingly,

$$\frac{dU}{dt} = \begin{cases} 0 & \text{if } t < 0 \\ a & \text{if } 0 \le t < \tau \\ b & \text{if } \tau \le t < T \\ 0 & \text{if } t \ge T \end{cases}, \tag{4.40}$$

which mirrors the result of (4.23).

CHAPTER 5

SLOPPY MODELING AND THE EFFECT OF THE FITNESS LANDSCAPE

5.1 Introduction

Given a particular morphology, what is the best way that an insect can fly? This was the question asked in the Chapter 2, which defined ”best” as energy-minimizing while still maintaining hovering flight, optimizing flight kinematics for fruit fly, bumblebee, and hawkmoth morphologies. Although the optima were found and some rudimentary sensitivity analyses were performed in the aforementioned chapter, we wish to expand our knowledge of the optimal basin in which the solutions reside. This will be attempted through the analyses in this chapter.

The first section here is a brief foray into the idea of modeling hovering insect flight as a ”sloppy” system in a manner similar to that described in [36–39]. To put it another way, the basic question we ask is whether a hovering insect has great freedom in some parameter space direction and little in others. This will be stated in a more formal manner later, but the basic idea is that in many eigendirections in a naturally parameterized system (i.e. the parameters have a physically meaningful/measurable interpretation) will have an importance on the cost function fitness that wildly varies [36, 38]. We find that our parameterization of insect flight displays this type of sloppy behavior.

After this, we study several of the local optima which are less efficient than the global optima. Do they display the same sort of sloppiness? Are they just little bumps along a compliant direction in parameter space, or are they legitimately different strategies? If that latter, what are the energy barriers between the different optima?

Finally, we see if ideas from sloppy modeling can aid in predicting spread within a population. Namely, we ask if the variations in kinematic data we observe in experimental data of fruit fly flight are predominantly along the compliant directions of the energy landscape.

5.2 Model Summary

The model of insect flight used is nearly identical to that used in Chapter 2. The insect wing is modeled as a rigid body supporting a point mass. Morphological data is taken from prior experiments in the literature (Table 2.2). The wings can rotate in three degrees of freedom, referred to as ϕ, θ, and η (Figure 2.1). ϕ is the azimuthal angle, θ is the vertical deviation, and η is a measure of wing pitch about the radial axis. The positions of these three axes are specified as a periodic function of time. Fluid forces are determined from a quasi-steady model of insect flight described in [40]. From the prescribed kinematics and fluid forces, it was shown previously that it is possible to calculate the lift production, L, and the power consumption, P, resulting from a particular hovering wing motion via equations 2.13-2.15.

The specific parameterization used is as follows:

$$\phi(t) = \frac{\phi_m}{\sin^{-1} K} \sin^{-1}[K \sin(2\pi f t)] \tag{5.1}$$

$$\theta(t) = \theta_m \cos(4\pi f t + \Phi_\theta) + \theta_0 \tag{5.2}$$

$$\eta(t) = \frac{\eta_m}{\tanh C_\eta} \tanh[C_\eta \sin(2\pi f t + \Phi_\eta)] + \eta_0. \tag{5.3}$$

This adds up to an 10 value paramaterization of a wing stroke. The energy-minimizing values of these parameters for the three insects discussed here were found in [106] via a clustering genetic algorithm which constrains the produc-

tion such that L is equal to M, the total mass of the insect. The analysis which occurs in the sections to follow can be viewed as an expansion about these points.

5.3 Sloppy Modeling Analysis

5.3.1 Hessian Calculations

The basic principle behind the sloppy analysis discussed in [37] lies with finding the Hessian of some cost function near an optimal solution. As the cost function in our model is the power consumption, P, we have that

$$H_{ij} = \frac{\partial P}{\partial x_i \partial x_j}. \tag{5.4}$$

It should be noted that in most of the papers describing sloppy modeling, the derivatives defining H_{ij} are with respect to the logarithms of the parameters, as this allows for parameters of wildly varying scales to be compared. In our parameterization, however, all parameters, with the exception of the flapping frequency, are of the same order (and are unitless). Hence, we can just use the partial derivatives with respect to the parameters themselves.

Two difficulties exist with this particular analysis, however. Fortunately, it is possible to "kill two birds with one stone," and eliminate them both using the same trick. First is that the flapping frequency can vary in size by a couple orders of magnitude from the other parameters. Also, and more importantly, this is a constrained optimization problem (if unconstrained, the power-minimizing solution is that the insect just refuses to flap its wings). Although it is possible to deal with constrained problems via the idea of a bordered Hessian, we can take advantage of a feature of our system to make the analysis easier. This feature is that both L and P are monotonically increasing functions of f, the flapping fre-

quency. Hence, if a wing stroke produces positive lift, this lift can be increased to exactly match the insect weight, Mg. And since P monotonically increases with f, we can say that the optimal frequency for a given set of kinematic parameters is precisely the frequency which satisfies $L = Mg$. Hence, we have reduced our 10 dimensional parameter space model to a 9 parameter manifold.

This manifold is found by using a binary search in f such that the constraint was met to within $M \times 10^{-10}$ for a given set of 9 parameters, $\vec{p}$. This results in a cost evaluation, $C(\vec{p})$. The Hessian is then numerically determined via

$$H_{ij} = \frac{C(\vec{p} + h_i\hat{e}_i + h_j\hat{e}_j) - C(\vec{p} + h_i\hat{e}_i) - C(\vec{p} + h_j\hat{e}_j) + C(\vec{p})}{h_i h_j} + o(\|\vec{h}\|^2), \tag{5.5}$$

where $\vec{h}$ is the vector of step sizes, and $\hat{e}_i$ is the unit vector in the parameter i direction. For the analyses to follow, h_i was set to be 10^{-5}, but the results do not change significantly for smaller values of h_i.

Given the Hessian, we then determine the principle axes by finding the eigenvectors and eigenvalues of H. The eigenvectors give the principle directions of variation, while the absolute values of the eigenvalues give the relative strengths of the corresponding directions. This is shown pictorially in Figure 5.1. For the 2-D space shown in this figure, the eigendirections are shown as arrows within the smallest ellipse. One can view crossing ellipses as a change in model behavior. Hence, there is much more room for variation in the longer elliptical axis than in the shorter axis. For higher dimensions this can be understood as N-dimensional ellipses. In the sloppy models referenced in [36–39], the spectrum of these eigenvalues ranges up to about 6 orders of magnitude.

In order to get a sense of which individual parameters (in the natural parameterization) are most constrained, we use a stiffness metric, s_m, which is defined as

$$s_m = \frac{\sum_{i=1}^{9} |\lambda_i| v_i^{(m)2}}{\sum_{i=1}^{9} |\lambda_i|}, \tag{5.6}$$

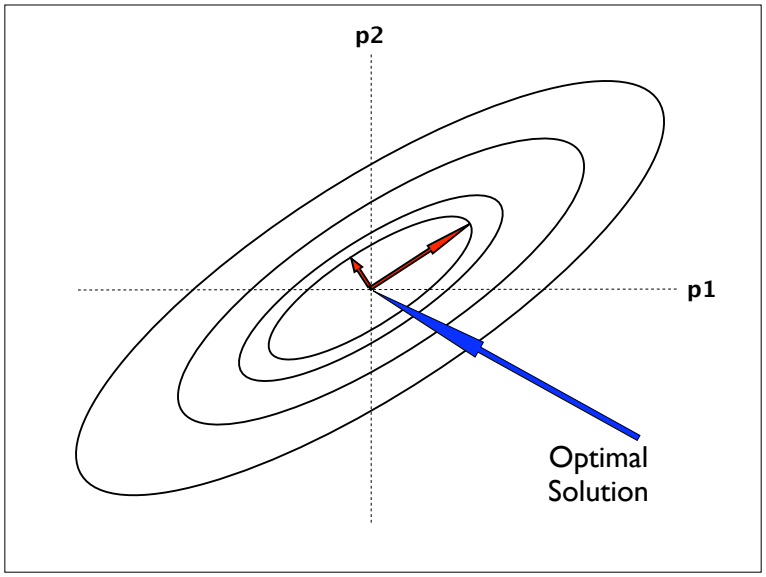

Figure 5.1: Hessian behavior near optimum

where λ_i is the ith eigenvalue and $v_i^{(m)}$ is the mth component of the corresponding eigenvector. Hence, a larger s_m implies the parameter m is more constrained. Note how in this definition, the $\sum_m s_m = 1$.

5.3.2 Results

The results for the fruit fly Hessian are seen in Figures 5.2 and 5.3. The minimum about which the Hessian is calculated is the same as in [106], found via a clustering genetic algorithm. Figure 5.2 shows the composition of the eigenvectors of H and Figure 5.3 shows the corresponding eigenvalues. The order of the parameters in Figure 5.2 is displayed in Table 5.1. As seen in Figure 5.3, we see a relatively continuous (i.e. no large separation between important and unimportant directions) spectrum of eigenvalues which spans about 3 orders of magnitude. While this is smaller than the 6 orders seen in cellular biology

systems, the system also involves an order of magnitude smaller number of parameters. As expected, the eigendirections, for the most part, do not align with the parameter space bases, much like in the previously observed systems. Additionally, looking at the stiffness of the parameters (Figure 5.4), we see that in the local vicinity of the optimal solution, 4 parameters were significantly more constraining than others. Namely, these are ϕ_m, K, θ_m, and Φ_θ. What this tells us is that on the $L = M$ manifold, the constraints accorded to parameters related to azimuthal and stroke plane displacements ($\phi(t)$ and $\theta(t)$) are large with respect to the variables related to wing rotation ($\eta(t)$).

This last result is particularly interesting, as much attention has been focused on understanding the process of wing rotation [27, 67, 75, 107], while there has been considerably less interest in the other two degrees of freedom. Two explanations exist for this. The first is that the wing rotation effects are due to unsteady effects, such as interaction with a leading edges vortices [108], which are not taken in account in the quasi-steady model used here. Secondly, the importance of wing rotation in the landscape could be more global in nature, as opposed to the local picture given here. Although exploring the former reason is beyond the scope of this chapter, we will look at the latter in Section 5.4

These analyses were also performed for the bumblebee and hawkmoth systems (not shown), resulting in nearly identical eigenvectors/values.

Table 5.1: Parameter order

1	ϕ_m
2	K
3	θ_m
4	Φ_θ
5	θ_0
6	η_m
7	η_0
8	C_η
9	Φ_η

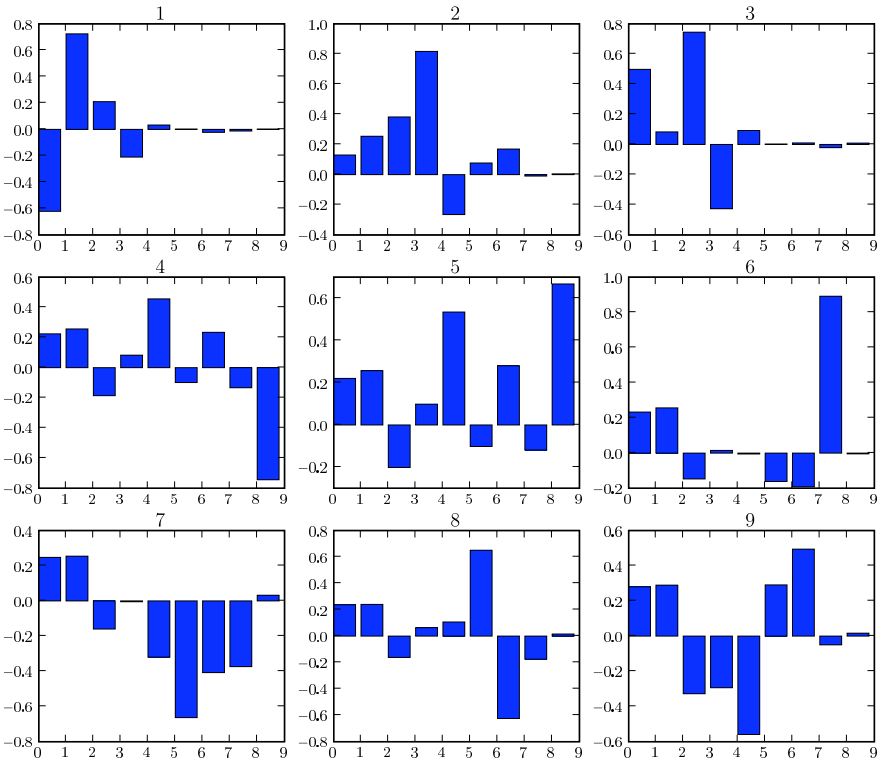

Figure 5.2: Fruitfly eigenvectors

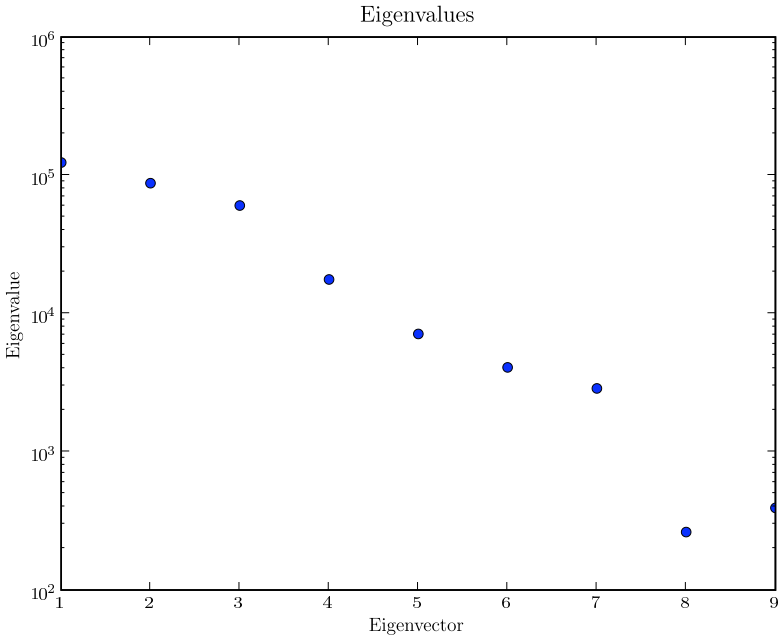

Figure 5.3: Fruitfly eigenvalues

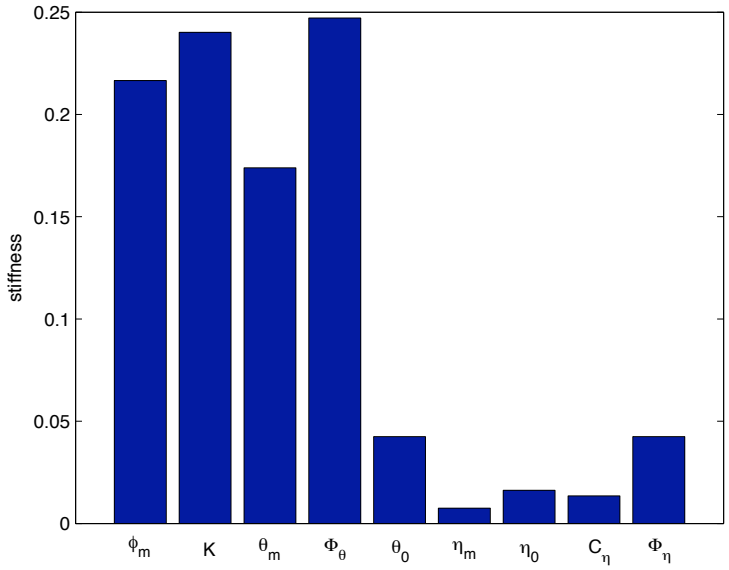

Figure 5.4: Fruitfly stiffness values

5.4 Analysis of Local Optima

5.4.1 Method for Generating Local Optima

Approximately 200 local optima of the system were found by running a modified version of the adaptive niching particle swarm optimization (ANPSO) [109, 110] method. The basic idea is that the landscape is filled with many particles. These particles have velocities and move about the parameter space paying attention to the energy of their current location, the lowest energy solution that the individual has found, and the lowest solution each of its neighbors has found. Although particle swarm optimization was originally developed to find the global minimum of a function [109], it can be made into a niching algorithm with a clever set-up of how the particles interact with each other. Essentially, if two particles remain close to each other for some fixed amount of time, they start communicating with each other, with the definition of "close" being adaptively altered as a function of the system state. When several of these particles become grouped together permanently, this group is considered a niche, and will converge unabated to a nearby local minimum.

For the study here, this algorithm was run 5 times, concentrating on the fruit fly morphology, resulting in several hundred unique local optima. Of these, we will focus only on the 52 optima found which have specific powers less than the somewhat arbitrary cutoff of $35\frac{W}{kg}$ (see Figure 5.5). This, by no means, gives a complete listing of all of the space's local optima, but should serve as an adequate starting point for our investigations.

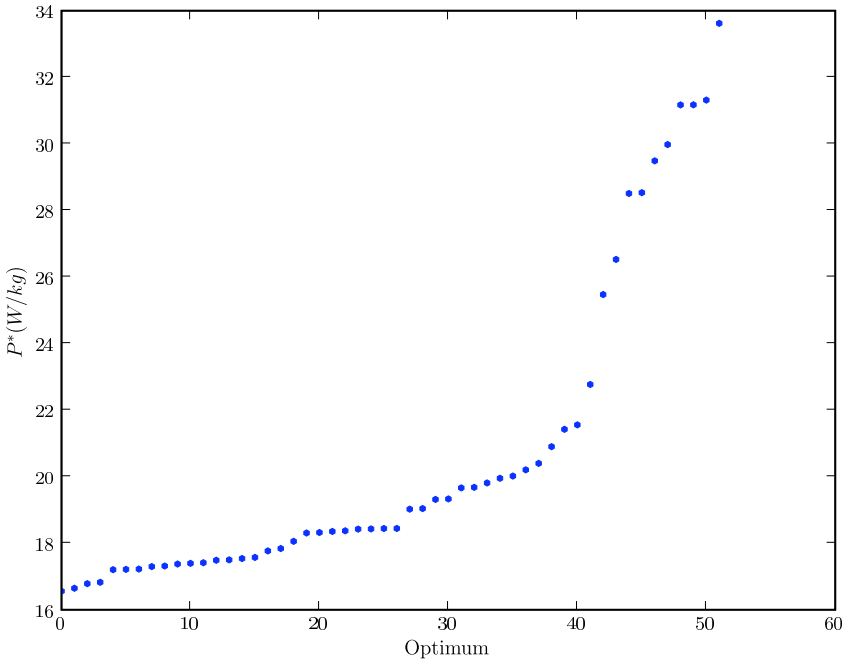

Figure 5.5: Specific powers of studied optimal solutions

5.4.2 Results and Discussion

The most striking thing one notices about these optima is that looking in some planes, only a discrete set of points or clusters of points exist, while in others, a more continuous distribution is seen. For example, if one looks at the optima in the ϕ_m vs. f plane (Figure 5.6), most of the optima lie on or near a curve $\phi_m f = c$, where c is a constant. This is what we would expect from classical airfoil theory. Looking at the η_0 vs. Φ_η plane however, we see a far more discrete structure, with five discrete points around which the optima are located. Similar dichotomies are seen when looking at the other planes. One of the questions which motivates this investigation is if the local optima lie along compliant directions of phase space, or are the optima legitimately different solutions. What these results seem to imply is that the answer is, well, yes. For cases such as ϕ_m vs. f, we see a continuous variation along what appears to be a type of optimal basin. For many other planes, however, there are blatant discontinuities

in phase space which suggest that different or mirror-symmetric strategies are being used.

To understand the various strategies found via the optimizations better, the optima are clustered via the k-means algorithm [111], aided by visual inspection, thereby grouping the 52 optima into 11 distinct classifications (Figure 5.8). The analysis of Section 5.3 was then applied to the lowest-energy sample from each classification, finding the Hessian eigenvectors and eigenvalues (Figure 5.9). As seen previously, each of these optima have a Hessian eigenspectrum which spans somewhere between two and four orders of magnitude. Also, observing the stiffnesses for the optima (as defined in (5.6)), we find that the five most efficient strokes display the same essential unimportance of the rotational degree of freedom (excepting a surprisingly large dependence on C_η for the upper-left stroke of Figure 5.8). The less optimal strokes do show commensurate dependence on the $\eta(t)$ parameters, but they by no means dominate.

So does this imply that rotational parameters are unimportant in this optimization scheme? No, just that they are unimportant locally. Although infinitesimal differences in these parameters have relatively small effects, there are certain areas of parameter space which are just plain bad, resulting in horrendously unacceptable efficiencies (i.e. $\Phi_\eta = 3\pi/4$ or $\eta_0 = \pi/4$). This is why the parameter spaces in these $\eta(t)$-related variables display the discrete strokes seen in Figure 5.7, whereas $\phi(t)$- and $\theta(t)$-related variables show more continuous distributions.

The question remains, however, if this result is physically or biological interesting. A possible theory is that the relative compliance of the wing rotation degrees of freedom could allow for increased manueverability, as small changes in rotation angle could turn a body, but not highly penalize an insect in either

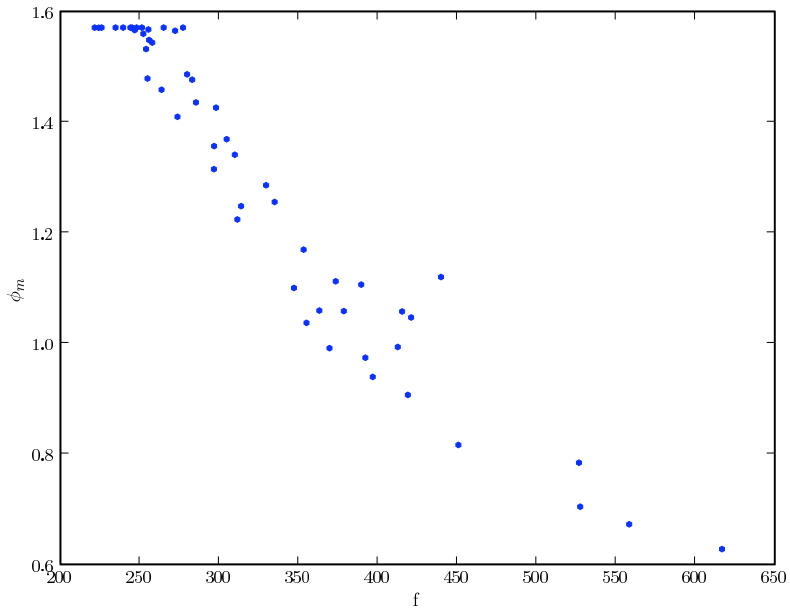

Figure 5.6: Stroke amplitude vs. frequency for local optima

lift or energy. Another potential theory is that the decreased sensitivity could allow for a more robust passive mechanism for rotating the wing. Since the basin of attraction must be relatively large in order to remain stable under small perturbations, the "sloppiness" in the rotational degrees of freedom could facilitate this.

The lack of sensitivity on the angular coordinates could also be a result of a proposed drag ratcheting control mechanism [75,76]. This idea states that since lift $\propto \sin 2\alpha$, whereas drag $\propto \sin^2 \alpha$, and since insects use angles of attack near 45^o, small variations in α have little effect in lift, while causing a relatively large shift in drag. Hence, with slight angel of attack modulations, drag can be used to steer flight.

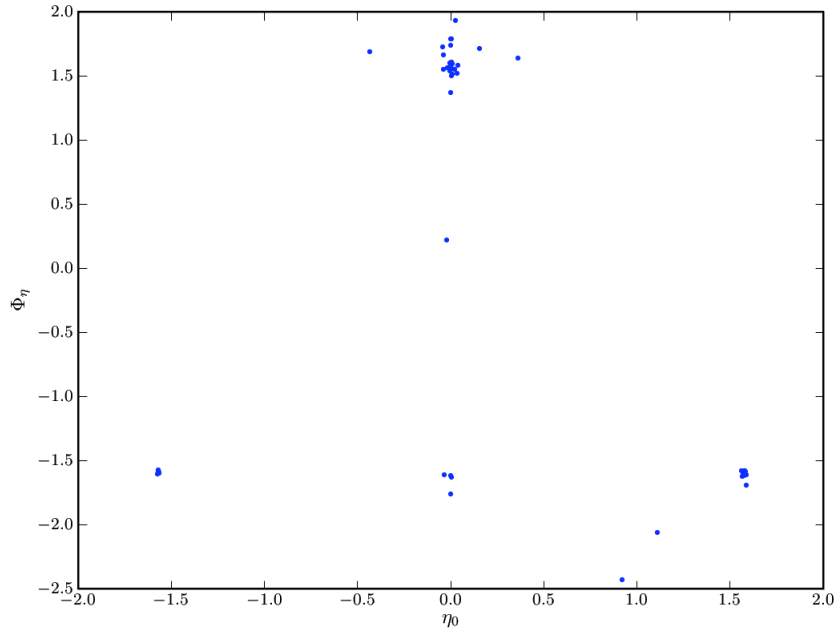

Figure 5.7: Rotation phase vs. rotation offset for local optima

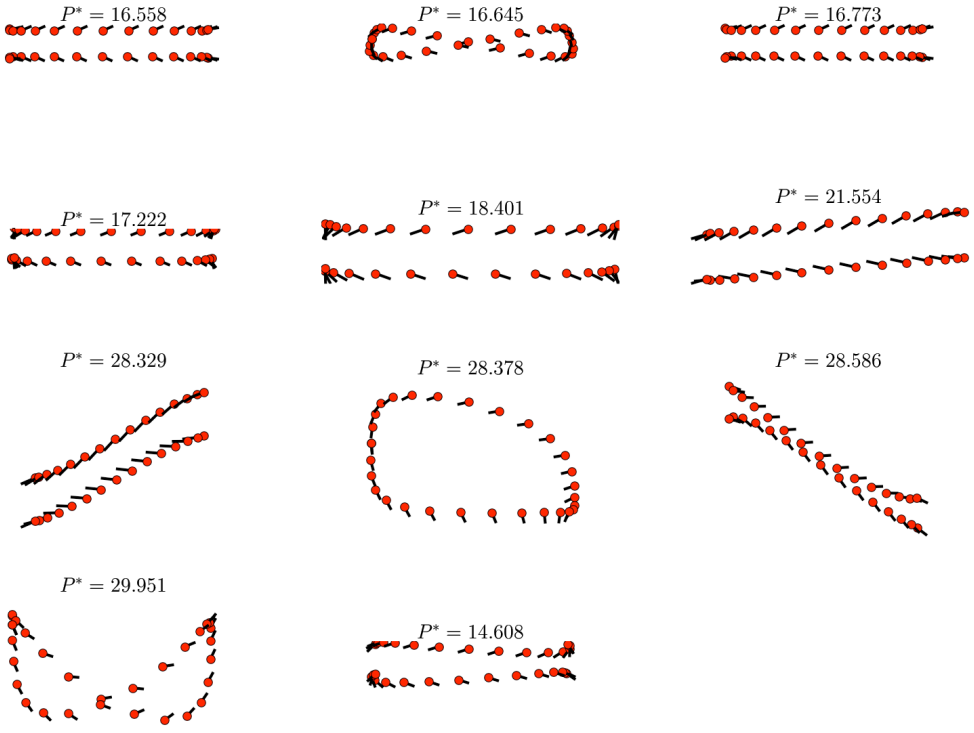

Figure 5.8: Locally optimal strokes

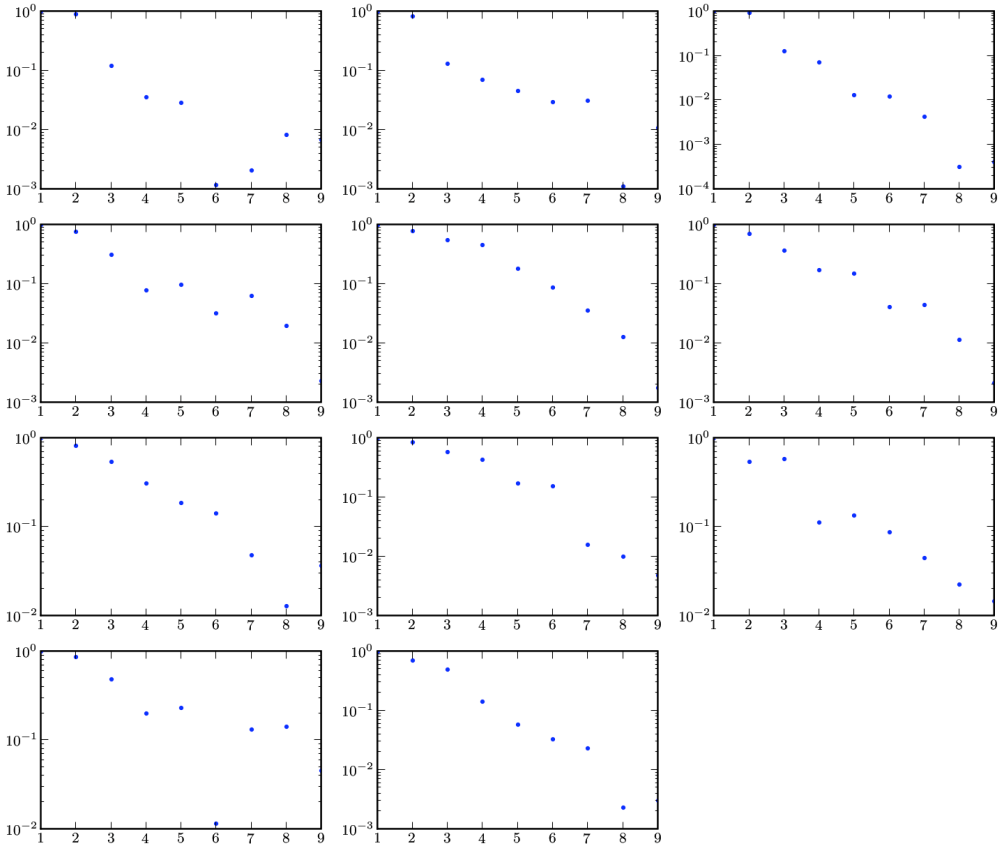

Figure 5.9: Locally optimal Hessian eigenvalue spectra (order corresponds to Figure 5.8)

5.4.3 Energy Barriers and Grouped Optima

The final analysis performed on the local optima was to measure the straight-line energy barrier between the 11 optima seen in Figure 5.8. The straight-line energy barrier is defined as the highest energy point located on the straight line in the landscape that starts at one minimum in parameter space and ends at another. More formally, if minimum 1 is at point $\vec{x}$ and minimum 2 is at point $\vec{y}$, then the straight-line energy barrier, B, is defined by

$$B(\vec{x}, \vec{y}) = \min_{0<r<1} F(\vec{x} + r(\vec{y} - \vec{x})) - \max(F(\vec{x}), F(\vec{y})), \tag{5.7}$$

where F is the function which calculates the energy. Although this is only an upper-bound on the calculation of the actual energy barrier, as a lower energy

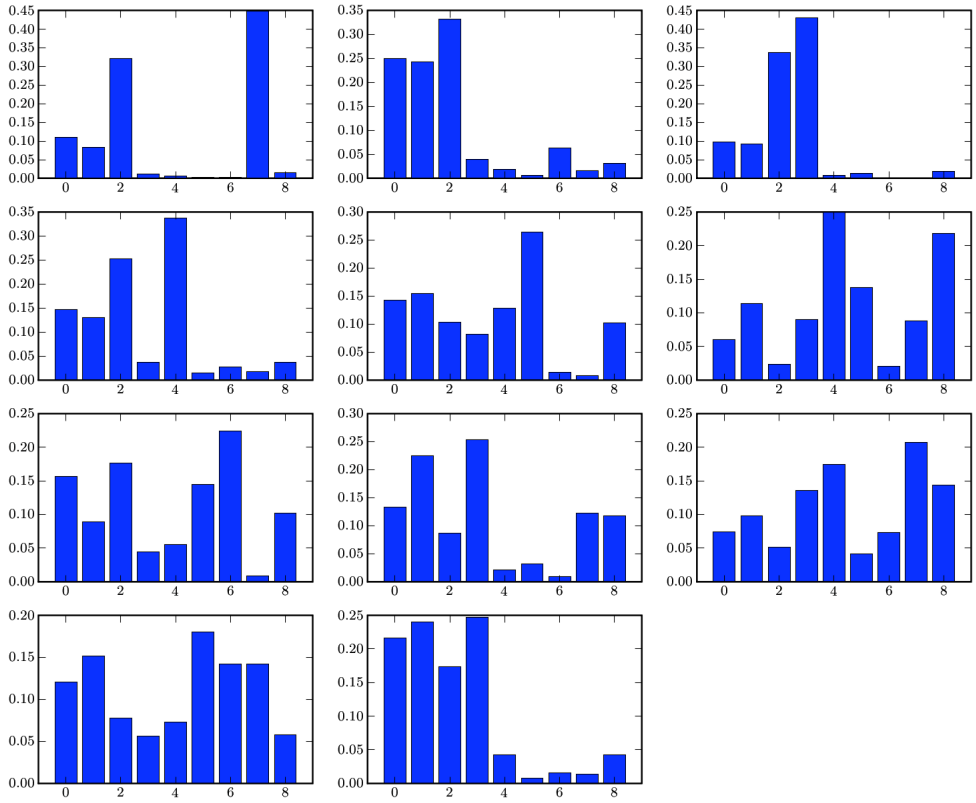

Figure 5.10: Locally optimal stiffnesses (order corresponds to Figure 5.8). The first 2 bars are $\phi(t)$ parameters, the next 3 are related to $\theta(t)$, and the last 4 to $\eta(t)$

path may be found through traversing a more convoluted path, it can serve as a first order approximation to begin investigations. A nudged elastic band method (or one of its many variants) would most likely be useful for this type of calculation [112, 113].

Essentially, two types of barriers were found, exemplified in Figure 5.11. The barriers either tended to be small (under $\approx$ 100 W/kg) or large (several orders of magnitude larger. This observation of a distinct cutoff leads to the idea that perhaps given sufficient evolutionary "temperature," perhaps an organism can jump between these basins of attraction which are only separated by a relatively small barrier. This leads to the idea of a graph of basin connectivity. For such a graph, each of the local optima are considered nodes. Lines are drawn between

these nodes if the B between them is less than some cutoff – here, 100 W/kg. Performing this analysis, we see the result in Figure 5.12. Note how most of the optima can reach each other through some pathway. This community structure on the graph also includes the global optima (the far right-center dot), implying that many of the local optima could be within striking distance of the global optimum. Looking at Figure 5.13, we can see the reason why some optima are not connected – they are distinct (or mirror-symmetric) strategies which are locally optimal, but physically isolated away from the global optimum in parameter space.

This brings us to perhaps the most apparent flaw with this type of analysis, the fact that the parameterization of a wing stroke does not correspond to the space of possible biological variations. For instance, there could be a single mutation which takes a wing stroke to its mirror-symmetric stroke, meaning that the actual barrier needed to be crossed is significantly smaller than the barrier predicted in our Euclidean parameter space. This, perhaps, suggests the utility of a more mechanical or experimentally-derived parameterization for wing motions [74] for not only the analyses of this section, but for the whole of the work in this chapter.

5.5 Predicting Population Variation

When confronted with any biological data (or, really, any data), some spread exists. Not all insects are doing precisely the same thing. Some of this spread is due to experimental uncertainty, but there is also legitimate biological variation between strokes. Some insects are doing different things from other insects. Since variation is an important factor which drives evolution, it would be of in-

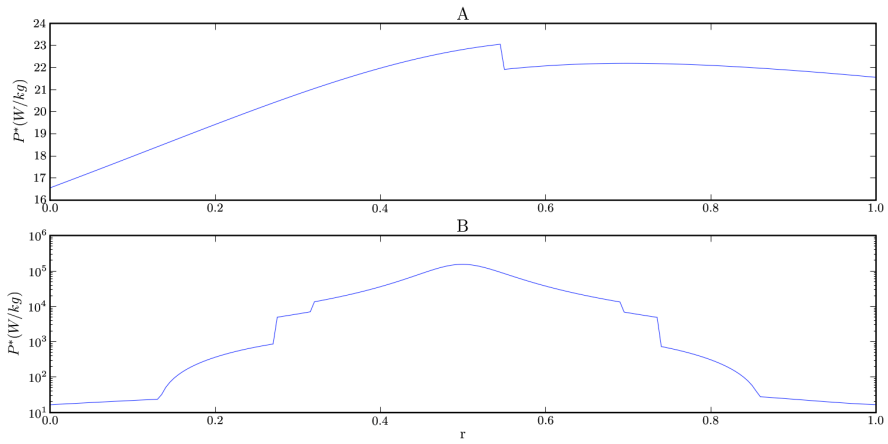

Figure 5.11: Two examples of straight-line energy barriers

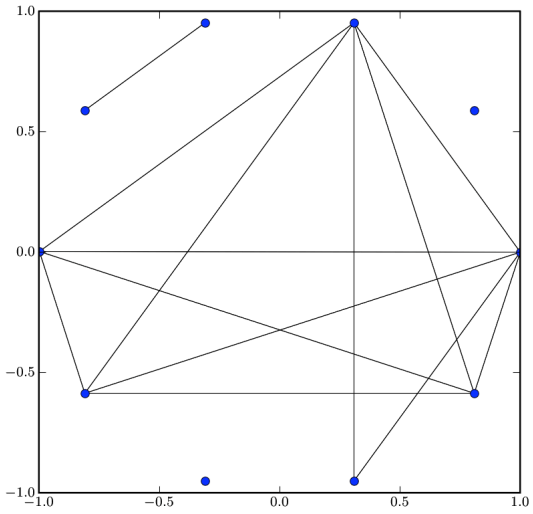

Figure 5.12: Connectivity graph for local optima of the fruit fly model. Each dot represents a local minimum, and a line between dots implies that the maximum barrier height between them is no greater than 100 W/kg. If one assumes that 100 W/kg is the maximum barrier height which can be crossed, then most of the minima can reach the global minimum (the dot at (1,0)) with a series of barrier jumps.

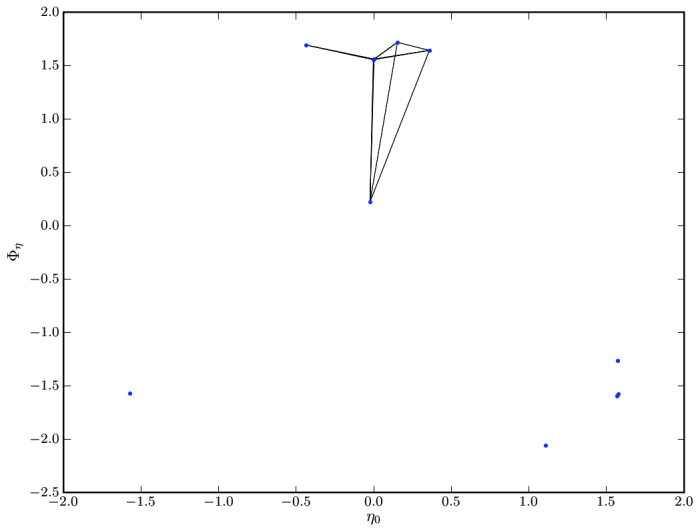

Figure 5.13: Connectivity graph for local optima of fruit fly model plotted in the η_0 vs. Φ_η plane

terest to probe the manners in which the wing strokes vary. Are all the observed wing strokes of similar efficiency, or are some much worse than others? Can we say something about the particular manner in which they vary using an optimization/sloppy modeling paradigm, or are physical or historical constraints more important?

These are questions we investigate in the remainder of this chapter using the previously described sloppy-modeling framework. To be more specific, we hypothesize that observed insect kinematics should have more spread in directions in which the the landscape is more compliant (small eigenvalues of H), and less when the landscape is stiffer (larger eigenvalues), a cartoon of which is displayed in Figure 5.14.

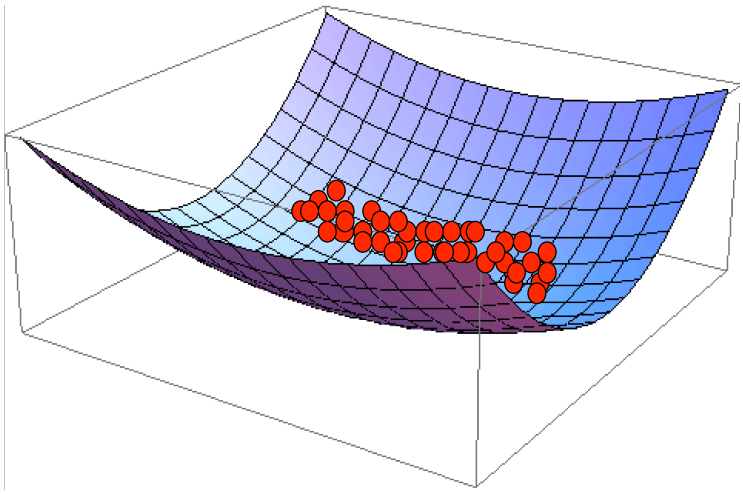

Figure 5.14: A cartoon of data varying along a compliant direction in parameter space

5.5.1 Cost Function and Parameterization

Here, we once again use the model from Chapter 2 for estimate force and power production, but with a couple of changes. First, instead of the parameterization from (5.1)-(5.3), we would like to use a more general form which allows for reasonable comparisons to experimental data.

Specifically, we parameterize the wing strokes via a Fourier series with L modes. Namely,

$$\phi(t) = \phi_0 + \sum_{n=1}^{L} A_n^{\phi} \sin(n(\omega t + \psi_n^{\phi})) \tag{5.8}$$

and so on for calculating $\theta(t)$ and $\eta(t)$. This parameterization is useful because it encompasses a wide variety of strokes and is convenient when comparing with experimentally obtained kinematics. One disadvantage, though, is that number of parameters needed to describe the stroke is relatively large, requiring $6L + 4$ parameters ($2L + 1$ per angle, plus one for the frequency). As it turns out, however, the frequency winds up factoring out when calculating C, leaving us with $6L + 3$ parameters. Also disadvantageous is that the parameters do not always have a straight-forward intuitive meaning.

Given this parameterization, however, we still have the problem that our landscape needs to only contain points which meet the constraint that $\langle F_z \rangle = mg$. As it turns out, though, it is possible to factor the frequency out of both the vertical force production, F_z, and the power output, P [114]. Since $F_z \propto f^2$ and $P \propto f^3$, we can then define a non-dimensional cost,

$$C = \bar{c}\sqrt{\rho_f}\frac{P}{F_z^{3/2}}, \tag{5.9}$$

where ρ_f is the density of the fluid and $\bar{c}$ is the average chord length of a wing (the morphological factor in front of the fraction serves to eliminate the units).

Given a particular set of parameters, forces and powers for a particular stroke are calculated using a quasi-steady model of aerodynamic forces coupled with inertial forces, as in [106]. We also can compute these forces for 3D free-flight of hovering fruit flies data obtained by Leif Ristroph in Itai Cohen's lab (the method for which is described in Chapter 3) and make comparisons with the optimal solutions[1]. This is achieved by taking time series data (approximately 35 data points per period) and fitting them to a Fourier series via the FFT algorithm. To simplify the analysis, we use only the first 5 terms of the series to avoid over-fitting issues. Data was taken for three species of fruit flies, *Drosophila melanogaster* (32 wing strokes), *Drosophila virilis* (28 wing strokes), and *Drosophila grimshawi* (26 wing strokes) of varying size. Being more specific, *melanogaster* have a body mass of a approximately 1 mg, *virilis* are about 2 mg, and *grimshawi* weigh in at around 3.5 mg. But since all morphological parameters can be scaled out of $\frac{P}{F_z^{3/2}}$ from (5.9), we can overlay these species all upon the same landscape in our model, despite their size differences.

Finally, it should be mentioned that for the parameterizations used in our

[1]For the purposes of this chapter, we define hovering as having an acceleration of less than $.1g$.

studies, we are not privy to a simple landscape. Mainly as a result of the various phase angles involved in the problem, the landscape is often littered with protruding bumps and copious local optima, as exemplified in the example in Figure 5.15. To simplify the problem slightly, we focus only on the landscape near the kinematic data, analyzing the problem from the context of local, not global, optimization. In fact, most of the analysis which follows makes a tacit assumption that we are looking only in the local neighborhood of some local minimum of the landscape. This is somewhat convenient anyway, as it allows us to use the Hessian formalism from Section 5.3. Of course, this approach has its limitations, so we shall discuss them later.

5.5.2 Results

Experimental Data

First, we present the results of analyzing the experimental data to see what sort of variations are present in the data. Figure 5.16 shows a typical example of the this. Here, the phases of the first two Fourier modes (ψ_1^θ and ψ_2^θ) are plotted against each other. We see that the variation in the data is much larger (about an 8-fold difference) along the ψ_1^θ axis than in the ψ_2^θ direction. In total, we see about 2 orders of magnitude difference between the largest and smallest variations (Figure 5.17).

Just looking at the magnitude of the variations is slightly misleading, however. For example, if we allow some parameter p is redefined to be $p^* = 100p$, then we have changed the magnitude of variation by two orders of magnitude without changing any information about the system. One way we can take care

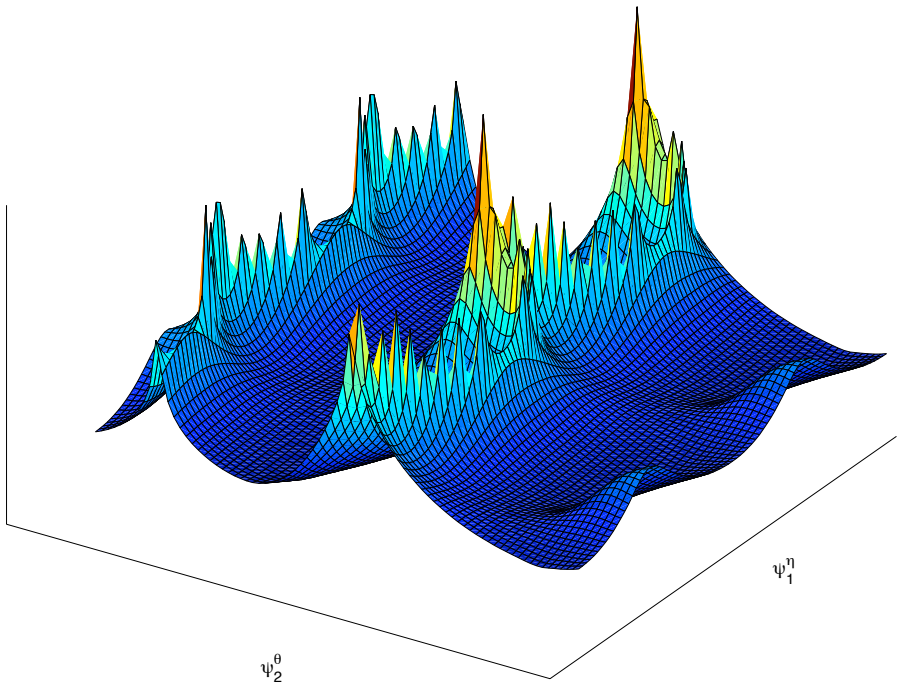

Figure 5.15: Cost landscape of ψ_2^θ vs. ψ_1^η for the fruit fly system. This plot takes a wing stroke, fixes all parameters but the two aforementioned phase angles, and varies only two parameters, generating this surface plot. The complexities which arise from having a non-convex landscape with singularities such as this example lead to focusing mainly on the local structure of the landscape, ignoring some of the complicated global structure.

of this is by normalizing the deviations by the absolute value of the parameter's mean, but this does not help if a parameter has a mean value of zero.

Fortunately, we can take advantage of our system's parameterization to aid us. Namely, we have three types of parameters: offsets, Fourier amplitudes, and phase angles. Ignoring the offsets, we know that Fourier amplitudes, by definition are greater than zero[2], and that phase angles must always be between

[2]Technically, the amplitudes could be zero, but experimentally, the amplitudes from the fit are always finite, hence making the mean positive

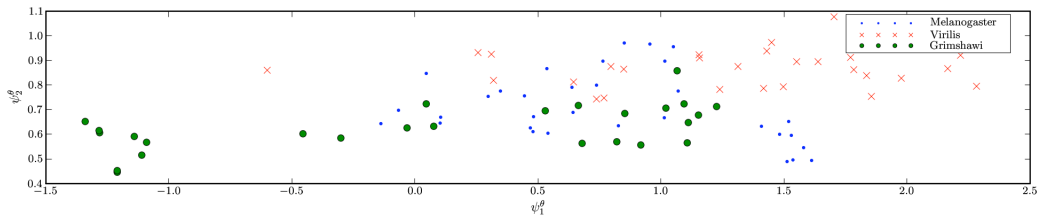

Figure 5.16: Measured phases for the first two Fourier modes of θ for fruit fly kinematics. Note the nearly order of magnitude difference between the variation in one phase compared to the other.

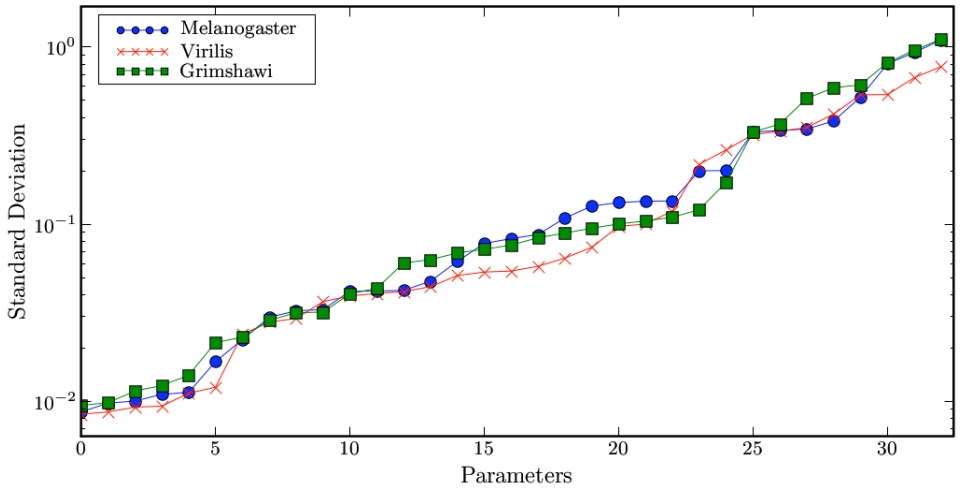

Figure 5.17: Plot of measured standard deviations vs. parameters (in no particular order) for the three species of fruit flies. We see a total of about 2 orders of magnitude between the smallest and largest variations.

$-\pi$ and π, and, hence, can always be compared directly without normalization. Therefore, one comparison we can make is to see if there is any correlation between variation in a Fourier Amplitude and variation in its corresponding phase angle (Figure 5.18). Although the statistics are still small, we still see an identifiable trend in the three species where as normalized variation in the amplitude increases, so does variation in the associated phase angle. This implies that the less constrained an amplitude is, the less constrained its phases are.

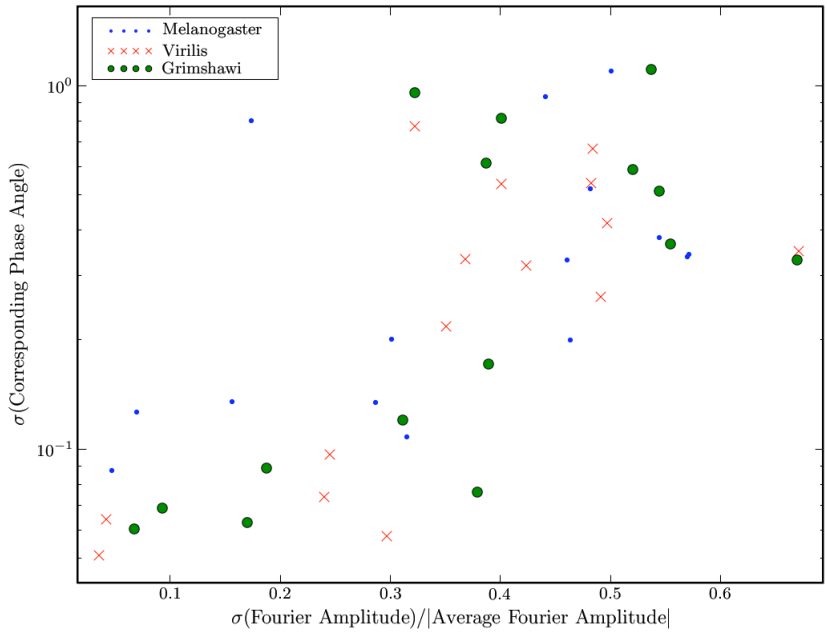

Figure 5.18: Phase variation vs. normalized amplitude variation

Overlaying Data on the Landscape

Before we talk about more quantitative measures of how the experimental variation correlates with the landscape generated by calculating Equation 5.9, it is helpful to have a more pictorial, qualitative understanding of how the two ideas meld together. We can achieve this through 2D landscape plots. These plots, similar to the schematic displayed in Figure 5.1, are two-dimensional contour maps of the cost landscape, assuming that the remaining parameters are unchanged. For the purposes of this write-up, we will take the non-varying parameters to be those of the local optimum within the basin of attraction populated by the experimental data and see in Figure 5.19 (found using a Conjugate-Gradient method [115] initialized from one of the found strokes[3]).

The first of these plots, Figure 5.20 shows the landscape corresponding to the raw data displayed in Figure 5.16 (ψ_1^θ vs. ψ_2^θ). For this case, the landscape is ef-

[3]This same solution was found using several different strokes as initial conditions.

fectively one-dimensional, as the optimal wing stroke's first Fourier amplitude in θ is very close to zero, while the 2nd mode is much larger (corresponding to a figure-8 like motion). We see that all the observed data lies within 30% of the optimal parameter set, with much more variation along the first phase than on the second, as seen previously. Hence, for these two parameters, the difference in variation can be accounted for by the lack of stiffness in the first Fourier phase as compared to the second. Figure 5.21 shows a similar result to this, except now within a legitimately two-dimensional landscape. The data points are all clustered near the local optimum, approximately varying as if filling up the nearby ellipses.

We begin to see where our pretty picture starts to become slightly washed-out as we look at Figure 5.22, though. Although we do see variation along the more compliant direction, the data points are not clustered nicely about some local optimum. This may be partially due to the fact that the cost variations are not horribly large between the optima, so there is not a large amount of pressure to keep very close to the optimum, but this is not the case for some of the cases to follow. For example, Figures 5.23 and 5.24 show experimental data which is offset from the local optimum, resulting in costs which are 2-4 times higher than the local optimum.

So what information can we glean from these plots? First, that our world prediction isn't perfect, but then again, it would have been surprising if it was. But what might be more interesting is studying why in particular the theory breaks down. These failures might be the fault of the model (after all, we are neglecting unsteady effects and have a somewhat simplistic model of mechanical power consumption) or some form of systematic error in the data collection/fitting process. It is also possible, as noted in our analysis of the different

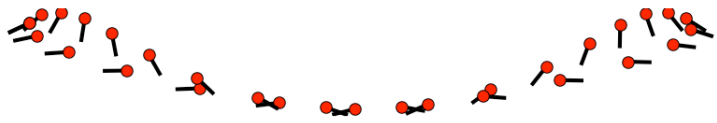

Figure 5.19: Locally optimal wing stroke calculated from experimental data

local minima, that the parameterization we have chosen is not an appropriate one to describe the wing motions.

But more intriguing is that these locations where our prediction is challenged could be the result of the organisms not "wanting" (as I do my best to anthropomorphize natural selection...) to optimize flight cost, or, not being able to do so. For example, in Figure 5.24, we see that the data points are located "southwest" of the local optima in the space of first ϕ and η Fourier amplitudes. But what is not on the plot is the fact that the wings, being solid objects and all, cannot pass through each other. Therefore, the first A_1^ϕ can never be greater than $\pi/2$ (assuming the two wings are performing the same stroke). Additionally, due to the elastic nature of the wing muscles, it is more costly to move the wing when it is near the head than when it is near its base on the thorax. Hence, this forces the wing to have a slightly sub-optimal (at least in the sense of our model) amplitude in the ϕ direction. This is just one example of how the biology of the system feeds back into the model and tells us what are some of the primary constraints which have acted on these creatures' flight evolution, and perhaps, could give us a better sense of precisely the sort of problems they are up against.

Hessian Analysis

In light of the results from the previous section, it seems somewhat superfluous to perform the Hessian analysis outlined earlier, seeing as how our data does

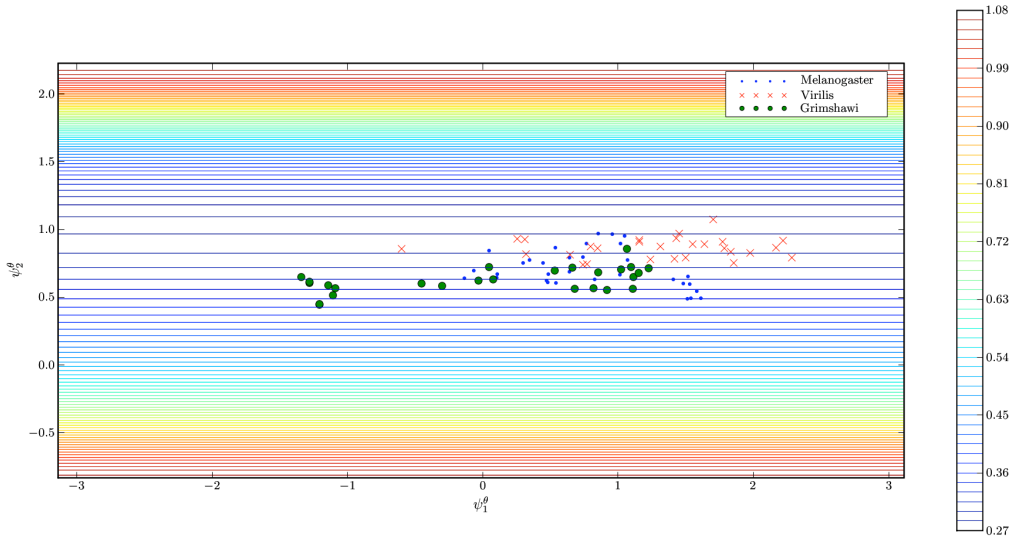

Figure 5.20: First and second phase angles for θ

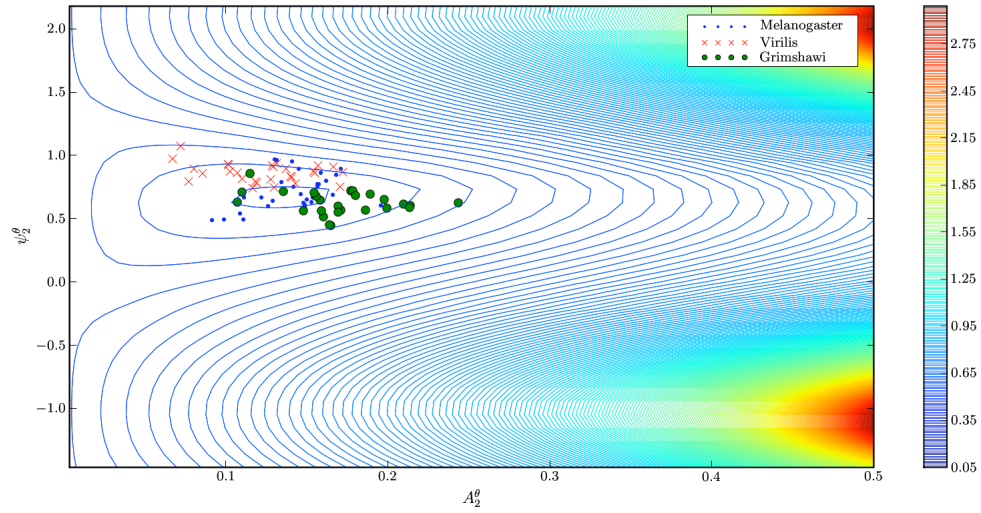

Figure 5.21: Amplitude and phase for the 2nd θ Fourier mode

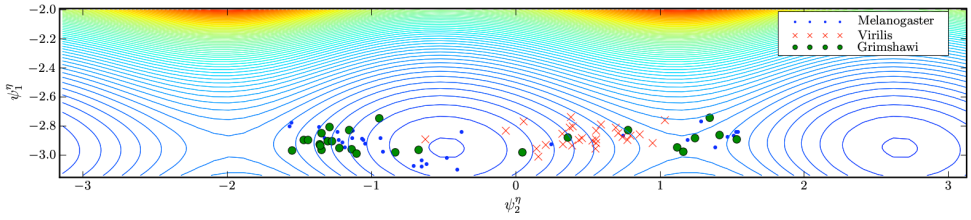

Figure 5.22: First and second phase angles for η (contour lines: blue = .2, evenly spaced by .05 up to red=3.)

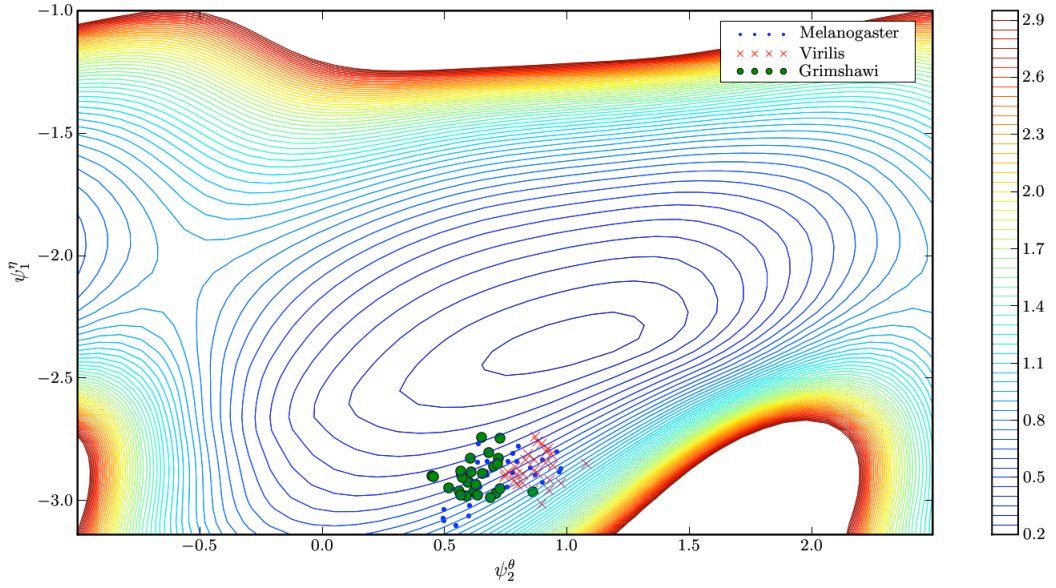

Figure 5.23: Second θ phase angle and the first η phase angle

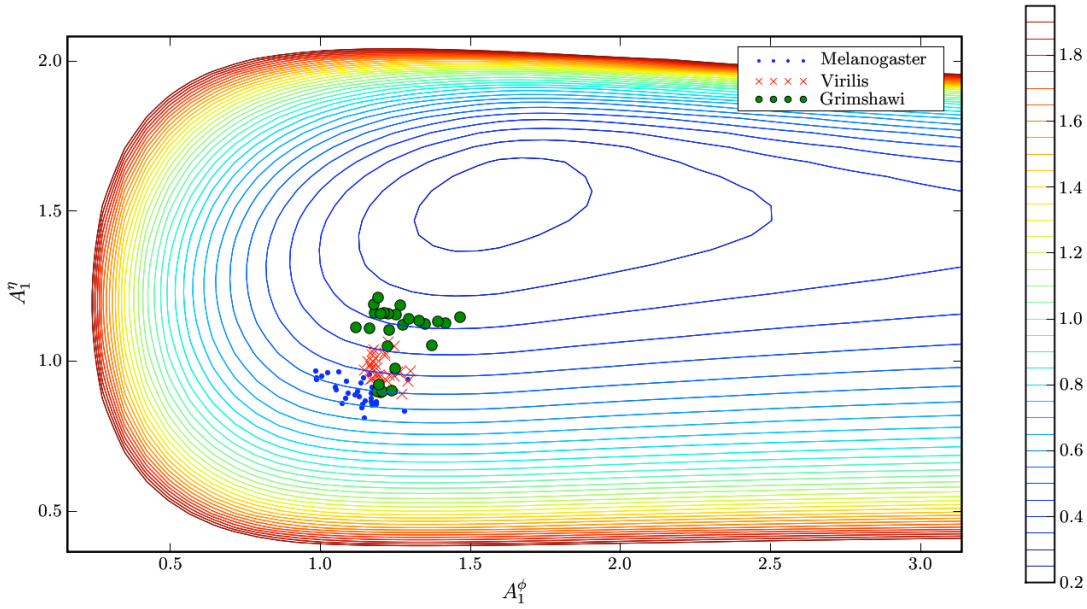

Figure 5.24: First Fourier amplitudes for ϕ and η

not lie precisely near the local optimum. However, we can still obtain some information about the local optimum itself, and if we assume that the eigendirections of the Hessian do not change as one moves away, we can see if variations along these bases correlate with the corresponding eigenvalues. It's not a perfect analysis, and ideally, we would like to have an analysis that works further away from the optimum, but has the potential to serve as a useful one, even if not a definitive one.

Calculating the Hessian using Equation 5.4, we see the eigenvalue spectrum of the Hessian about the optimal stroke from Figure 5.19 (Figure 5.25). Note that the eigenvalues range about 8 orders of magnitude continuously, with three smaller eigenvalues appearing at the end. This implies that our parameterization is "sloppy" in the sense that we cannot separate (unless arbitrarily) unimportant modes from more important ones, as there is a continuous stretch of eigenvalues over many orders of magnitude.

Given the eigenvectors and eigenvalues, we can then calculate the stiffnesses as prescribed in Equation 5.6. From this, we see that for the ϕ and η modes, most of the stiffness resides in the odd Fourier modes (both amplitude and phases). Although the stiffness decreases as the mode increases for both cases, it is much more striking for η. Additionally, the η offset also is important, as it helps set the mid-stroke angle of attack. For θ, however, the even Fourier modes are stiffer than the odd ones – which is consistent with the Figure-8 style stroke seen in Figure 5.19.

We now attempt to compare these results to the experimental variation. We can do this in two manners. First, if we recalculate the standard deviations in the eigenbases (as opposed to in the original parameterization), then we can compare these deviations directly to their corresponding eigenvalues. Makeing this

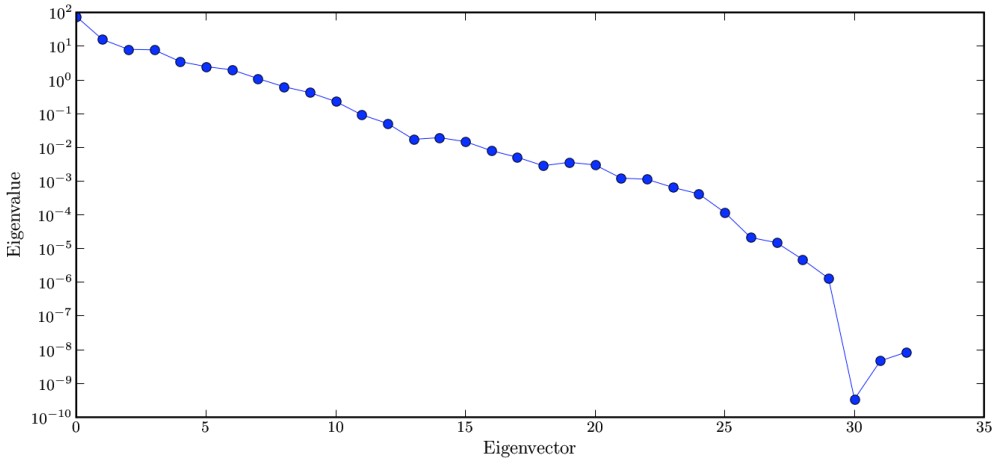

Figure 5.25: Eigenvalue spectrum of the Hessian near the locally optimal stroke

plot (Figure 5.27), we see that, although somewhat noisy[4], larger eigenvalues are significantly correlated with smaller normalized standard deviations. This meshes with our expectation that larger eigenvalues should be more constraining than smaller ones. We also see this sort of result when plotting parameter stiffness as a function of experimental variation in that parameter for the three species (Figure 5.28), although the plot breaks down for smaller eigenvalues, most likely due to insufficient statistics.

5.5.3 Discussion

Aside from obtaining additional data, there are several challenges needed to more fully understand the relationship between the landscape and population variations. First, we need to have a better characterization of the experimental error in comparison to the variation. If the error in measuring and fitting the Fourier coefficients is of comparable size to the observed variation, then we

[4]In order to get sufficient statistics to compile this plot, data from the three species were lumped together.

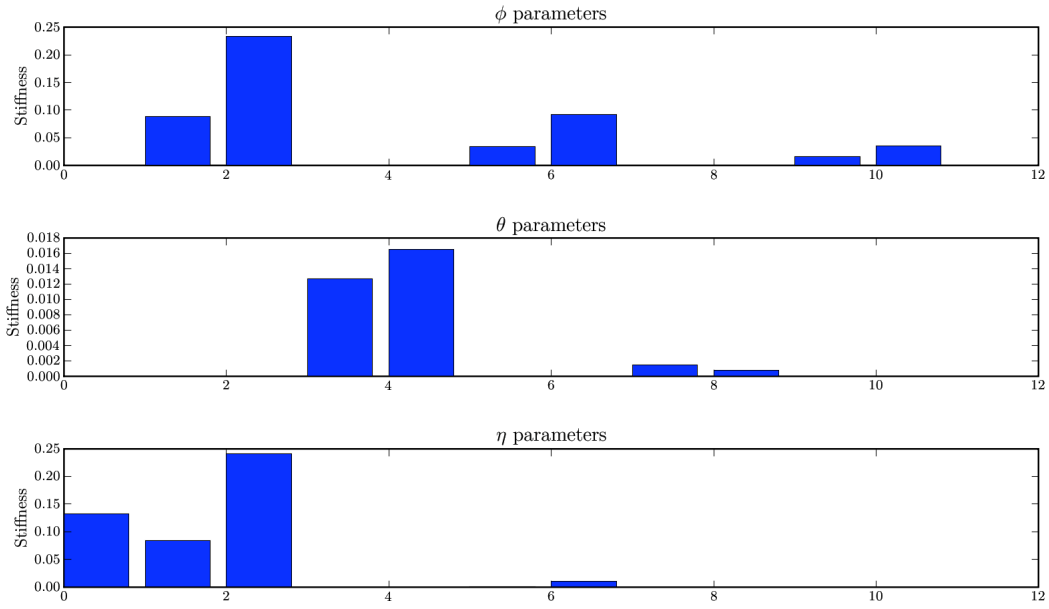

Figure 5.26: Parameter stiffnesses near the local optimum for ϕ, θ, and η. In each plot, the first bar is the offset value, followed by amplitude and phase for each respective Fourier mode. Note that for ϕ and η, most of the importance lies within the odd modes, whereas θ largely relies only on the even modes.

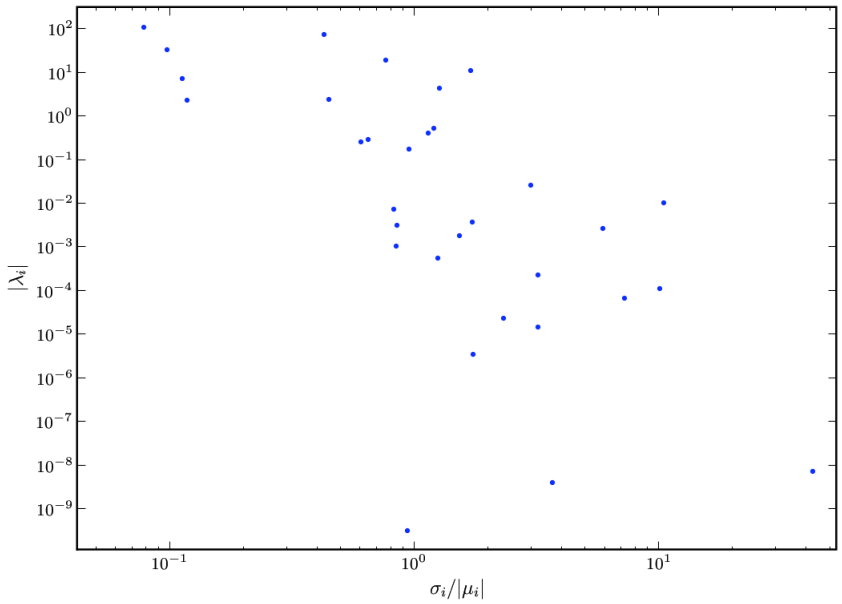

Figure 5.27: Eigenvalues vs standard deviations in the corresponding eigendirections

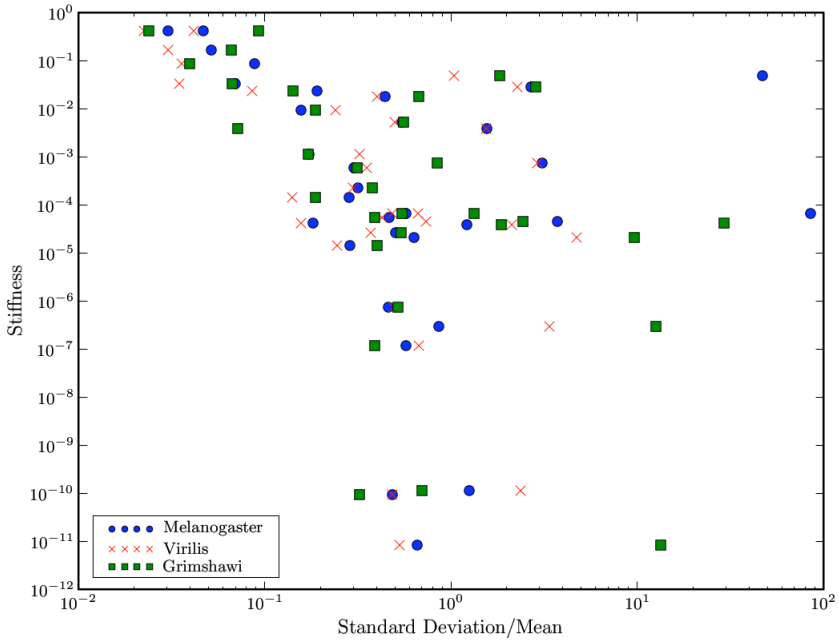

Figure 5.28: Parameter stiffness vs normalized standard deviation

cannot really say anything anyway. And even if the error is relatively small, we would like to be able to put error bars on the coefficients in order to make more rigorous claims. As we have obtained more data sets since performing this study, thanks largely to the HRMT tracking method (Chapter 3), one solution might be to take as our data points the average stroke from a longer series of wing beats. The error bars would then be related to the intra-individual variations and the variations we observe would be between different individuals in a population.

Secondly, as the landscape figures show, our data is not at the local optimum for many parameters. We would like to understand why this is the case, and if there is any physical or biological reason for this. It could be that our model is insufficient, leaving out effects or constraints. Or, perhaps, it could be that insects aren't really optimizing C like we have postulated, and maybe there is some other landscape which better describes the data. We could investigate this

by creating a metric that measures the distance of a stroke from a somehow optimal stroke, and compare this distance for different definitions of optimality (i.e. power per vertical force, or vertical force divided by drag, or smoothness of force production, or maximal vertical force production, all of which have been used in the literature), and see which definition can best explain the observed wing strokes.

Finally, we would like some way to perform a Hessian-style analysis like that used here, but at locations away from a local optimum. Near a local optimum, we have the property that the gradient is zero, so all information immediately near the basin (assuming appropriate smoothness, well-behavedness, etc.) is given by the Hessian. As one moves further away, however, this approximation starts to blur out, and the world becomes more complicated.

All this being said, though, the project remains an interesting one because it makes an attempt (if a flailing one) to quantify variations within a population and to attribute those variations to some identifiable metric. We make a prediction about the measured diversity within a population, which should have no bearing on the particular parameterization used to describe it. And as evolution and natural selection thrive on diversity and variation, characterizing this type of behavior, even if only for a solitary system, would be an important insight. This is the promise of the line of research; we just need the machinery to catch up with it.

5.6 Summary

In this chapter, the optimal and sub-optimal basins of the fruit fly model of Chapter 2 have been analysed via the Hessian eigen-direction analysis of [36–39]. The eigenvalues of the basins generally span 2-4 orders of magnitude

continuously, implying that this model of only a few parameters is sloppy near its optima. The stiffness of each of the parameters was quantified and it was found that the flight efficiency was relatively insensitive to the degrees of freedom related to wing rotation. Also, we have found many of the local optima of our model and analyzed the basin structure near them and, to a certain extent, the energy barriers between them. Finally, we have explored how the topography of the fitness landscape informs our understanding of variations within a population. Although this last analysis has yet to yield definitive conclusions, it points in intriguing directions for future study.

CHAPTER 6

THE TRANSITION TO CHAOS IN FALLING PLATES

6.1 Introduction

In the previous chapters of this thesis, insect flight has been analyzed through the lens of quasi-steady modeling. In this context (as the term "quasi-steady" can mean many things), we refer to a model in which all flow is instantaneously developed, implying that all fluid forces acting on a wing are only functions of its morphology and current kinematics (positions, velocity, etc.), and not on any flow history – at least explicitly. More specifically, the two-dimensional falling-plate model introduced in [40] and elaborated upon in [41, 42] has been used as a fluid force model for insect wings. This comparison is plausible, as the plates share both morphological similarities (thin aspect ratio, relatively long third dimension) and reside in the same Reynolds number regime ($Re \approx 100$ – 1000).

As this model provides the undergirding for much of the work described in this document, it is of use to have an understanding of the dynamics it predicts (even if said dynamics are removed from wing musculature). For instance, observed insect wing motions might be the result of the passive interactions with the fluid. Additionally, one hypothesis is that animals might want to be near a transition or a bifurcation in their system dynamics, as it would allow for potentially greater control authority.

In this chapter, we apply some of the ideas of non-linear dynamics and mappings to this system. In particular, Lyapunov exponents and correlation dimensions of the attractor for various parameter values have been calculated, and the systems transition to chaos is analyzed via a Lorenz map prescribed for the

system.

6.2 Model

The model of fluid forces is a modified version of Krichoff's equations for the flow around a 2-D airfoil. It is a quasi-steady model, in that it depends only upon the kinematic variables of the plate at a given time, and it assumes contributions from lift, drag, and added mass terms. For simplicity, the plate is considered to have an elliptical cross-section. To eliminate cross-terms from the statement of the problem, the kinematic variables are given in terms of a co-moving, co-rotating coordinate system with respect to the plate (shown below in Figure 6.1) which has basis vectors $\{x, y\}$ and a rotational angle with respect to a horizontal orientation, θ. The equations describing the motion of the system are given by

$$(m + m_{11})\dot{v}_{x'} = (m + m_{22})\dot{\theta}v_{y'} - \rho_f \Gamma v_{y'} - \pi(\rho_s - \rho_f)abg\sin\theta - F^{\nu}_{x'} \tag{6.1}$$

$$(m + m_{22})\dot{v}_{y'} = -(m + m_{11})\dot{\theta}v_{x'} + \rho_f \Gamma v_{x'} - \pi(\rho_s - \rho_f)abg\cos\theta - F^{\nu}_{y'} \tag{6.2}$$

$$(I + I_a)\ddot{\theta} = (m_{11} - m_{22})v_{x'}v_{y'} - \tau^{\nu}, \tag{6.3}$$

where m is the mass of the plate, I is the plates moment of inertia, ρ_f and ρ_s are the densities of the fluid and the plate, respectively, a and b are the semi-major and semi-minor axes of the disk cross-section, g is the gravitational acceleration near the surface of the Earth, m_{11}, m_{22}, and I_a are added mass terms, $F^{\nu}_{x'}$, $F^{\nu}_{y'}$, and τ^{ν} are viscous drag terms, and Γ is the circulation around the plate. From the plates elliptical geometry, it is possible to extract m and I in terms of the other parameters, as well as calculate the added mass terms. Here, we have that $m = \pi\rho_s ab$ and $I = \frac{1}{4}\pi\rho_s ab(a^2 + b^2)$. From using the analysis of [116], the added

mass terms are found to be

$$m_{11} = \pi\rho_f b^2 \tag{6.4}$$

$$m_{22} = \pi\rho_f a^2 \tag{6.5}$$

and

$$I_a = \frac{1}{8}\pi\rho_f(a^2 - b^2)^2. \tag{6.6}$$

What remains is to specify the form of the circulation and of the viscous terms. For the circulation, a Kutta-Joukowski style form is used, with modifications to allow for stall effects at high angle of attack and for rotational lift.

$$\Gamma = 2C_R a^2\dot{\theta} - C_T a\sqrt{v_{x'}^2 + v_{y'}^2}\sin 2\alpha = 2C_R a^2\dot{\theta} - 2C_T a\frac{v_{x'}v_{y'}}{\sqrt{v_{x'}^2 + v_{y'}^2}}, \tag{6.7}$$

where C_R is the rotational lift coefficient, C_T is the translational lift coefficient, and α is the angle of attack (the angle between the velocity vector and the semi-major axis of the ellipse).

Finally, we need to specify the dissipative viscous terms. For the translational terms, a quadratic drag is used, yielding

$$\vec{F}^v = \rho_f a(A - B\cos 2\alpha)\sqrt{v_{x'}^2 + v_{y'}^2}\langle v_{x'}, v_{y'}\rangle \tag{6.8}$$

$$= \rho_f a\Big(A - B\frac{v_{x'}^2 - v_{y'}^2}{v_{x'}^2 + v_{y'}^2}\Big)\sqrt{v_{x'}^2 + v_{y'}^2}\langle v_{x'}, v_{y'}\rangle, \tag{6.9}$$

where A and B are drag coefficients. The viscous torque term is given by

$$\pi\rho_f a^4\Big(\frac{1}{\bar{T}}\mu_1 + \mu_2|\dot{\theta}|\Big)\dot{\theta} \tag{6.10}$$

where μ_1 and μ_2 are drag coefficients and $\bar{T}$ is the characteristic time scale of the system. The specific time scale will be described when making the equations non-dimensional.

Speaking of which, in the grand spirit of the analysis of ODEs, we now wish to non-dimensionalize the equations. We will assume that the semi-major axis

of the ellipse is our length scale, L, and that the velocity scale, U, is given by the terminal velocity of the plate when interacting with a quadratic drag. The time scale is just $\frac{U}{L}$. Hence, we have

$$L = a \tag{6.11}$$

$$U = \sqrt{\Big(\frac{\rho_s}{\rho_f} - 1\Big)gb}. \tag{6.12}$$

Non-dimensionalizing 6.1 according to these scales yields

$$(I^* + \beta^2)\dot{v}_{x'} = (I^* + 1)\dot{\theta}v_{y'} - \Gamma v_{y'} - \sin\theta - F^{\nu}_{x'} \tag{6.13}$$

$$(I^* + 1\dot{v}_{y'}) = -(I^* + \beta^2)\dot{\theta}v_{x'} + \Gamma v_{x'} - \cos\theta - F^{\nu}_{y'} \tag{6.14}$$

$$\frac{1}{4}\Big(I^*(1+\beta^2) + \frac{1}{2}(1-\beta^2)\Big)\ddot{\theta} = (\beta^2 - 1)v_{x'}v_{y'} - \tau^{\nu} \tag{6.15}$$

where β is the aspect ratio, $\frac{b}{a}$, and I^* is the dimensionless moment of inertia, $\frac{\rho_s b}{\rho_f a}$. In this form, we also have that

$$\Gamma = \frac{2}{\pi}\left(C_R\dot{\theta} - C_T\frac{v_{x'}v_{y'}}{\sqrt{v^2_{x'} + v^2_{y'}}}\right) \tag{6.16}$$

$$\vec{F}^{\nu} = \frac{1}{\pi}\left(A - B\frac{v^2_{x'} - v^2_{y'}}{v^2_{x'} + v^2_{y'}}\right)\sqrt{v^2_{x'} + v^2_{y'}}\langle v_{x'}, v_{y'}\rangle \tag{6.17}$$

and

$$\tau^{\nu} = (\mu_1 + \mu_2|\dot{\theta}|)\dot{\theta}. \tag{6.18}$$

The remainder of this paper will explore the dynamics of the non-dimensional system as I^* is altered. As done in [42] the other parameters will be set such that $\beta = .05$, $A = 1.4$, $B = 1.0$, $C_T = 1.2$, $C_R = \pi$, and $\mu_1 = \mu_2 = .2$.

6.3 Possible Motions

It is easiest to refer to this system in terms of the qualitative types of motion which the plate can undergo. The complexity of the motion is heavily tied to

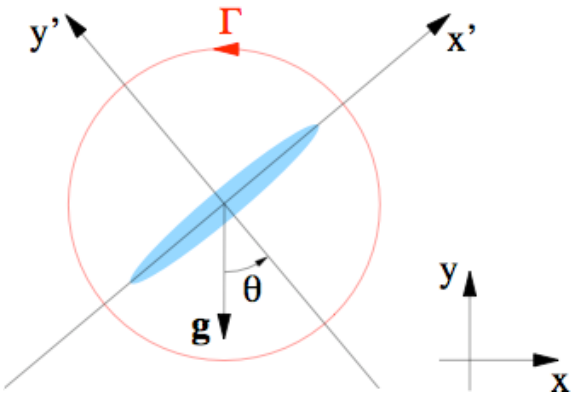

Figure 6.1: Plate coordinate system

the extent of the interactions between the plate and the fluid. I^* is the ratio of the moment of inertia of the falling disk and the induced moment of inertia of the fluid, so it is a good measure of these interactions. Hence, by dimensional analysis alone, one would guess that interesting dynamics would occur near $I^* = 1$, as this is where the interplay between the two objects in the system is the largest (even though only the plate's motion is explicitly modeled here). This turns out to be what happens. Also important is the fact that qualitative long-term motion of the plate is independent to the initial conditions by which the plate was dropped [41].

At low values of I^* (less than about 1.22, similar to a large sheet of paper falling in air), the plate exhibits fluttering motion, rocking back and forth periodically (Figure 6.2(a)). In the region $1.22 < I^* < 1.42$, the plate is able to generate enough angular momentum to make full rotations, and so it tumbles diagonally downward(Figure 6.2(b)). There is also a logarithmic divergence of the period of oscillation near $I^* = 1.22$ in the transition region between fluttering and tumbling, the signature of a homoclinic bifurcation [41]. From the end of the tumbling region upwards to approximately $I^* = 3$, a chaotic regime exhibiting characteristics of both fluttering and tumbling exists (Figure 6.2(c)). Both of

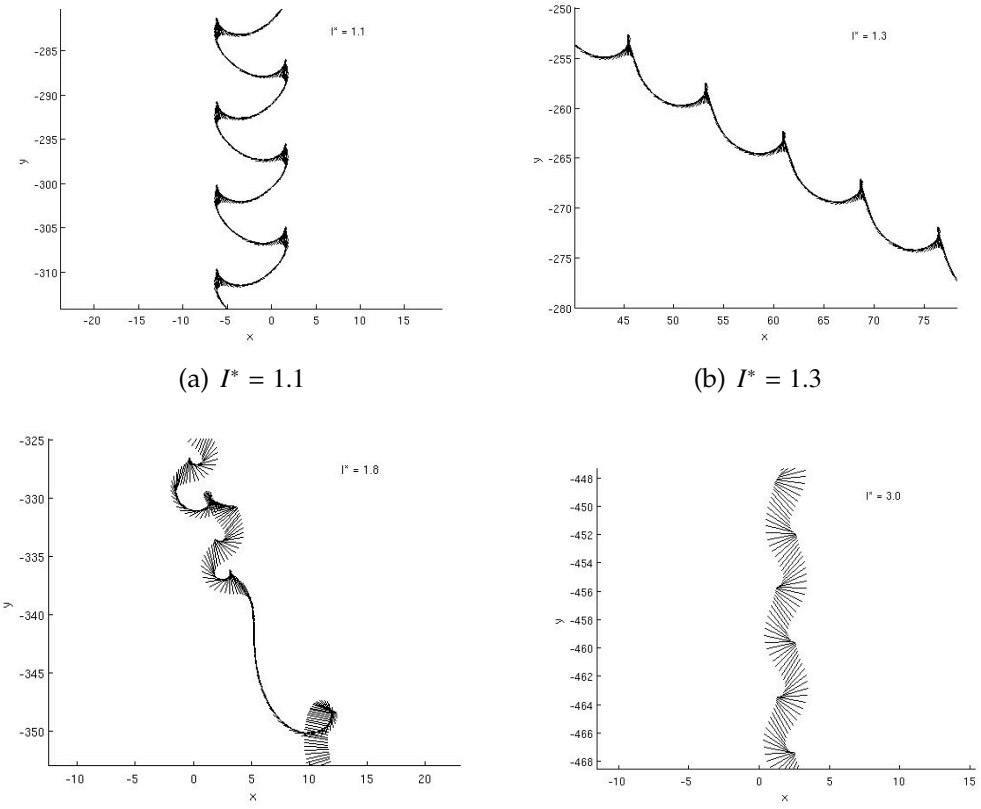

(a) $I^* = 1.1$ (b) $I^* = 1.3$

(c) $I^* = 1.8$ (d) $I^* = 3.0$

Figure 6.2: Sample model trajectories

the previous two regimes discussed can be thought of business cards of various widths falling in air. Whether or not this motion actually is chaotic will be discussed later. Finally, for $I^* > 3$, the fluids impact on the plate becomes minimal, resulting in small amplitude fluttering (Figure 6.2(d)).

This chapter will take particular interest in the transition into the regime of more complicated trajectories beginning near $I^* = 1.42$ and the transition back to small-amplitude fluttering near $I^* = 2.84$.

6.4 Lyapunov Exponents

The first analysis of these equations is to measure the largest Lyapunov exponent for the system as a function of I^*. This is achieved via the method described in [117,118]. First, the linear variational equations for the four variables salient to the systems dynamics (v_x, v_y, θ and $\dot{\theta}$) are calculated, giving an equation of the form

$$\begin{pmatrix} \delta\dot{v}_{x'} \\ \delta\dot{v}_{y'} \\ \delta\dot{\theta} \\ \delta\dot{\omega} \end{pmatrix} = A \begin{pmatrix} \delta v_{x'} \\ \delta v_{y'} \\ \delta\theta \\ \delta\omega \end{pmatrix}. \tag{6.19}$$

Here, $\omega \equiv \dot{\theta}$ (since having nested dots over a variable is aesthetically unpleasing to a large degree) and A is a 4×4 matrix which depends on the morphological parameters of the plate and the kinematic variables. Performing this calculation, we can write the non-zero elements of A as follows:

$$\begin{aligned}
A_{11} &= \frac{2C_T v_{y'}^4 + 2v_{x'}^4(B-A) + 3v_{x'}^2 v_{y'}^2(B-A) - (A+B)v_{y'}^4}{\pi v^3 I^*} \\
A_{12} &= \frac{2C_T v_{x'} v_{y'}(v_{x'}^2 + v^2) - Av^2 + B(v^2 + 2v_{x'}^2)v_{x'}v_{y'} + v^3(\pi I^* + \pi - 2C_R)\omega}{\pi v^3 I^*} \\
A_{13} &= -\frac{\cos\theta}{I^*} \\
A_{14} &= \Big(1 + \frac{1}{I^*} - \frac{2C_R}{\pi I^*}\Big)v_{y'} \\
A_{21} &= \frac{-2C_T v_{x'} v_{y'}(v^2 + v_{y'}^2) - (Av^2 + B(v^2 + 2v_{x'}^2))v_{x'}v_{y'} + v^3(\pi I^* + \pi - 2C_R)\omega}{\pi v^3(I^* + 1)} \\
A_{22} &= \frac{v_{x'}^4(B-A) - 3v_{x'}^2 v_{y'}^2(A+B) - 2v_{y'}^4(A+B) - 2C_T v_{x'}^4}{\pi v^3(I* + 1)} \\
A_{23} &= \frac{\sin\theta}{I^* + 1} \\
A_{24} &= \frac{1}{I^* + 1}\Big(\frac{2C_R}{\pi} - I^*\Big)v_{x'}
\end{aligned}$$

$$
\begin{aligned}
A_{34} &= 1 \\
A_{41} &= \frac{-8}{2I^* + 1} v_{y'} \\
A_{42} &= \frac{-8}{2I^* + 1} v_{x'} \\
A_{44} &= \frac{-8}{2I^* + 1} (\mu_1 + 2\mu_2 |\omega|)
\end{aligned}
$$

where $v \equiv \sqrt{v_{x'}^2 + v_{y'}^2}$.

Given these equations, after running the system for some transient time to get onto the attractor (usually 500-1000 time steps), a trajectory is chosen with its initial condition being the final state of the transient calculation and

$$\delta(0) = \sqrt{\delta v_{x'}(0)^2 + \delta v_{y'}(0)^2 + \delta\theta(0)^2 + \delta\dot{\theta}(0)^2} = 1 \tag{6.20}$$

with the direction of the initial condition of the four variational variables being chosen at random. The variational equations are then run for a time t. $\delta(t)$ is then measured and recorded in the same manner as $\delta(0)$. The initial conditions for the variational variables for the next time step, also of length t, are then given by taking the values $\delta v_{x'}$, etc., and then normalizing them by $\delta(t)$ (the initial conditions for the kinematic variables are simply given by their values at the end of the previous time step. This process is then continued for an arbitrary number of time steps, all of length t. The largest Lyapunov exponent, λ, is then calculated by

$$\lambda = \frac{1}{N} \sum_{i-1}^{N} \frac{1}{t} \log \frac{\delta(it)}{\delta(t(i-1))}. \tag{6.21}$$

This process was then repeated 10-20 times per I^*, each with a randomly chosen different initial direction of δ. Then, λ was found for many different values of I^* between .5 and 3.5, resulting in Figure 6.3 below.

As expected, the Lyapunov exponent is within error of zero in the regions in which simple periodic behavior occurs (fluttering, tumbling, low-amplitude fluttering), implying that at most, it takes a very long time for closely separated

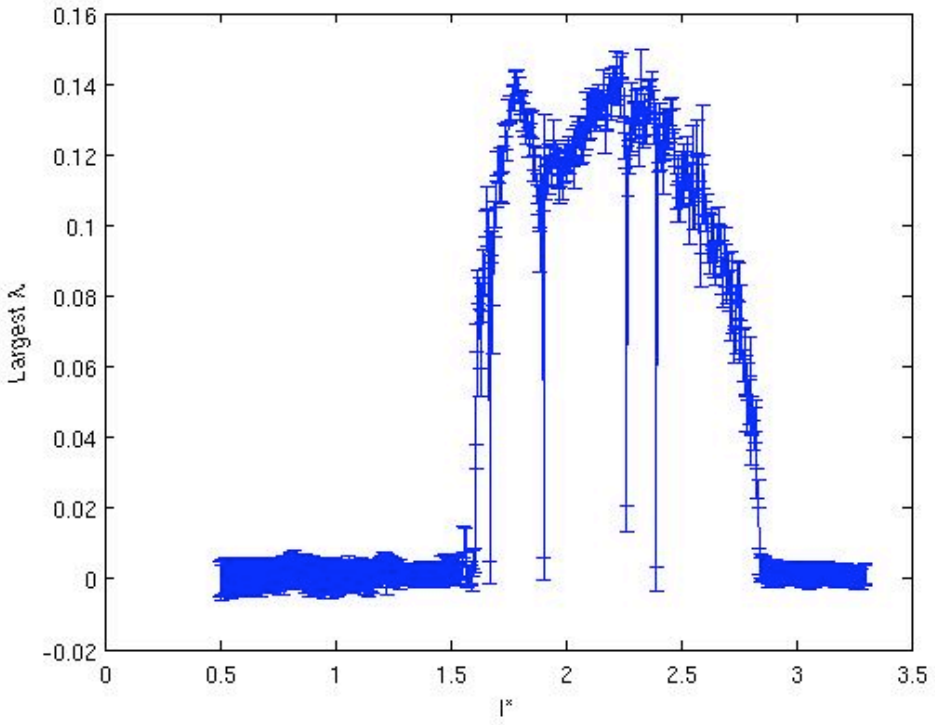

Figure 6.3: Largest Lyapunov exponent vs. I^*

initial conditions to diverge (if they do at all). The fact that λ becomes positive, though, during $1.6 < I^* < 2.84$ implies that the complicated trajectories observed here actually are chaotic. The drops down to near zero during the large λ region correspond to periodic windows (Figure 6.4), the nature of which will be explained in more detail in following sections. Interesting as well is the fact that there appears to be two separate peaks involved in the Lyapunov exponent rise. This suggests that two separate physical processes are occurring to engender the chaotic regime. Looking at trajectories from regions in which different processes appear to be occurring (Figure 6.5), there appears to be no obvious qualitative difference between the two regions, other than the fact that tumbling is more common in the first. Again, this will be discussed further in detail later.

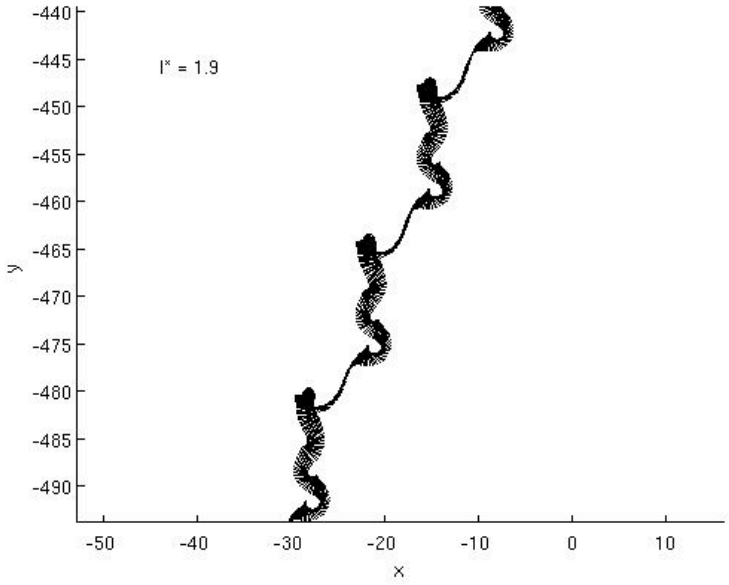

Figure 6.4: An example of a periodic trajectory in the midst of the chaotic region ($I^* = 1.9$)

6.5 The Lorenz Map

The next piece of analysis was to transform the system in hopes of observing phenomena that might better shed light on the systems dynamics. This was achieved via the map developed by [119] in Lorenz's famous paper attempting to understand atmospheric dynamics. In this method, we can take advantage of the fact that there is a bounded oscillation in the vertical velocity (v_y) of the plate after an initial transient period (Figure 6.6). In this case, the map is given by taking the value of the four state variables ($\langle v_x, v_y, \theta, \dot{\theta} \rangle$) whenever vy is at a maximum. Note that the velocity values are in the unprimed frame, as these oscillations are not seen when looking at velocities in the primed frame. Although and are recorded at each time step, this paper looks primarily at the 1-D

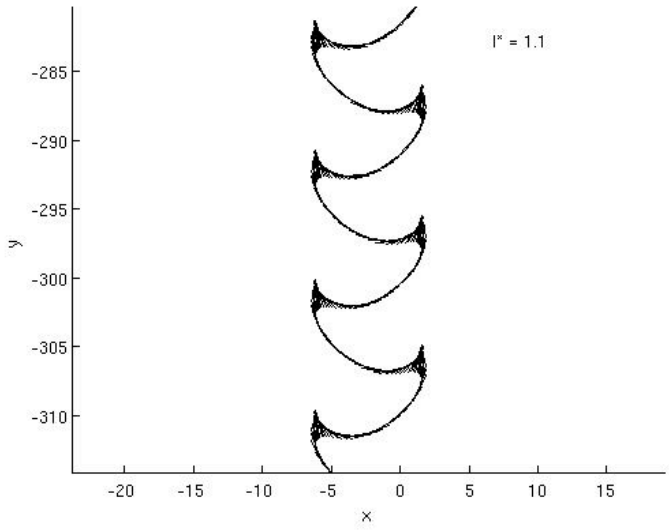

(a) $I^* = 1.75$

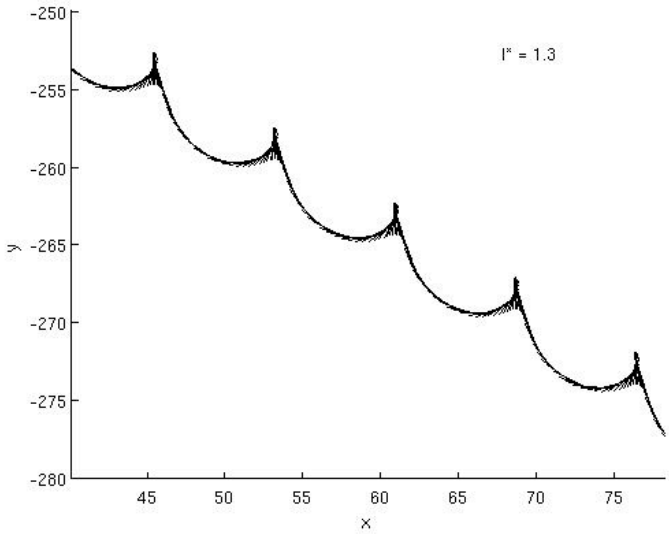

(b) $I^* = 2.5$

Figure 6.5: Two chaotic trajectories

iterations of v_y and the 2-D map resulting from $|v_x|$ and v_y (the absolute value is necessary for the x-coordinate in order to make fluttering a period-1 solution, the motivation for which will be shown momentarily).

First, we will look at the results from the 2-D map as a function of I^* in order to understand the structure of the attractor. Shown below are plots of at the Lorenz map points for varying values of I^* (Figure 6.7). A movie of these attractors morphing with I^* can be obtained via request from the author.

During the regions before $I^* = 1.42$ in which simple fluttering and tumbling exist, there is only one dot in the attractor, implying that a periodic solution exists (if v_x is used instead of $|v_x|$ for the Lorenz map, the symmetry of the motion causes two points to exist for fluttering, which we would like to characterize as periodic). The number of points then becomes two near $I^* = 1.42$, and then four near $I^* = 1.5$ (there is also a small segment in which a period-8 cycle occurs near $I^* = 1.56$). This type of growth appears to suggest that the system follows a period doubling cascade into chaos. As it turns out, though, there appears to be another process occurring as well that complicates the system's transition to chaos (see next section). As I^* continues to increase past the region of period doubling and into the chaotic region, an attractor with several tendrils extending off of a line forms (as seen in the plots 2nd and 3rd from the end in Figure 6.7). Near $I^* = 2.84$, though, all of the points collapse down to the main backbone line, and after this, the attractor spontaneously collapses down to a single point, implying the onset of small-amplitude fluttering, as seen in Figure 6.2(d). So whats happening at this point? For values immediately smaller than $I^* = 2.84$, the trajectory of the plate is for the most part that of a small-amplitude flutterer. However, the amplitude variations are not yet stable, causing the occasional tumble to occur when the plate builds an excess of angular momentum

(Figure 6.8). This motion corresponds to the thick line of points seen in Figure 6.7(g). Hence, the transition from a 1-D-like attractor to a point occurs when the small-amplitude fluttering motion stabilizes. More will be said about this later.

The last piece of analysis done on the 2-D Lorenz map was to measure the correlation dimension of the attractor as a function of I^*. This was done using the method described in [120]. For points $\{\vec{x}\}_i$ in an attractor containing N points, $C(\epsilon)$ is defined such that

$$C(\epsilon, N) = \frac{2}{N(N-1)} \sum_{i=1}^{N} \sum_{j=i+1}^{N} \Theta\Big(\epsilon - \|\vec{x}_i - \vec{x}_j\|\Big), \tag{6.22}$$

where $\Theta(x)$ is the Heaviside step function. The correlation dimension is then defined as

$$d = \lim_{\epsilon \to 0} \lim_{N \to \infty} \frac{\partial}{\partial(\log \epsilon)} \log C(\epsilon, N). \tag{6.23}$$

Naturally, we expect that this value should be zero for areas of periodic solution which result in a Lorenz map of a point, and that $1 < d < 2$ for the chaotic region. Practically, this was calculated by finding the slope of a log-log plot of $C(\epsilon, N)$ for constant N and various values of ϵ. The results can be seen below in Figure 6.9. As expected, the average dimension was found to be zero in the regions of periodic motion, and then increased to a value a little larger than one in the chaotic region ($d \approx 1.19$). It then drops off to $d = 1$ near the transition to low-amplitude fluttering and proceeds to drop-off immediately to $d = 0$ after $I^* = 2.84$. This further confirms the collapse to a line and then a point at the chaos to small-amplitude fluttering transition.

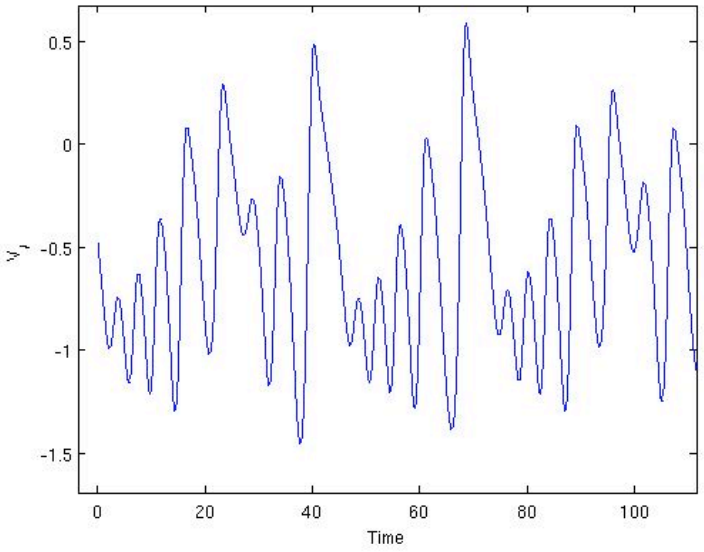

Figure 6.6: Vertical velocity ($v_{y'}$) vs. Time for $I^* = 2.2$

6.6 The Transition to Chaos in the 1-D Lorenz Map

We now look at the 1-D Lorenz map alluded to in the previous section in which each point is taken to be the value of v_y at each of its local maxima (Figure 6.6). The large-scale structure of which can be seen above in Figure 6.10. As seen in the 2-D map, the system starts out as a single stationary point for low I^* and then undergoes a series of period doublings before entering a more chaotic regime after about $I^* = 1.6$. This region then continues until about $I^* = 2.84$, at which point, the system enters the small-amplitude fluttering region.

Looking more closely at the period-doubling region (Figure 6.11), we can see many of the same features observed in the logistic map, but also some aspects that are strikingly different. In the first category, we see the same type of bold lines cutting through the bifurcation diagram. Also, there are several periodic windows within the chaotic regime. As seen in Figure 6.12, these windows match perfectly with the drops in the Lyapunov exponent discussed previously.

In the region where $1.56 < I^* < 1.59$, there is a period-2 solution (Figure 6.13)

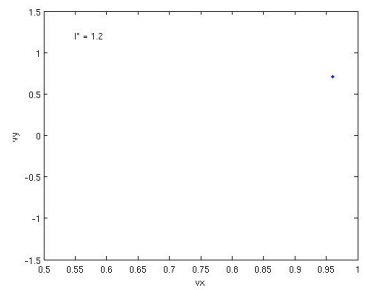

(a) $I^* = 1.2$

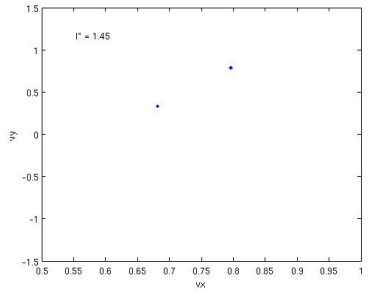

(b) $I^* = 1.45$

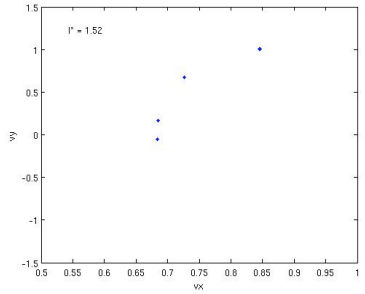

(c) $I^* = 1.52$

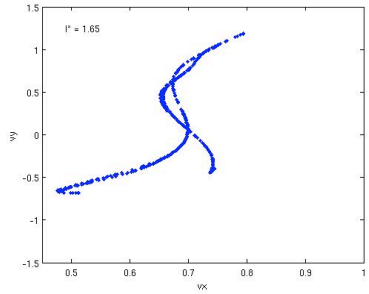

(d) $I^* = 1.65$

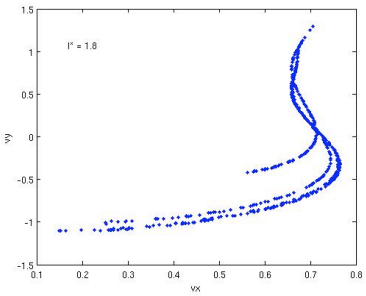

(e) $I^* = 1.8$

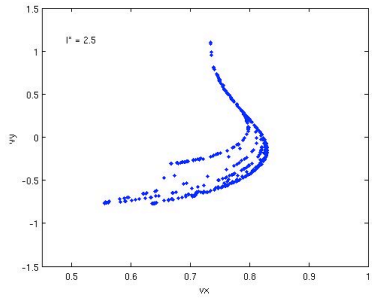

(f) $I^* = 2.5$

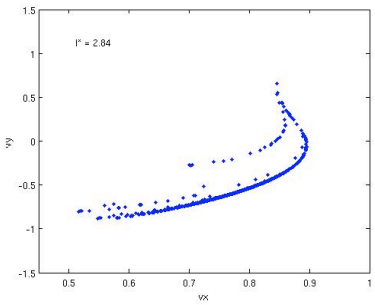

(g) $I^* = 2.84$

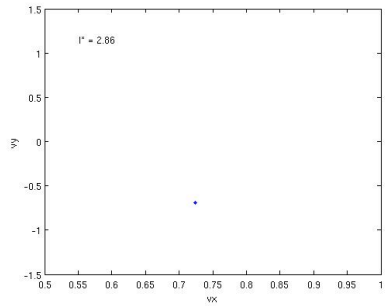

(h) $I^* = 2.86$

Figure 6.7: Attractor geometry for the Lorenz map vs. I^* for $1.2 < I^* < 2.86$

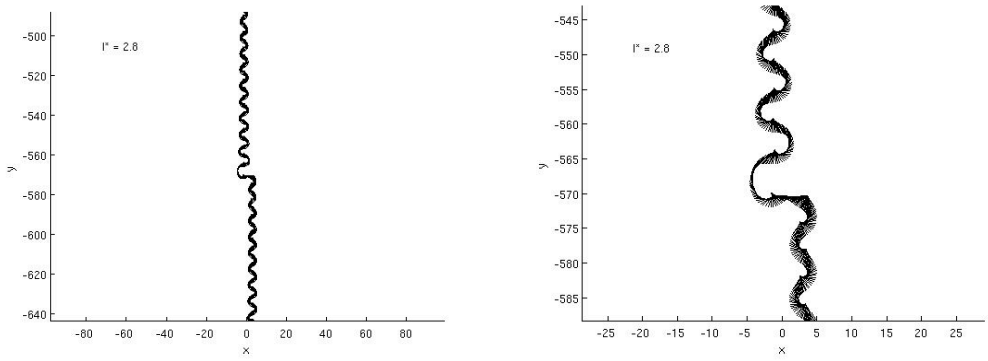

(a) (b)

Figure 6.8: Trajectory of Falling Plate at $I^* = 2.8$ (Far away and close up)

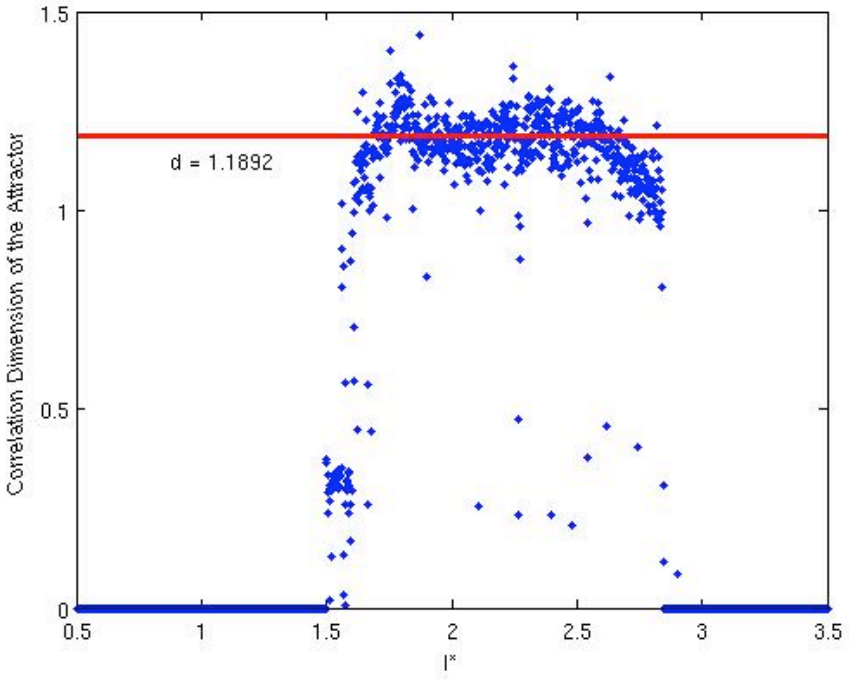

Figure 6.9: Correlation dimension of the attractor vs. I^*

that spontaneously appears (the stay dots in the region are the result of the transient time not being long enough as it takes longer for the trajectory to reach the attractor during the 2-cycle). It should be also noted, that λ is near zero in this region. Qualitatively, what happens here is that the trajectory goes from a period-4 oscillation that is a combination of fluttering and tumbling in to a more complicated, quasi-periodic-looking trajectory as the spontaneous appearance of the 2-period nears. The period-2 region then is when the plate is able to build-up enough angular momentum to tumble exactly once per half-cycle, but is unable to completely turn over again after that, resulting in a period-2 descent. The end of this region is caused by the ability of the plate to occasionally tumble a second time, resulting in a complicated trajectory similar to that seen immediately prior to the period-2 appearance. Despite valiant attempts, however, rigorous results regarding the (in)stability of this period-2 trajectory have currently eluded the author. A qualitative picture, however, can be seen in Figure 6.14 through the evolution of different trajectories through the described region.

While on the subject of non-rigorous results, there is an as-of-yet unexplained coincidence that appears to suggest the first peak seen in Figure 6.3. The emboldened lines seen in Figure 6.11 appear to all converge at approximately $I^* = 1.775$. As shown in Figure 6.15, this point almost exactly coincides with the first peak of λ. The reason for this remains a question for future research, as I have yet to find a compelling quantitative or qualitative explanation for this coincidence.

Lastly, we look at the transition from chaos to low-amplitude fluttering near $I^* = 2.84$. Looking at the zoom-in of the bifurcation diagram in Figure 6.16, it is possible to see what appears to be a condensing of points near the transition immediately before the transition to a small-amplitude fluttering scenario. We

can observe this more closely by looking at what happens to the shape of the probability measure of v_y as I^* approaches the transition. The measure, μ, was found by finding the Lorenz map values for the first 10,000 time steps (after an initial transient). The positions of v_y were then histogrammed and normalized to provide the plots shown in Figure 6.17. As seen there, the measure collapses down from a widely distributed measure at $I^* = 2.5$ to a delta function at $v_y \approx .69$, implying the creation of a stable period-1 orbit at the transition.

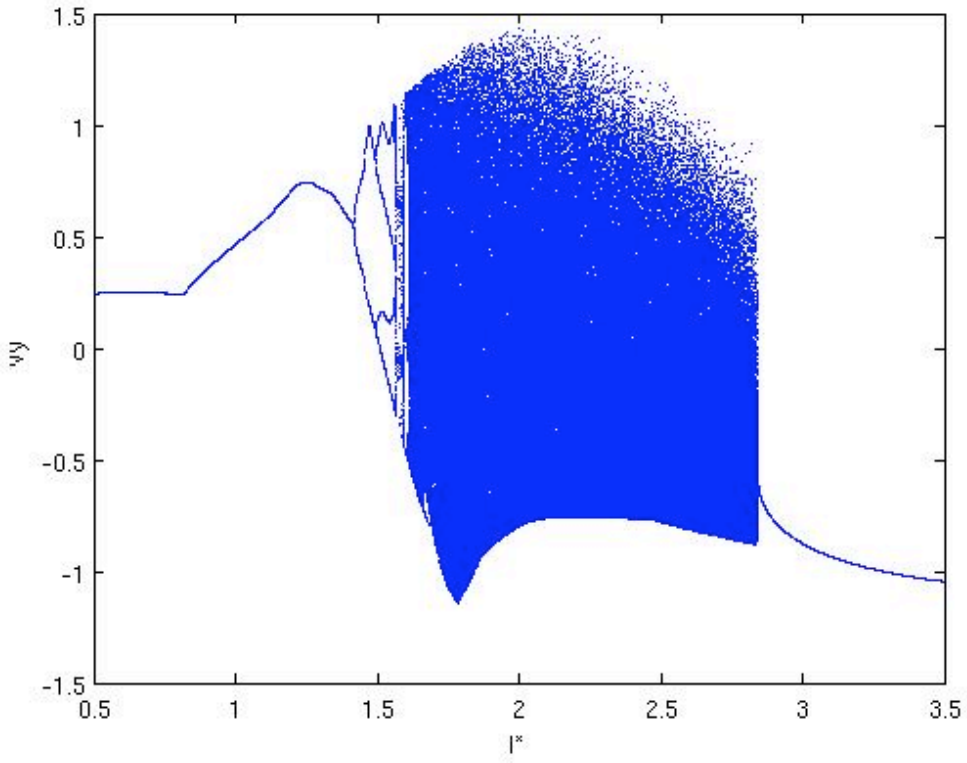

Figure 6.10: Large-scale results of the 1-D Lorenz map

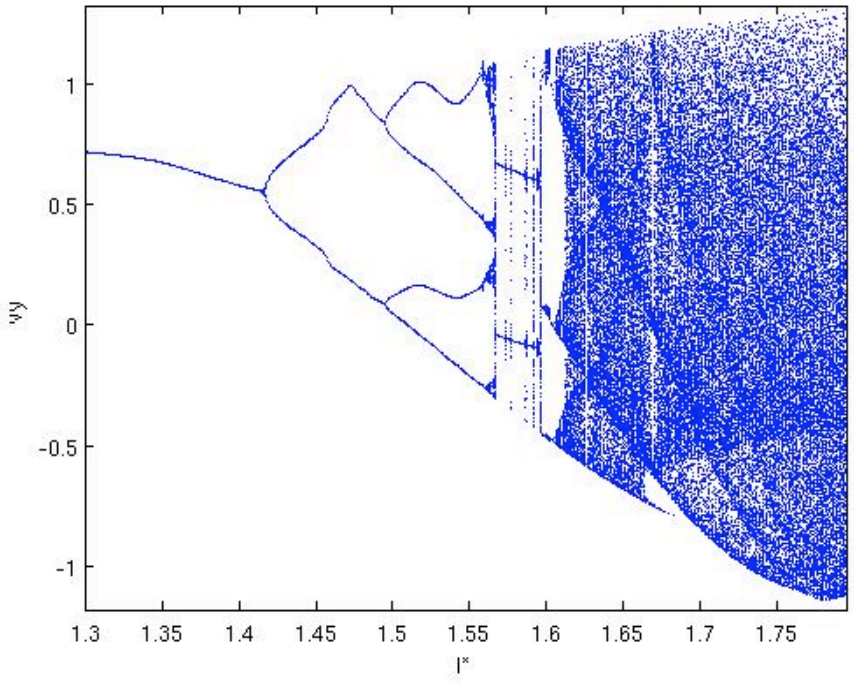

Figure 6.11: Zoom-in on the period doubling region of the Lorenz map

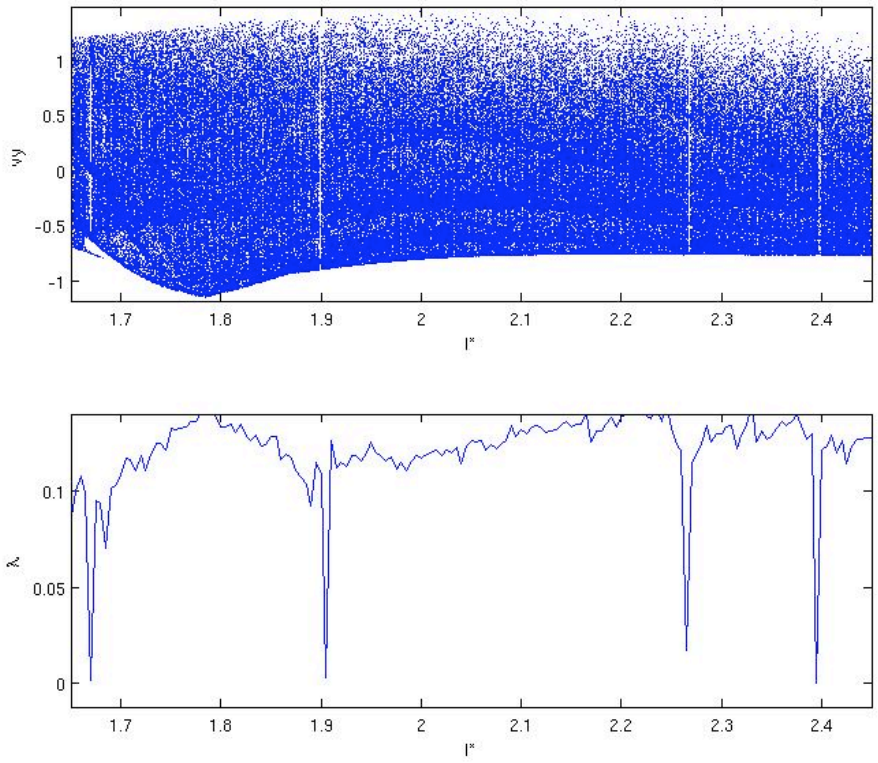

Figure 6.12: Location of periodic windows compared to drops in the Lyapunov exponent

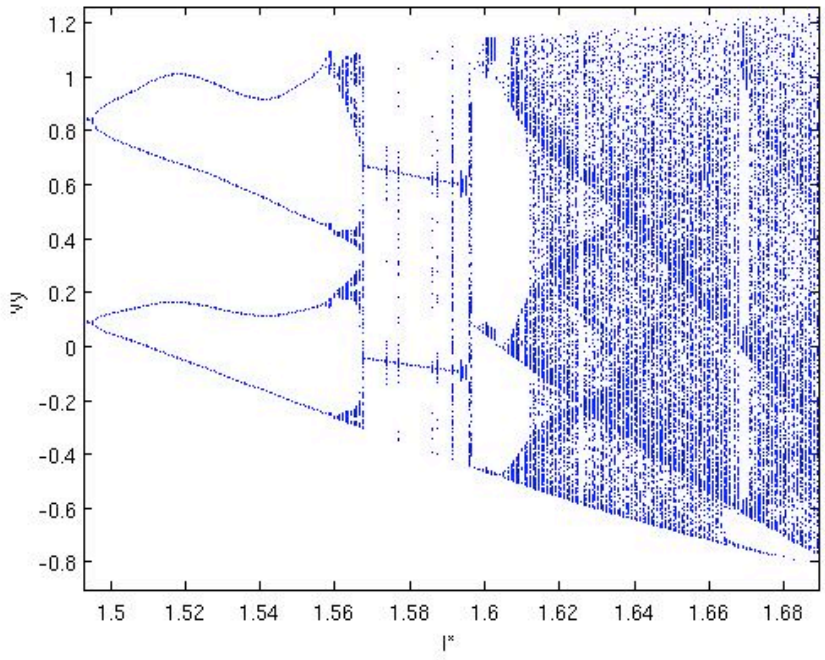

Figure 6.13: Zoom-in on the period-2 region

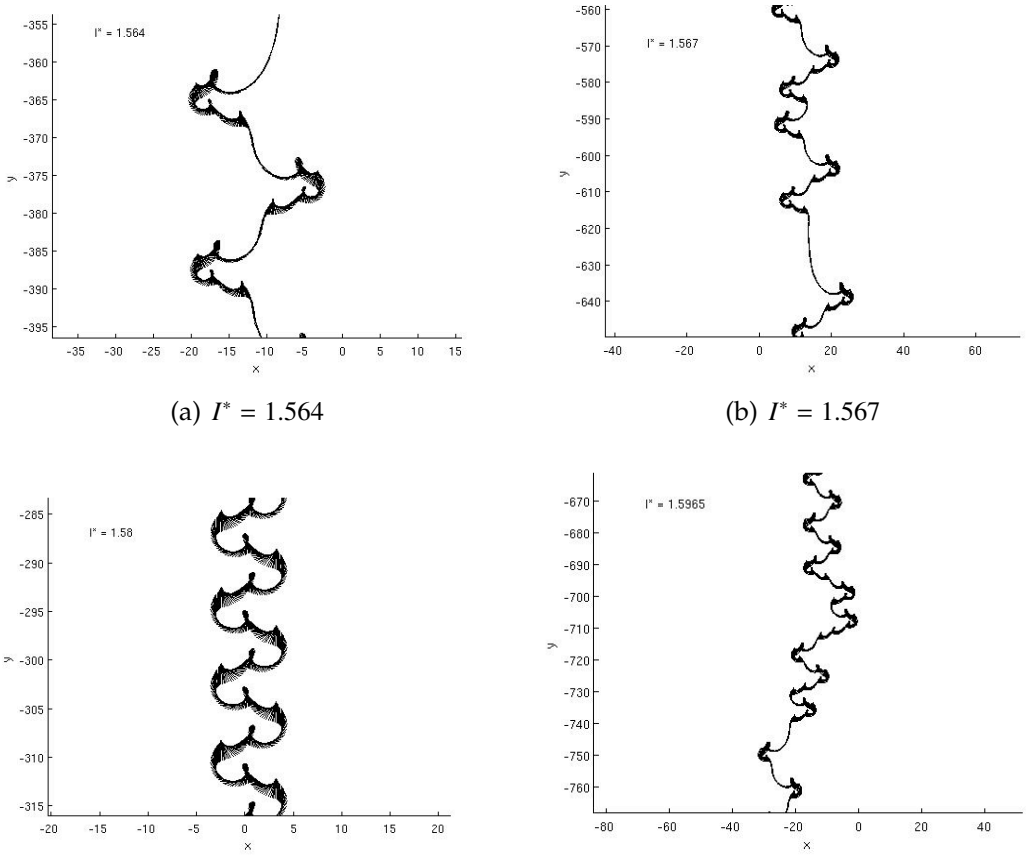

(a) $I^* = 1.564$ (b) $I^* = 1.567$

(c) $I^* = 1.58$ (d) $I^* = 1.5965$

Figure 6.14: Plate trajectories approaching, passing through, and leaving the period-2 region

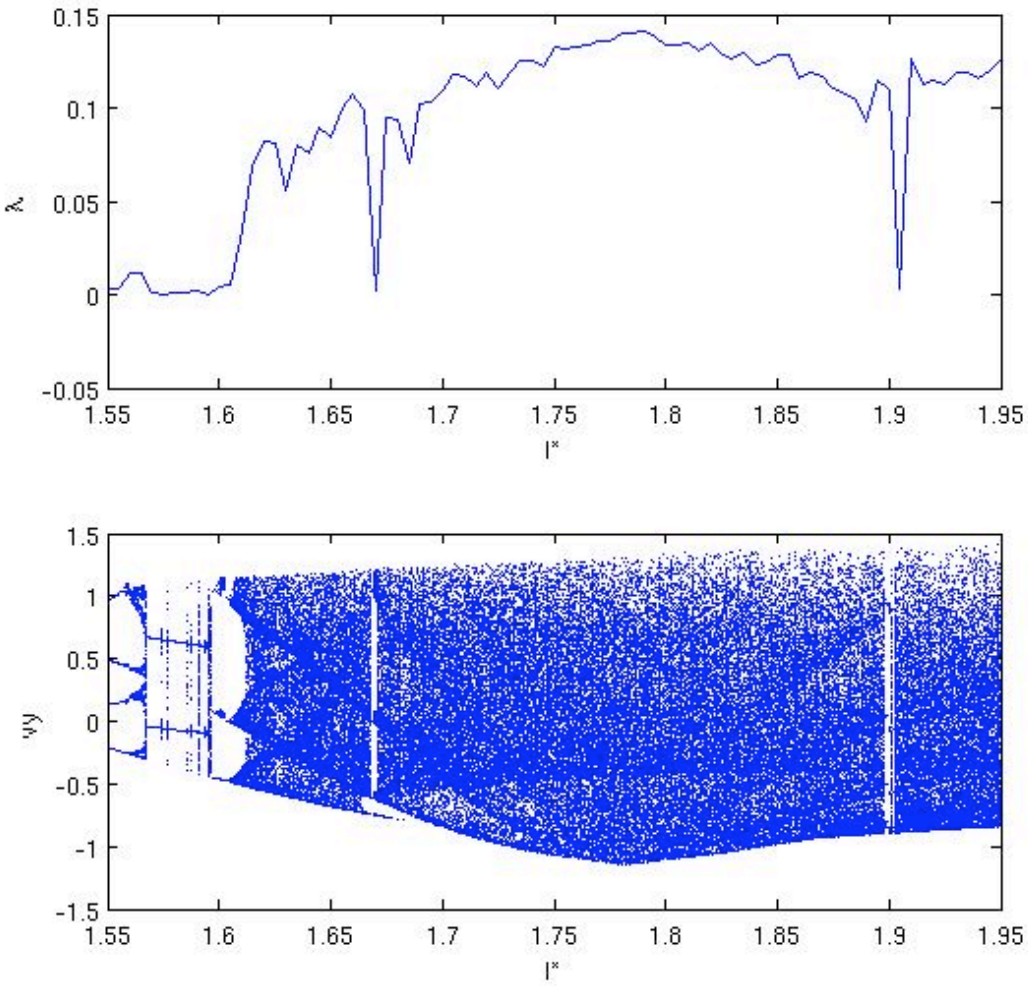

Figure 6.15: Coincidence of the first λ peak and the convergence of bold lines

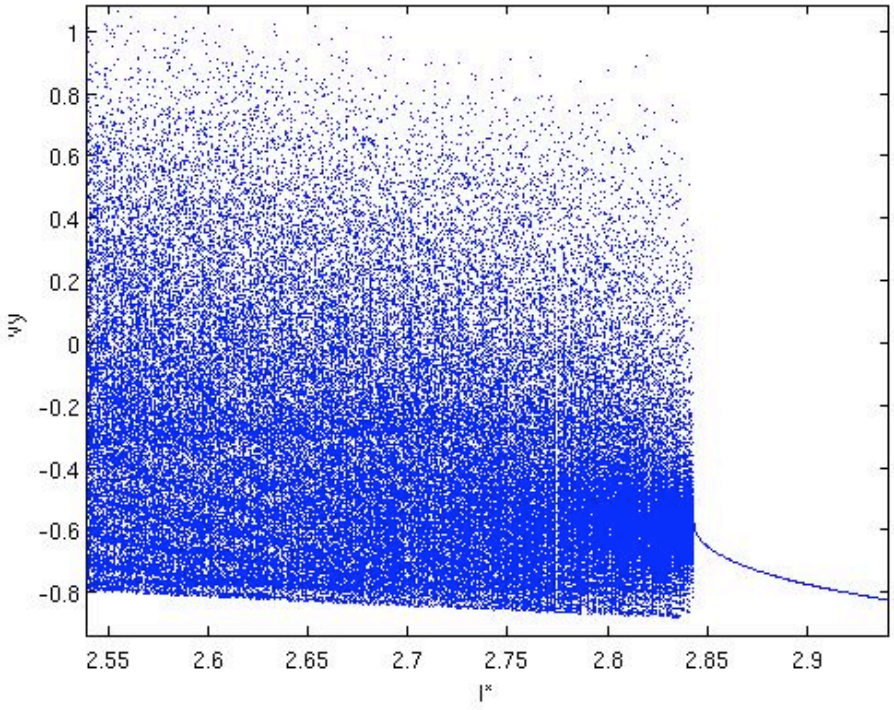

Figure 6.16: The transition from chaos to low-amplitude fluttering

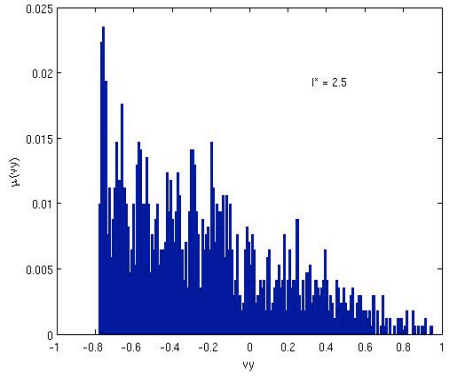

(a) $I^* = 2.5$

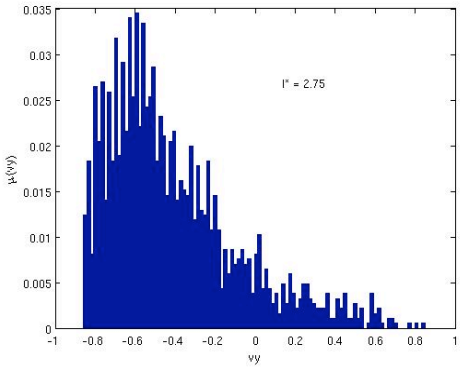

(b) $I^* = 2.75$

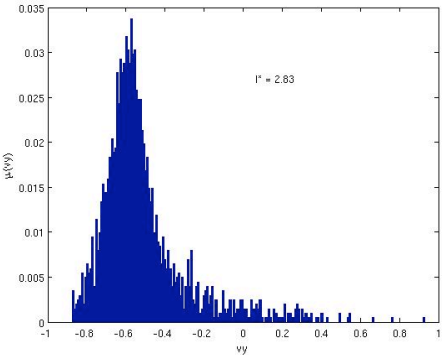

(c) $I^* = 2.83$

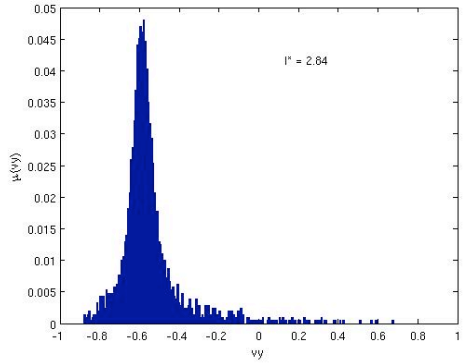

(d) $I^* = 2.84$

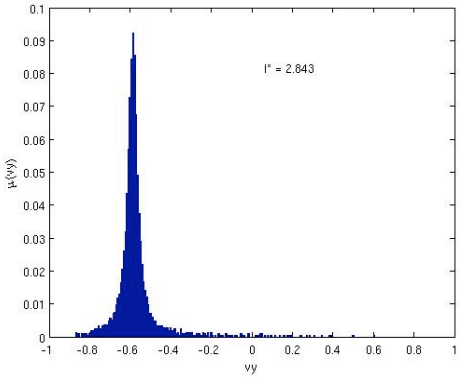

(e) $I^* = 2.843$

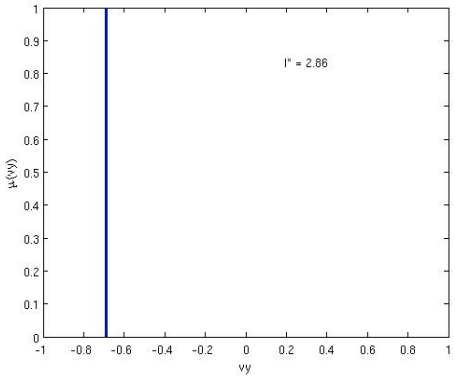

(f) $I^* = 2.86$

Figure 6.17: Measure of v_y near the transition to small-amplitude fluttering

6.7 Conclusions

Here, the dynamics of a two-dimensional falling rigid plate have been studied through measuring the Lyapunov exponents and looking at one and two dimensional Lorenz maps of the system for varying values of the non-dimensional moment of inertia, I*. The system was found to undergo a Feigenbaum-like period doubling transition into chaos beginning near $I^* = 1.42$ (although not enough branches were available to measure the Feigenbaum constant itself due to the numerical limitations of the ODE solver and the sudden appearance of a stable 2-cycle in the midst of the period doubling region). This chaotic region coincides with a large rise in the Lyapunov exponent of the system.

Further work in this area would benefit from more rigorous observations of the results shown numerically and/or qualitatively here. In particular, a proof of the existence and stability of a period-2 motion shown in Figure 6.13 and an understanding of the measure collapse illustrated in Figure 6.17 would be interesting problems. Any sort of explanation for the coincidence of the bold lines converging and the first Lyapunov peak (Figure 6.15) would be interesting. Numerically, it would also be of interest to look at measure variations systematically throughout the rest of the chaotic region besides its very end. Finally, [42] also observed that the dynamics of the plate change in qualitative ways when the viscous parameters, μ_1 and μ_2 are altered. Hence, it would be of value to see how the structure of the attractor and the bifurcation diagram changes with these variables.

CHAPTER 7

OPTIMIZING THE FLIGHT OF A TUMBLING AIRFOIL

7.1 Introduction

Insects are some of the world's most graceful, efficient, and varied locomotors – flying, darting, and hovering with an ease that has aroused the curiosity of physicists and the envy of aerospace and mechanical engineers. Despite this fact (or, more likely, because of it), the physical mechanisms behind their abilities are still poorly understood. This thesis focuses on unraveling some of these mechanisms. This includes attempting to understand the physical and evolutionary reasons explaining why insects fly in the manner which has been observed. Of particular interest is how rotation affects flight, as rotation of the airfoil with respect to the fluid flow is the primary difference between flapping flight and conventional airfoil theory. Rotation has also been shown to be important in explaining the dynamics of falling plates and paper [40–42]. As such, this paper will study the case of a two-dimensional flapper whose only means of actuation is via rotation about its center of mass. By attempting to optimize the trajectory of this object, it is possible to observe whether flight of some form is possible with only rotation, and if so, the nature of these flying trajectories.

7.2 Methods

7.2.1 Model Description

The model of fluid forces on a thin plate used here is similar to the one introduced in [40–42] to analyze the dynamics of a thin elliptical plate falling through a fluid, and by [106] to study optimal kinematics in insect flight. As the wings

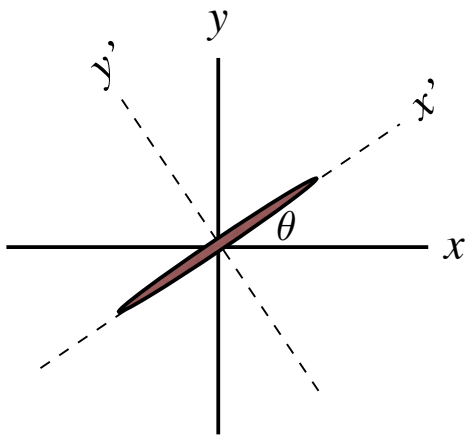

Figure 7.1: Model coordinates

we are interested in studying are of similar geometry and Reynolds number ($Re \sim 100$), the model should be applicable here as well. This is a quasi-steady model, meaning that all forces are only functions of the current kinematic state of the system (namely – position, velocity, and acceleration). Hence, there is no history dependence in the fluid flow. Although this does not allow for unsteady effects to explicitly enter into the equations of motion, the addition of a rotational lift term (Eqn. 7.4) has been shown to capture many of these effects [41]. For this paper, though, the model is appended to include the effect of the plate having to support an additional mass, M, located at the center of mass, along with its own mass. Also, a rotational actuator is assumed to exist at the center of mass. In fact, the parameter, M, can be viewed as the mass of this motor. The equations of motion are non-dimensionalized with the length scale being a, the semi-major axis of the ellipse, and with a velocity scale equal to the terminal velocity of the plate if it was resisted by quadratic drag.

In the co-rotating coordinate system shown in Figure 7.1, the non-dimensional equations of motion for the plate are as follows:

$$I^*(1+\gamma)\dot{v}_{x'} = (I^*(1+\gamma)+1)\dot{\theta}v_{y'} - \Gamma v_{y'} - \frac{1}{\pi}\sin\theta - F^{\nu}_{x'} \tag{7.1}$$

$$(I^*(1+\gamma)+1)\dot{v}_{y'} = -I^*(1+\gamma)\dot{\theta}v_{x'} + \Gamma v_{x'} - \frac{1}{\pi}\cos\theta - F^{\nu}_{y'} \tag{7.2}$$

$$\frac{1}{4}(I^* + \frac{1}{2})\ddot{\theta} = -v_{x'}v_{y'} - \tau^{\nu} + \tau^{applied} \tag{7.3}$$

Here, Γ is the circulation of the flow around the plate, given by

$$\Gamma = \frac{-2}{\pi}\left[C_T \frac{v_{x'}v_{y'}}{\sqrt{v_{x'}^2 + v_{y'}^2}} + C_R\dot{\theta}\right] \tag{7.4}$$

where C_T and C_R are non-dimensional constants. It is the term involving C_R which allows the creation of the lift from rotation – modeling several unsteady effects. For the studies here, $C_T = 1.2$ and $C_R = \pi$, as in [41]. $\vec{F^{\nu}}$ is the viscous drag, which is modeled as

$$\vec{F^{\nu}} = \frac{1}{\pi}\left[A - B\frac{v_{x'}^2 - v_{y'}^2}{v_{x'}^2 + v_{y'}^2}\right]\sqrt{v_{x'}^2 + v_{y'}^2}\begin{pmatrix} v_{x'} \\ v_{y'} \end{pmatrix} \tag{7.5}$$

where A and B are non-dimensional constants set to 1.4 and 1, respectively. τ^{ν} is the viscous torque, set such that

$$\tau^{\nu} = (\mu_1 + \mu_2|\dot{\theta}|)\dot{\theta} \tag{7.6}$$

where $\mu_1 = \mu_2 = .2$. I^* is the non-dimensional moment of inertia (given by $\frac{\rho_s b}{\rho_f a}$, where a and b are the semi-major and minor radii, respectively, of the ellipse, and ρ_f and ρ_s are the densities of the fluid and solid), and γ is the ratio between the supported mass and the wing mass. More precisely,

$$\gamma = \frac{M}{\pi\rho_s ab} \tag{7.7}$$

Although, one would ideally like to understand the properties of the flapper as a function of I^* and γ, time and computational limitations force this study

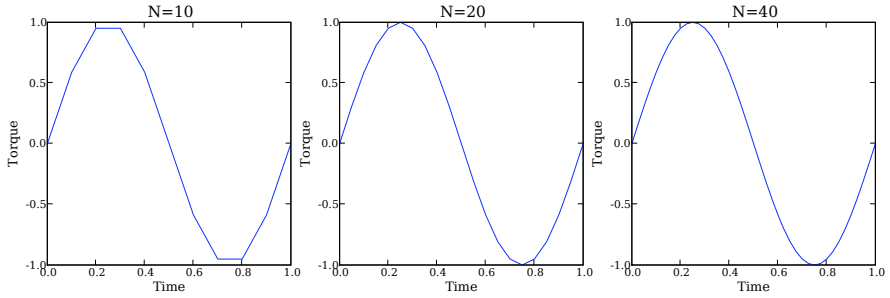

Figure 7.2: Applied torques for various values of N

to look exclusively at the case of $I^* = \gamma = 1$, which matches the morphological parameters of some larger insects such as hawkmoths and dragonflies. Finally, $\tau^{applied}$ is the applied torque by the actuator. It is this torque which will be optimized.

Also of interest is the mechanical power necessary to actuate a given motion. This power, P, is defined by

$$\frac{1}{T}\int_0^T |\dot{\theta}(t)\tau^{applied}(t)|dt \tag{7.8}$$

The absolute value is necessary because it is assumed that actuator cannot store energy.

7.2.2 Representation

For the optimizations to follow, the applied torque is assumed to be a periodic, piecewise-linear function with N evenly-spaced break points (see Figure 7.2). This assumption is inspired by studies of bipedal locomotion by [50]. Hence, any representation of the system requires at least $N + 1$ variables (one for each break point, plus a period giving the time scale). Here, two different representations are used – although it turns out that one clearly outperforms the other. For all simulations performed here, $N = 20$.

The first representation (hereto referred to as Representation 1) takes two absolute inputs: the torque at the beginning (and, accordingly, the end, due to periodicity) of each period and the length of the period. Each subsequent variable is a floating point number to be added to the previous value in order to obtain the torque at the next break point, with linear interpolation in between. The second representation (Representation 2) also specifies the torque at the beginning/end of the period, as well as the period length, but the intermediate variables are actually the absolute values of torque at the given point in the cycle, irrespective of its predecessors. Again, linear interpolation is used between the torque values at the break points. Pictorial examples of these representations can be seen in Figure 7.3.

The possible advantage of Representation 1 is that it preserves the shape of the waveform segment during crossover. Hence, once a good shape is found, it is likely to be kept in the population. The problem with this, however, is that shapes are less important that just having the values of the torques optimized, or that simply having a good shape will not lead to a better fitness unless the absolute values are optimal or near-optimal. This question of representation will be further examined in section 7.3.

7.2.3 Fitness and Function Evaluations

There are several useful definitions of what makes a good actuation pattern, but the most obvious ones are

1. The height the wing can rise to in a given amount of time (maximize)
2. The forward distance the wing can travel in a given amount of time (max-

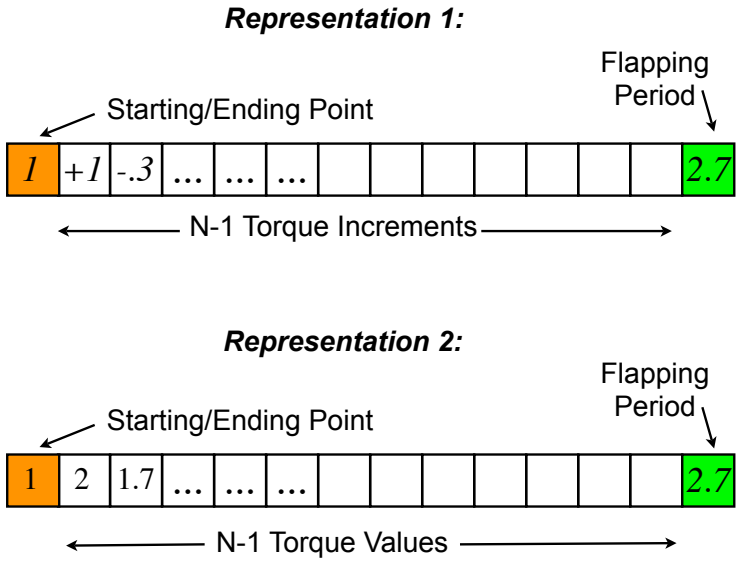

Figure 7.3: Representations used for the genetic algorithm

imize)

3. The amount of power required to actuate a particular trajectory (minimize)

To be precise, the fitness is defined as the time-averaged quantity in question after integrating Equations 7.1-7.3 from $t = 0$ to $t = 300$. This integration is implemented as a 4th-order Runga-Kutta numerical integration using the Gnu Scientific Library in C++ with absolute and relative tolerances of 10^{-6} (function evaluation time $\approx .25 - 2$ seconds, depending on the given torques, on a 3.0 GHz Intel Xenon processor). For all runs, the initial condition was set such that the flapper was started from rest, lying horizontally ($v_x = v_y = \theta = \dot{\theta} = 0$). Naturally, it is possible to optimize each of these traits individually (except for power, since that would lead to the trivial solution), or multiple ones via a Pareto-style multi-objective optimization. The methods for these optimizations are described in the following two sections.

7.2.4 Single-Objective Optimization

For the sake of understanding the system better for the more interesting multi-objective optimizations, we initially ran simulations that optimized only one objective, namely, the time-averaged vertical distance the flapper travels. For these simulations, two-point crossover is used, with $p_c = .6$. Mutation of values is allowed with a probability, p_m, of 10^{-3} per genome element. A value, X, is mutated to X' via

$$X' = X + M \cdot N(0,1) \tag{7.9}$$

where $N(0,1)$ is randomly drawn from a gaussian distribution with $\mu = 0$ and $\sigma = 1$, and $M = .25$.

Two different selection methods, rank-proportional with stochastic uniform sampling (SUS) and binary tournament, were tested, as well as the two different representations described in Section 7.2.2. For all runs, the population size, S, was set to 200. Values smaller than this tended to prematurely converge for all selection and variability operators tested. No elitism was used as the relatively large population size, combined with the low mutation rate mostly prevented good solutions from exiting the population. The population was initialized by randomly choosing N numbers $\in [-50, 50]$ for torque values/increments, and a number $\in (0, 50]$ for the stroke period. Although torque values were allowed to mutate out of this range, the period was restricted to be within the original range (a negative period is physically meaningless, and allowing larger periods dramatically increases the search time).

7.2.5 Multi-Objective Optimization

A Pareto-style algorithm is used to optimize the combinations of lift and power, as well as lift and forward flight[1]. The algorithm utilized is a variant of the NGSA-II algorithm ([121]), which is an elitist genetic algorithm that sorts not only by Pareto front, but also by its dissimilarity to other solutions in the population. More specifically, the algorithm ranks solutions first by their Pareto front (defined in the usual manner as the number of fronts needed to be removed in order for the solution to be non-dominated), but then by the normalized distance between the nearest neighbors on each side of the front in each dimension of fitness space. This aims to prevent the front from crowding in one particular area. The solutions with maximum fitness in each of the dimensions are always ranked at the top of their respective fronts.

After initializing the population to a size of S solutions, selection and variation occur in the same manner as in Section 7.2.4 until the population size doubles to a size of $2S$. Binary tournament selection is used (which should give a hint as to the findings from single-objective optimization). This doubled population is then sorted via the algorithm described in the previous paragraph. The top S individuals in this population survive to the next generation. Aditionally, to limit the search space, a lower bound of zero is set on the amount of lift generated by the solution (if the flapper is falling, the solution is not particularly interesting, no matter how little power is used). Various population sizes are tested.

[1] An algorithm that optimizes all three was also implemented, but no satisfactory results were achieved

7.3 Results

7.3.1 Single-Objective Optimization

As stated in the previous section, the single-objective optimization for vertical distance traveled per unit time is tested for both Representation 1 and Representation 2, as well as for two different types of selection, binary tournament and rank-proportional selection. The results (averaged over 5 trials each), can be seen in Figure 7.4. The optimal solution found in these simulations is shown in Figure 7.5. As Figure 7.4 displays, Representation 1 (where the genome components are relative values of torque) wound-up beating Representation 2 (components are the absolute values of torque). The apparent reason for this is that Representation 2 appears to be solving a "needle-in-the-haystack" style problem in that large changes quickly occur, followed by long plateaus. Additionally, the tournament selection outperformed the rank-based selection. Accordingly, for the simulations in Section 7.3.2, Representation 1 was used with a binary tournament selection (better solution taken with a probability of .75).

These optimization results were tested against the results from SNOPT, a atate-of-the-art commercial implementation of Sequential Quadratic Programming (SQP) optimization for which it is proven that all solutions it finds are locally minima [122]. This comparison was achieved by starting the SNOPT algorithm at a randomly selected initial condition in the same search space as that used by the GA. The program runs until it converges to an absolute and relative tolerance of 10^{-6} (the same as the ODE solver). Once this solution is found, a new initial condition is given to SNOPT, and the process continues until 200,000 total function evaluations are used. Comparing the results from this to the GA results (Representation 1, Tournament Selection) are striking. Over 5

runs of 200,000 evaluations, the GA converged to an average fitness of .561±.051. After 5 runs of the SNOPT algorithm described above, the average fitness was .141±.013. The best solutions obtained via the GA and SNOPT are seen in Figure 7.6 – with the GA clearly defeating the more conventional method. Although the reasons I can give for this discrepancy are largely speculative, it appears that for this particular problem, SNOPT gets easily hung-up on local minima. Hence, a decent a priori knowledge of certain aspects of function space is required.

All is not perfect, however. As will be seen in the next section, the GA was unable to find the best possible solutions, largely due to the population converging too quickly. This premature convergence is hinted at by the plots in Figure 7.4. Although some diversity-enhancement methods were attempted (i.e. occasionally adding in a externally evolved small sub-population, pruning via a distance metric, etc.), the best method was simply to use the multi-objective optimization described in the section to follow.

7.3.2 Multi-Objective Optimization

The initial test done was to observe the effect of population size on the success of the multi-objective optimization. In order to make a proper comparison, for each case, the GA was run until either the population converged (no new additions to the Pareto front in 20 generations) or 1 million function evaluations were achieved[2]. Figure 7.7 shows the final Pareto fronts for optimizing both rise and the inverse of the power consumed for these tests. What we see is that a population size of 1000 is clearly the best amongst the chosen run sizes. Hence,

[2]1 million function evaluations is the approximate number of function evaluations which can be performed over the course of 2 days

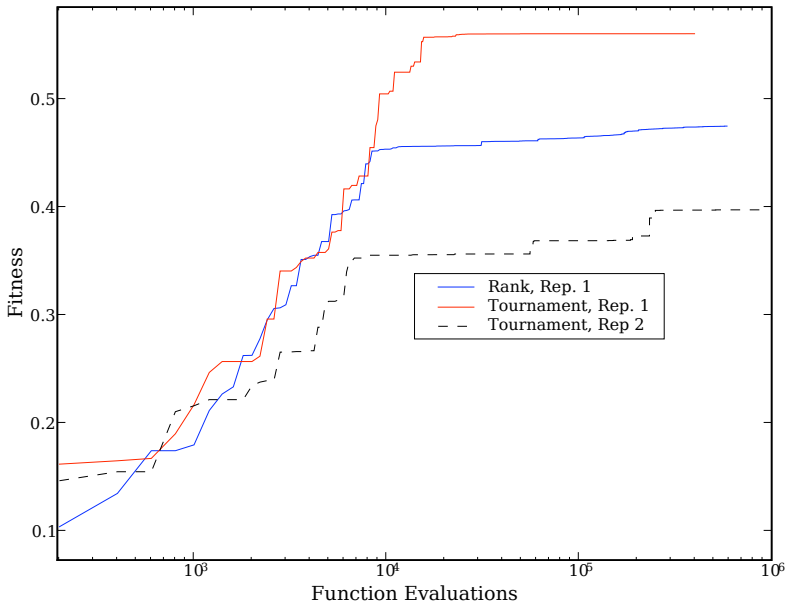

Figure 7.4: Fitnesses vs. function evaluations for rise optimization. All results are averaged over 5 runs, with fitness errorbars of ≈ ±.05

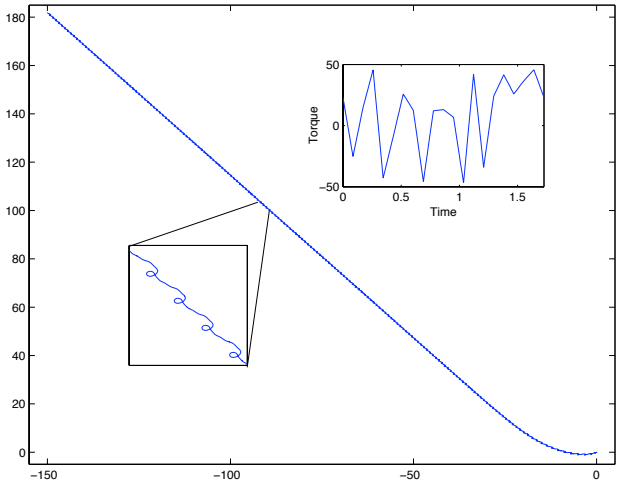

Figure 7.5: Trajectory and torques for optimal solution found via single-objective optimization (Rise = .690)

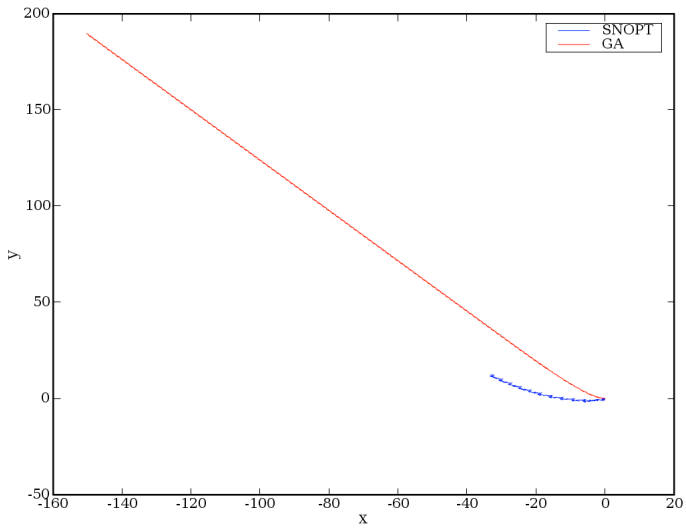

Figure 7.6: Comparison between GA and SNOPT after running from $t = 0$ to $t = 125$

it was this value that was used for the simulations to follow.

A reason for the large size necessary appears to be the existence of distinct strategies in the population. In other words, there is not a smooth transition between all nearest neighbors on the Pareto front, with discontinuous jumps between the various flapping strategies (an effect that will be observed in more detail later in this section). Therefore, the population is more likely to get hung-up on a local minimum that is able to take over the population if the number of individuals is small. Larger population sizes took significantly longer to converge, making their study impractical for the paper here. Other methods to alleviate this problem via diversity maintenance are possible, but the relatively costly objective function did not allow for a large degree of testing.

Results for the $S = 1000$ run at various time-steps are seen in Figure 7.8. As shown in the figure, the Pareto fronts gradually grow outward until finally converging after ~ 1000 generations. Once the front reaches its convergence point, new points with similar strategies grow outwards until creating an ergodic-appearing set of points displaying the limits of the particular strategy. This

is the reason for the separated clusters of points which lie upon the final front. This type of behavior (as well as the front itself), was seen in each of 5 runs with $S = 1000$. Also, note that the best solution in terms of optimizing only rise (top-left on the front), is significantly better than the fitness of the best solution found via single-objective optimization (Figure 7.5), which only had a fitness of .69, compared to the solution here, which has a rise value of .91 (Figure 7.9). Three solutions along the front are shown in Figures 7.9 - 7.11.

Finally, the results from optimizing both forward and vertical distance traveled are shown in Figure 7.12. The solutions were all of the same general type (see Figure 7.13), allowing for an ergodic-looking Pareto front, especially when compare to Figure 7.8. All solutions on the front display this sort of "reverse-tumbling" style behavior. In fact, five separate simulations all reached this identical front. While in itself, this would be a good result, as it means that the algorithm in repeatable and consistent, comparison to Figure 7.8 shows that this GA does not find the solution with optimal vertical displacement. Several attempts to expand out the front to these more "lift-like" solutions via diversity maintenance (in particular: pruning via a distance metric and introduction of a newly-evolved subpopulation at regular intervals) failed, all resulting in the same final front seen in Figure 7.12.

7.4 Conclusions and Future Work

In this chapter, it has been shown that a wing can generate sufficient lift to displace itself vertically via only rotational actuation. In addition, optimal (or minimally, very good) solutions have been found in terms of power consumption, lift production, and thrust production. This was achieved via both a single-

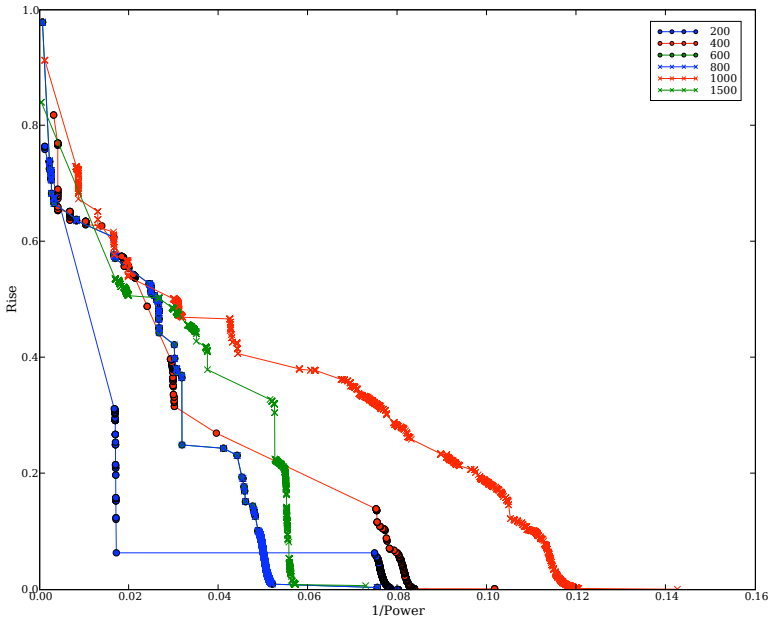

Figure 7.7: Performance of pareto optimization vs. population size

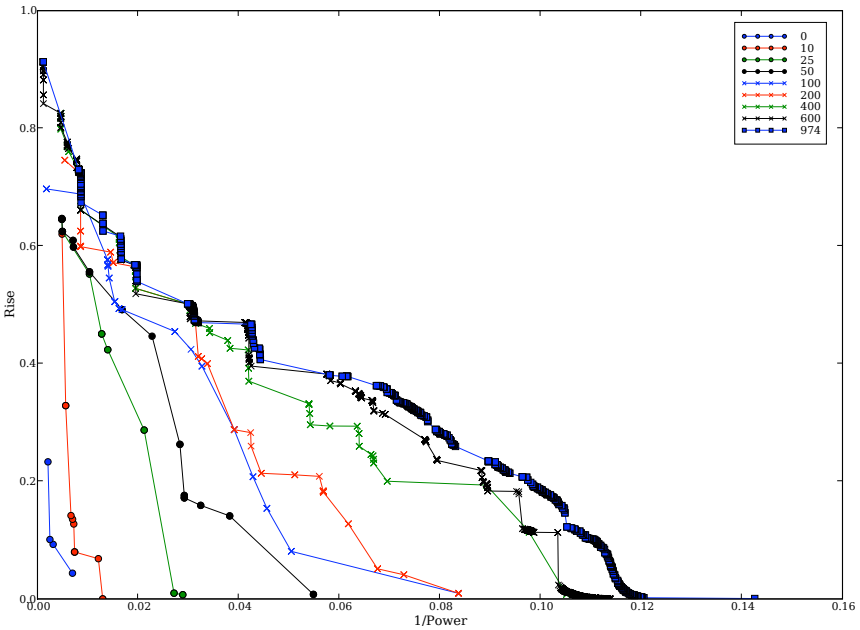

Figure 7.8: Performance of rise-power pareto optimization for $S = 1000$

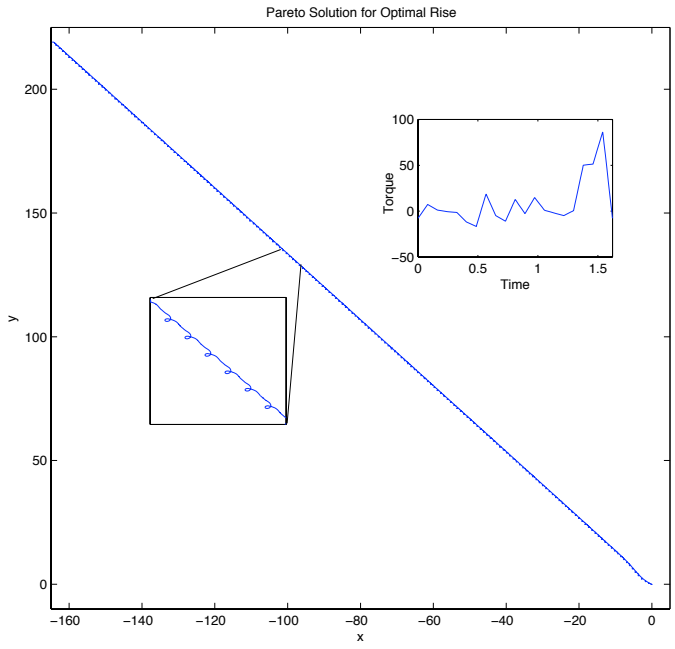

Figure 7.9: Optimal rise

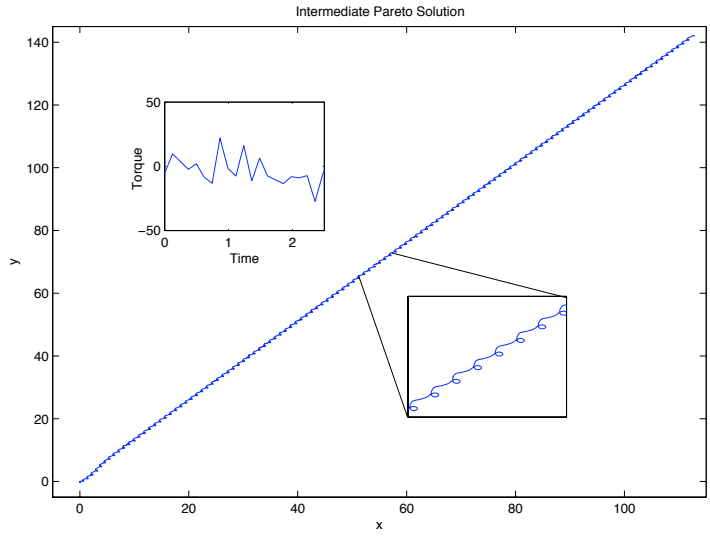

Figure 7.10: Intermediate

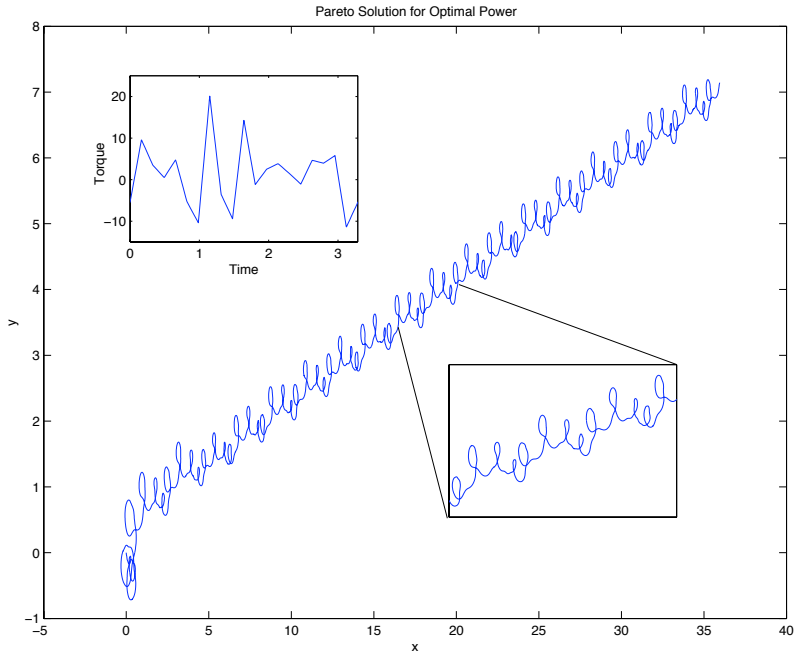

Figure 7.11: Optimal power

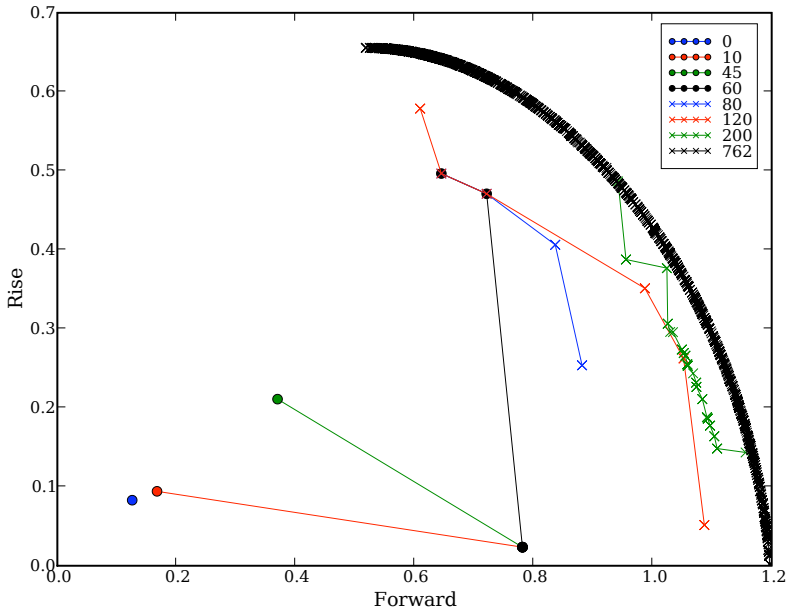

Figure 7.12: Performance of rise-forward pareto optimization

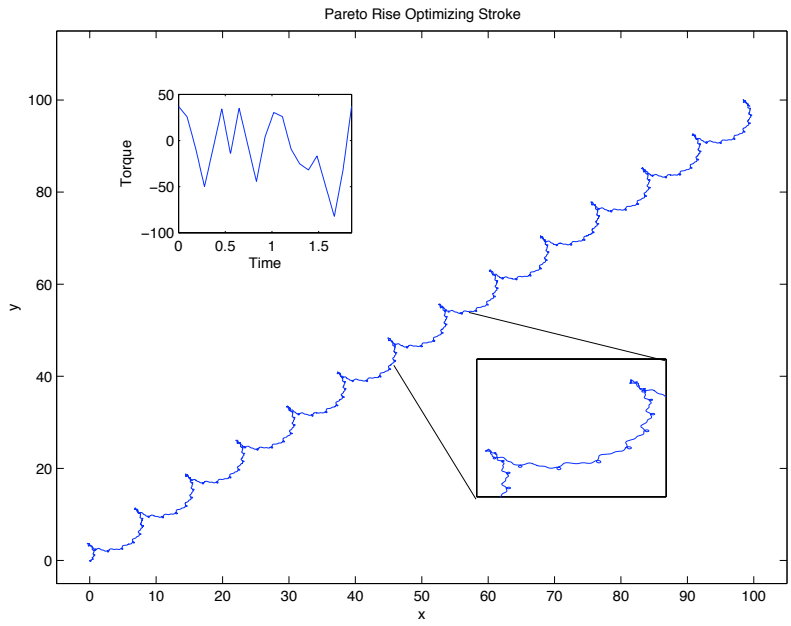

Figure 7.13: Example solution of rise-forward optimization

objective optimization for vertical displacement and a multi-objective, Pareto-style, optimization which optimized two parameters at once. The results from these optimizations outperformed the results from a commercially available SQP optimization.

Future work could involve better understanding the diversity-mainenence problem in the single-objective optimization and the rise/forward multi-objective optimization. Also interesting from a more scientific (as opposed to optimization) view-point, would be to study why this system exhibits clustering behavior in the power/rise optimization (Figure 7.8), as opposed to the more ergodic front of the rise-forward optimization. It should be noted, though, that the latter case could simply be ergodic because of poor diversity maintenance. Additionally, the optimal solutions could be studied as a function of the parameters I^* and γ. As mentioned earlier in the text, a GA which optimizes all three possible fitnesses (rise, power, and forward flight) is also intriguing. Finally,

more work could go into parallelizing the algorithm in order to speed-up the process. For all the work here, each run was done on only a single processor.

Of course, there is much room for future improvements and hypotheses here. In particular, control of the flapper could be studied. One numerical experiment could be: given a random gust of wind, what is the optimal control to right the flapper? Also, comparisons could be made between purely rotational flappers and translational and rotational flappers (more similar to a real insect or flapping animal). Does the rotational flapper flap more efficiently? How does rotation affect control with respect to translation? These are questions that should become feasible to answer with algorithmic and implementation improvements.

BIBLIOGRAPHY

[1] A. Krogh. The progress of physiology. *Amer. J. Physiol.*, 90:243–251, 1929.

[2] T. Weis-Fogh. Energetics of hovering flight in hummingbirds and drosophila. *J. Exp. Bio.*, 56:79–104, 1972.

[3] C. P. Ellington. The aerodynamics of hovering insect flight. *Phil. Tran. R. Soc. Lond. B*, 305:1–181, 1984.

[4] S. P. Sane. The aerodynamics of insect flight. *Journal of Experimental Biology*, 206:4191–4208, 2003.

[5] Z. J. Wang. Dissecting insect flight. *Annu. Rev. Fluid. Mech.*, 37:183–210, 2005.

[6] C. P. Ellington. The novel aerodynamics of insect flight: Applications to micro-air vehicles. *J. Exp. Bio.*, 202:3439–3448, 1999.

[7] R. J. Wood. The first takeoff of a biologically inspired at-scale robotic insect. *IEEE Trans. Robotics*, 24:341–347, 2008.

[8] F. Van Breugel, W. Regen, and H. Lipson. From insects to machines. *IEEE Robotics & Auto. Mag.*, pages 68–74, December, 2008.

[9] R. S. Fearing, K. H. Chiang, M. H. Dickinson, D. L. Pick, M. Sitti, and J. Yan. Wing transmission for a micromechanical flying insect. *Proceedings of the IEEE International Conference on Robotics and Automation*, 2:1509–1516, 2000.

[10] R. E. Kohler. *Lords of the Fly: Drosophila Genetics and the Experimental Life*. U. Chicago Press, Chicago, IL, 1994.

[11] M. D. Adams and et al. The genome sequence of *Drosophila melanogaster*. *Science*, 287:2185–2195, 2000.

[12] C. H. Greenewalt. Dimensional relationships for flying animals. *Smithsonian Misc. Coll.*, 144(2):1–46, 1962.

[13] S. E. Sutton and P. J. Hudson. The vertical distribution of small flying insects in the lowland rain forest of zaire. *Zoo. J. of the Linnean Soc.*, 68:111–123, 1980.

[14] S. A. Combes. Aerial jousting in orchid bees: Biomechanics versus behavior in competitive interactions. *Comp. Bio. and Physiol. A*, 150:S77, 2008.

[15] S. A. Combes and R. Dudley. Turbulence-driven instabilities limit insect flight performance. *Proc. Nat. Acad. Sci.*, 106:9105–9108, 2009.

[16] K. E. Machin and J. W. S. Pringle. The physiology of insect fibrillar muscle. ii. mechanical properties of a beetle flight muscle. *Phil. Tran. R. Soc. Lond. B*, 151:204–225, 1959.

[17] H. Wagner. Flight performance and visual control of flight of the free-flying housefly (*Musca domestica* l.). I. Organization of the flight motor. *Phil. Tran. R. Soc. Lond. B*, 312:527–551, 1986.

[18] A. R. Ennos. Inertial and aerodynamic torques on the wings of diptera in flight. *J. Exp. Bio.*, 142:87–95, 1989.

[19] J. M. Zanker. The wing beat of *Drosophila melanogaster*. I. Kinematics. *Phil. Tran. R. Soc. Lond. B*, 327:1–18, 1990.

[20] M.H. Dickinson, F.-O. Lehmann, and K. G. Götz. The active control of wing rotation by *Drosophila*. *J. Exp. Bio.*, 182:173–189, 1993.

[21] S. P. Sane, A. Dieudonné, M. A. Willis, and T. L. Daniel. Antennal mechanosensors mediate flight control in moths. *Science*, 315:863–866, 2007.

[22] J. H. Marden, M. R. Wolf, and K. E. Weber. Aerial performance of *Drosophila melanogaster* from populations selected for upwind flight ability. *J. Exp. Bio.*, 200:2747–2755, 1997.

[23] L. Ristroph, G. J. Berman, A. J. Bergou, Z.J. Wang, and I. Cohen. Automated hull reconstruction motion tracking (HRMT) applied to sideways maneuvers of free-flying insects. *J. Exp. Bio.*, 212:1324–1335, 2009.

[24] G. K. Taylor and A. L. R. Thomas. Dynamic flight stability in the desert locust *Schistocerca gregaria*. *J. Exp. Bio.*, 206:2803–2829, 2003.

[25] S. N. Fry, R. Sayaman, and M. H. Dickinson. The aerodynamics of hovering flight in *Drosophila*. *J. Exp. Bio.*, 208:2303–2318, 2005.

[26] S. Alben and M. Shelley. Coherent locomotion as an attracting state for a free flapping body. *Proc. Nat. Acad. Sci.*, 102:11163–11166, 2005.

[27] A. J. Bergou, S. Xu., and Z. J. Wang. Passive wing pitch reversal in insect flight. *J. Fluid Mech.*, 591:321–337, 2007.

[28] D. I. Pullin and Z. J. Wang. Unsteady forces on an accelerating plate and application to hovering insect flight. *J. Fluid Mech.*, 509:1–21, 2004.

[29] M. Iima. A two-dimensional aerodynamic model of freely flying insects. *J. Theor. Bio.*, 247:657–671, 2007.

[30] L. Ristroph and J. Zhang. Anomalous hydrodynamic drafting of interacting flapping flags. *Phys. Rev. Lett.*, 101:194502, 2008.

[31] N. Vandenberghe, S. Childress, and J. Zhang. On unidirectional flight of a free flapping wing. *Phys. of Fluids*, 18:014102, 2006.

[32] Z. J. Wang. Vortex shedding and frequency selection in flapping flight. *J. Fluid Mech.*, 410:323–341, 2000.

[33] Z. J. Wang. Effect of forewing and hindwing interactions on aerodynamic forces and power in hovering dragony flight. *Phys. Rev. Lett.*, 99:148101, 2007.

[34] G. K. M. Cheung. *Visual Hull Construction, Alignment and Refinement for Human Kinematic Modeling, Motion Tracking and Rendering*. PhD thesis, Carnegie Mellon University, Pittsburgh, PA, 2003.

[35] K. Pearson. On lines and planes of closest fit to systems of points in space. *Philosophical Magazine*, 2:559–572, 1901.

[36] K. S. Brown and J. P. Sethna. Statistical mechanical approaches to models with many poorly known parameters. *Phys. Rev. E.*, 68:021904, 2003.

[37] R. N. Gutenkunst, J. J. Waterfall, F. P. Casey, Brown K.S., C. K. Myers, and J. P. Sethna. Universally sloppy parameter sensitivities in systems biology models. *PLoS Comp. Bio.*, 3:189, 2007.

[38] J. J. Waterfall, F. P. Casey, R. N. Gutenkunst, K. S. Brown, C. R. Myers, P. W. Brouwer, V. Elser, and J. P. Sethna. Sloppy-model universality and the vandermonde matrix. *Phys. Rev. Lett.*, 97:165501, 2006.

[39] B. C. Daniels, Y.-J. Chen, J. P. Sethna, R. N. Gutenkunst, and C. R. Myers. Sloppiness, robustness, and evolvability in systems biology. *Curr. Op. in Biotech.*, 19:389–395, 2008.

[40] U. Pesavento and Z. J. Wang. Falling paper: Navier-Stokes solutions, model of fluid forces, and center of mass elevation. *Phys. Rev. Lett.*, 93:144501–144504, 2004.

[41] A. Andersen, U. Pesavento, and Z. J. Wang. Unsteady aerodynamics of fluttering and tumbling plates. *J. Fluid Mech.*, 541:65–90, 2005.

[42] A. Andersen, U. Pesavento, and Z. J. Wang. Analysis of transitions between fluttering, tumbling and steady descent of falling cards. *J. Fluid Mech.*, 541:91–104, 2005.

[43] M. H. Dickinson and J. R. B. Lighton. Muscle efficiency and elastic storage in the flight motor of *Drosophila*. *Science*, 268:87–90, 1995.

[44] J. F. Harrison and S. P. Roberts. Flight respiration and energetics. *Ann. Rev. of Physiol.*, 62:179–205, 2000.

[45] A. E. Kammer and B. Heinrich. Insect flight metabolism. *Adv. Insect Physiol.*, 13:133–228, 1978.

[46] R. Dudley. *The Biomechanics of Insect Flight*. Princeton University Press, Princeton, NJ, 2000.

[47] R. McN. Alexander. *Optima for Animals*. Princeton University Press, Princeton, NJ, 1996.

[48] R. McN. Alexander. A minimum energy cost hypothesis for human arm trajectories. *Biol. Cybern.*, 76:97–105, 1997.

[49] R. McN. Alexander. Design by numbers. *Nature*, 412:591, 2001.

[50] M. Srinivasan and A. Ruina. Computer optimization of a minimal biped model discovers walking and running. *Nature*, 439:72–75, 2006.

[51] J. Wilkening and A. E. Hosoi. Shape optimization of a swimming sheet over a thin liquid layer. *J. Fluid Mech.*, 601:25–61, 2008.

[52] G. A. Parker and J. M. Smith. Optimality theory in evolutionary biology. *Nature*, 348:27–33, 1990.

[53] J. E. A. Bertram. Constrained optimization in human walking: cost minimization and gait plasticity. *J. Exp. Bio.*, 208:979–991, 2005.

[54] T. L. Hedrick and T. L. Daniel. Flight control in the hawkmoth manduca sexta: the inverse problem of hovering. *J. Exp. Bio.*, 209:3114–3130, 2006.

[55] M. Roper, R. E. Pepper, M. P. Brenner, and A. Pringle. Explosively launched spores of ascomycete fungi have drag-minimizing shapes. *Proc. Nat. Acad. Sci.*, 52:20583–20588, 2008.

[56] D. Tam and A. E. Hosoi. Optimal stroke patterns for Purcell's three-link swimmer. *Phys. Rev. Lett.*, 98:068105, 2007.

[57] Z. J. Wang. Aerodynamic efficiency of flapping flight: analysis of a two-stroke model. *J. Exp. Bio.*, 211:234–238, 2008.

[58] S. J. Gould and R. C. Lewontin. The spandrels of San Marco and the Panglossian paradigm: A critique of the adaptionist programme. *Phil. Tran. R. Soc. Lond. B*, 205:581–598, 1979.

[59] D. C. Queller. The spaniels of St. Marx and the Panglossian paradox: A critique of a rhetorical programme. *Quart. Rev. Bio.*, 70:485–489, 1995.

[60] F. Jacob. *The Possible and the Actual*. U. Washington Press, Seattle, 1982.

[61] T. Weis-Fogh. Quick estimates of flight fitness in hovering animals. *J. Exp. Bio.*, 59:139–230, 1973.

[62] A. R. Ennos. The kinematics and aerodynamics of the free flight of some diptera. *J. Exp. Bio.*, 142:49–85, 1989.

[63] R. Dudley and C. P. Ellington. Mechanics of forward flight in bumblebees. I. Kinematics and morphology. *J. Exp. Bio.*, 148:19–52, 1990.

[64] A. P. Willmott and C. P. Ellington. The mechanics of flight in the hawkmoth *Manduca sexta*. *J. Exp. Bio.*, 200:2705–2745, 1997.

[65] D. B. Russell. *Numerical and Experimental Investigations into the Aerodynamics of Dragonfly Flight*. PhD thesis, Cornell University, Ithaca, NY, 2004.

[66] S. P. Sane and M. H. Dickinson. The control of flight force by a flapping wing: Lift and drag production. *J. Exp. Bio.*, 204:2607–2626, 2001.

[67] M. H. Dickinson, F.-O. Lehmann, and S. P. Sane. Wing rotation and the aerodynamic basis of insect flight. *Science*, 284:1954–1960, 1999.

[68] J. R. Usherwood and C. P. Ellington. The aerodynamics of revolving wings: I. model hawkmoth wings. *J. Exp. Bio.*, 205:1547–1564, 2002.

[69] R. Dudley and C. P. Ellington. Mechanics of forward flight in bumblebees. II. Quasi-steady lift and power requirements. *J. Exp. Bio.*, 148:53–88, 1990.

[70] M. Sun and G. Du. Lift and power requirements of hovering insect flight. *Acta Mechanica Sinica*, 19:458–469, 2003.

[71] M. Milano and P. Koumoutsakos. A clustering genetic algorithm for cylinder drag optimization. *J. Comp. Phys.*, 175:79–107, 2002.

[72] M. J. D. Powell. A new alogorithm for unconstrained minimization. In J.B. Rosen, O.L. Mangasarian, and K. Ritter, editors, *Nonlinear Programming*, pages 31–66, New York, NY, 1970. Academic Press.

[73] R. A. Norberg. The pterostigma of insect wings an inertial regulator of wing pitch. *J. of Comp. Physiol. A*, 81:9–22, 1972.

[74] G. J. Stephens, B. Johnson-Kerner, W. Bialek, and W. S. Ryu. Dimensionality and dynamics in the behavior of *C. Elegans*. *PLoS Comp. Bio.*, 4:1–10, 2008.

[75] A. J. Bergou and et al. The elastic drag ratchet: How insects control their wings to induce aerial maneuvers. 2009. *In Prep*.

[76] L. Ristroph and et al. Insect autopilot. 2009. *In Prep*.

[77] T. L. Hedrick. Software techniques for two- and three-dimensional kinematic measurements of biological and biomimetic systems. *Bioinsp. Biomim.*, 3:034001, 2008.

[78] Y. Liu and M. Sun. Wing kinematic measurements and aerodynamics of hovering droneflies. *J. Exp. Bio.*, 211:2014–2025, 2008.

[79] D. K. Riskin, D. J. Willis, J. Iriatre-Díaz, T. L. Hedrick, M. Kostandov, J. Chen, D. H. Laidlaw, K. S. Breuer, and S. M. Swartz. Quantifying the complexity of bat wing kinematics. *J. Theor. Bio.*, 254:604–615, 2008.

[80] S. M. Walker, A. L. R. Thomas, and G. K. Taylor. Photogrammetric reconstruction of high-resolution surface topographies and deformable wing kinematics of tethered locusts and free-flying hoverflies. *R. Soc. Lond. Interface*, 6:351–366, 2009.

[81] C. Schilstra and J. H. van Hateren. Blowfly flight and optic flow: I. Thorax kinematics and flight dynamics. *J. Exp. Bio.*, 202:1481–1490, 1999.

[82] E. Fontaine, D. Lentink, S. Kranenbarg, Müller U. K., J. L. van Leeuwen, A. H. Barr, and J. W. Burdick. Automated visual tracking for studying the ontogeny of zebrafish swimming. *J. Exp. Bio.*, 211:1305–1316, 2008.

[83] E. I. Fontaine, F. Zabala, M. H. Dickinson, and J. W. Burdick. Wing and body motion during flight initiation in *Drosophila* revealed by automated visual tracking. *J. Exp. Bio.*, 212:1307–1323, 2009.

[84] A. D. Briscoe and L. Chittka. The evolution of color vision in insects. *Ann. Rev. Entomol.*, 46:471–510, 2001.

[85] B. G. Baumgart. *Geometric Modeling for Computer Vision*. PhD thesis, Stanford University, Palo Alto, CA, 1974.

[86] H. Steinhaus. Sur la division des corp materiels en parties. *Bull. Acad. Polon. Sci.*, 4:801–804, 1956.

[87] S. A. Combes and T. L. Daniel. Into thin air: contributions of aerodynamic and inertial-elastic forces to wing bending in the hawkmoth *Manduca sexta*. *J. Exp. Bio.*, 206:2999–3006, 2003.

[88] A. M. Mountcastle and T. L. Daniel. Aerodynamic and functional consequences of wing compliance. *Exp. in Fluids*, 46:873–882, 2009.

[89] F.-O. Lehmann and M.H. Dickinson. The changes in power requirements and muscle efficiency during elevated force production in the fruit fly *Drosophila melanogaster*. *J. Exp. Bio.*, 200:1133–1143, 1997.

[90] F.-O. Lehmann and M. H. Dickinson. The control of wing kinematics and flight forces in fruit flies (*Drosophila* spp.). *J. Exp. Bio.*, 201:385–401, 1998.

[91] F.-O. Lehmann and M. H. Dickinson. The production of elevated flight force compromises manoeuvrability in the fruit fly *Drosophila melanogaster*. *J. Exp. Bio.*, 204:627–635, 2001.

[92] R. Dudley and P. Chai. Animal flight mechanics in physically variable gas mixtures. *J. Exp. Bio.*, 199:1881–1885, 1996.

[93] R. Dudley. Extraordinary flight performance of orchid bees (*Apidae: Euglossini*) hovering in helox (80% He / 20% O_2. *J. Exp. Bio.*, 198:1065–1070, 1995.

[94] W. B. Dickson, A. D. Straw, and M. H. Dickinson. Integrative model of *Drosophila* flight. *AIAA Journal*, 46:2150–2164, 2008.

[95] Wolfram Research. *Mathematica, Version 7*. Wolfram Research, Inc., Champaign, Illinois, 2008.

[96] S. Revzen and J. Guckenheimer. Estimating the phase of synchronized oscillators. *Phys. Rev. E*, 78:051907, 2008.

[97] C. J. Pennycuick. Power requirements for horizontal flight in the pigeon *Columba livia*. *J. Exp. Bio.*, 49:527–555, 1968.

[98] C. P. Ellington. Limitations on animal flight performance. *J. Exp. Bio.*, 160:71–91, 1991.

[99] G. Card and M. H. Dickinson. Performance trade-offs in the flight initiation of *Drosophila*. *J. Exp. Bio.*, 211:341–353, 2008.

[100] D. N. Burghes and A. M. Downs. *Modern Introduction to Classical Mechanics & Control*. John Wiley & Sons, Inc., London, 1975.

[101] T. Weis-Fogh. An aerodynamic sense organ stimulating and regulating flight in locusts. *Nature*, 164:873–874, 1949.

[102] M. Gewecke and M. Niehaus. Flight and flight control by the antennae in the small tortoiseshell (*Aglais urticae* L. Lepidotera): I. Flight balance experiments. *J. Comp. Physiol.*, pages 249–256, 1981.

[103] S. A. Burdick, M. B. Reiser, and M. H. Dickinson. The role of visual and mechanosensory cues in structuring forward flight in *Drosophila melanogaster*. *J. Exp. Bio.*, 210:4092–4103, 2009.

[104] H. Autrum. Electrophysiological analysis of the visual systems in insects. *Exp. Cell Res.*, Suppl. 5:426–439, 1958.

[105] A. Sherman and Dickinson M. H. A comparison of visual and haltere-mediated equilibrium reflexes in the fruit fly *Drosophila melanogaster*. *J. Exp. Bio.*, 206:295–302, 2003.

[106] G. J. Berman and Z. J. Wang. Energy-minimizing kinematics in hovering insect flight. *J. Fluid Mech.*, 582:153–168, 2007.

[107] M. H. Dickinson and K. Götz. Unsteady aerodynamic performance of model wings at low reynolds numbers. *J. Exp. Bio.*, 174:45–64, 1993.

[108] C.P. Ellington, C. van den Berg, A. P. Willmott, and A. L. R. Thomas. Leading-edge vortices in insect flight. *Nature*, 384:626–630, 1996.

[109] A. P. Engelbrecht. *Fundementals of Computational Swarm Intelligence*. Wiley, Hoboken, NJ, 2005.

[110] S. Bird and X. Li. Adaptively choosing niching parameters in a PSO. In *Proceedings of GECCO 2006*, page 3, 2006.

[111] J. B. MacQueen. Some methods for classifications and analysis of multivariate observations. In *Proceedings of the 5th Berkeley Symposium on Mathematical Statistics and Probability*, pages 281–297, Berkely, CA, 1967. University of California Press.

[112] G. Henkelman and H. Jónsson. Improved tangent estimate in the nudged elastic band method for finding minimum energy paths and saddle points. *J. Chem. Phys.*, 113:9978–9985, 2000.

[113] S. A. Trygubenko and D. J. Wales. A doubly nudged elastic band method for finding transition states. *J. Chem. Phys.*, 120:2082–2094, 2004.

[114] A. J. Bergou. Internal communication. 2007.

[115] M. R. Hestenes and E. Stiefel. Methods of conjugate gradients for solving linear systems. *J. of Res. of the Nat. Bureau of Standards*, 49:409–436, 1952.

[116] L. I. Sedov. *Two Dimensional Problems in Hydrodynamics and Aerodynamics*. Interscience Publishers, New York, NY, 1965.

[117] F. Moon. *Chaotic Vibrations*. Wiley-Interscience, New York, NY, 1987.

[118] H. Peitgen, H. Jurgens, and D. Saupe. *Chaos and Fractals*. Springer, New York, NY, 2004.

[119] E. N. Lorenz. Deterministic nonperiodic flow. *J. Atmos. Sci*, 20:130–141, 1963.

[120] H. Kantz and T. Schreiber. *Nonlinear Time Series Analysis*. Cambridge University Press, Cambridge, UK, 2004.

[121] D. Kalyanmoy, A. Pratap, S. Agarwal, and T. Meyarivan. A fast and elitist multiobjective genetic algorithm: NGSA-II. *IEEE Trans. Evo. Comp.*, 6:182–197, 2002.

[122] P. E. Gill, W. Murray, and M. A. Saunders. An SQP algorithm for large-scale constrained optimization. *SIAM J. Optim.*, 12:979–1006, 2002.